Modelling the Spectra of Exoplanets



Jake Taylor
New College
University of Oxford

A thesis submitted for the degree of
Doctor of Philosophy

Trinity 2021

Dedicated to Mum and Dad. Thank you for letting me spread my wings into the unknown. None of this would have been possible without your love and support. I love you.

Acknowledgements

Coming from a struggling comprehensive state school I never thought I would get to this stage in my life, and, with the odds stacked against me in many ways, I have been able to fulfil one of my lifelong dreams. I want to thank my physics teachers: Mr Warriner, Mr Athens and Mr Sheppard, who managed to cultivate and fuel my interest in physics despite the difficult job of controlling students who made every lesson a battle. I'd like to thank Mr Adjei, who always believed in me and wanted me to strive for success. I never properly thanked you for coming to visit me in the hospital after I had my lung surgery, so I would like to take the opportunity to do so here. It meant a huge amount to me that you decided to take time off during the school day to bring everyone to show support, it kept my spirits up.

Thank you to the Reuben Foundation, especially Lisa Reuben, who awarded me the Reuben's Scholarship to study my undergraduate degree at UCL. Thank you also to Nick Greenwood for funding the Penrose Scholarship.

I want to thank my original supervisors Patrick Irwin and Suzanne Aigrain for giving me a chance to pursue my dreams. You both supported and helped me when I needed it the most.

Thank you to my other supervisor Vivien Parmentier, you arrived at Oxford at the beginning of my second year and took me under your wing. I was lost when my project fell through. You helped pick up the pieces and be my guide in the field of exoplanet atmospheres. I'm extremely grateful to have you in my corner.

To Juan Alday Parejo, the best office mate I could ever imagine! We were both worried that we'd get someone boring as an office mate, but after our trip to the King's Arms on the first day we met we knew then it was going to be an amazing friendship and journey together.

To Ryan Garland, Daniel Toledo Carrasco and Ashwin Braude. Thank you for all the pub trips and gossiping we had. You were all so welcoming to the group. Our antics will serve as great stories to tell in the future.

To Robin De Meyere, Cameron Gardner, Norbert Zicher, Josh Stallings, Dane Clark, Waverly Sisson, Eddie Maza, Helen Potts and Ellie Hick. Oxford would never have been the same without you. Thank you for all the amazing memories we made together.

To Peter McGill, Nick Massey, Tom Sherborne and Garsha Seyf. Your support was invaluable. Despite being in different cities, it felt like you were with me all the time, I love you all.

None of this would have been possible without the love and support from my family. Most of the time they had no clue what I was doing, but they had my back regardless. Thank you and I love you.

Lastly, I want to acknowledge myself. Jake, you wrote this thesis during one of the worst periods of your life... and you did it! It may not be the grand thesis you always dreamt about, but be proud of what you were able to achieve and overcome by completing this. Let this thesis serve as a reminder of your grit and perseverance.

Abstract

Extrasolar planets (exoplanets) are planetary-mass objects that orbit different stars in our galaxy. To date, there have been over 4000 of these objects discovered, with a bias towards objects that transit their host star. This thesis focuses on interpreting the emission spectra of hot to ultra-hot Jupiter exoplanets. These are Jupiter-sized objects which orbit close to their host star, resulting in high effective temperatures and a tidally-locked orbital configuration.

The study of the emission spectra of exoplanets lets us probe the vertical chemical and thermal structure of the planet's atmosphere. The majority of the current observations are of hot to ultra-hot Jupiter planets, as the day-side flux is readily measurable with current telescopes. Therefore the first part of the thesis focuses on upgrading the NEMESIS model to calculate H^- opacities and implementing a temperature-pressure parameterisation that can handle temperature profiles that can span the parameter space that contain non-inverted and inverted profiles.

These objects exhibit large day-night contrasts due to their tidally-locked nature, and it has been shown that this is detectable with current observations. We explore in this thesis the biases that can arise when studying an exoplanet with a non homogeneous thermal structure. We find that if we assume the thermal structure to be uniform on the disc, this can lead to spurious detection of molecules. We show that by retrieving the nightside and the dayside of the planet simultaneous we can perform an unbiased retrieval. We find that if the nightside contribution is small enough, a simple dilution factor can be used to account for the spatial inhomogeneity of the atmosphere.

Finally, we explore how scattering clouds can affect the way we interpret the emission spectra of cloudy exoplanets. We show that using a model that does not contain scattering to study the emission spectra of a cloudy exoplanet can lead to incorrectly inferred chemical abundances and also

an erroneous detection of a thermal inversion. To provide a more agnostic approach to the modelling of clouds, in this thesis we have developed a novel technique to retrieve the cloud scattering properties, namely the single scattering albedo, which approximately encapsulates the real and imaginary refractive index spectra and the particle size of the cloud condensing species.

This thesis has broader impacts on the exoplanet community. The tools developed for hot and large planets will ensure that when moving to study smaller and cooler objects in the future, we can trust that our techniques are well verified.

Contents

1 Introduction **1**

1.1 A Brief History of Exoplanets 1

1.2 Characterising Exoplanets using their Secondary Eclipse 2

1.2.1 Time of Secondary Eclipse 2

1.2.2 Depth and Wavelength Dependence of Secondary Eclipse . . . 3

1.2.3 Summary of Current Limitations 6

1.3 Characterising Exoplanets using their Phase Curves 7

1.3.1 Observations: Photometric and Spectroscopic 7

1.3.2 Limitations of Phase Curve Observations 8

1.4 Future Direction of the Field 9

1.4.1 The James Webb Space Telescope (JWST) 9

1.4.2 Ariel 9

1.5 Roadmap to the thesis 10

2 NEMESIS **12**

2.1 Radiative Transfer 12

2.2 Correlated-k 14

2.3 What is a Spectral Retrieval? 16

2.4 Temperature-Pressure (T-P) Parameterisation 17

2.5 H^- Opacity 18

2.6 2-D and Dilution Parameterisations 20

2.7 Single Scattering Albedo (SSA) Parameterisation 22

2.8 Nested Sampling 23

2.8.1 Why Nested Sampling over MCMC? 25

2.8.2 Bayesian Evidence and Model Selection 26

3 Understanding and Mitigating Biases of Inhomogeneous Emission Spectra with JWST **28**
3.1 Introduction . . . 28
3.2 Analytical Description . . . 29
3.3 Model Setup . . . 31
3.3.1 Composite Spectra . . . 31
3.3.2 Treatment of angles . . . 35
3.3.3 WASP-43b . . . 35
3.3.4 Application to NIRSpec . . . 36
3.4 Retrieval Results . . . 37
3.4.1 NIRSpec G140M . . . 38
3.4.2 NIRSpec G235M . . . 40
3.4.3 NIRSpec G395M . . . 42
3.4.4 NIRSpec Prism . . . 42
3.4.5 G235M + G395M . . . 42
3.4.6 2-D vs Dilution styles . . . 43
3.4.7 Origins of the chemistry bias . . . 45
3.4.8 Wavelength dependent radius effect . . . 47
3.5 Summary . . . 48

4 Thermal Scattering of Cloudy Exoplanets with JWST **50**
4.1 Introduction . . . 50
4.2 How thermal scattering shapes the emission spectrum . . . 51
4.2.1 Single Scattering Albedo and Emissivity . . . 51
4.2.2 Solution in the isothermal case . . . 52
4.2.3 Non-isothermal case . . . 53
4.2.4 Expected degeneracies . . . 56
4.3 Results from constant cloud single-scattering albedo case . . . 57
4.3.1 Isothermal atmosphere . . . 58
4.3.1.1 Observing scenario 1: NIRSpec Prism (0.6 - 5.3 μm) 59
4.3.1.2 Observing scenario 2: MIRI LRS (5.0 - 12.0 μm) . . 60
4.3.1.3 Observing scenario 3: Full Wavelength Range 61
4.3.2 Non-isothermal atmosphere . . . 62
4.3.2.1 Observing scenario 1: NIRSpec Prism . . . 64
4.3.2.2 Observing scenario 2: MIRI LRS . . . 64
4.3.2.3 Observing scenario 3: Full Wavelength Range 66

4.3.3 Inverted Thermal Profile . . . 66
4.3.4 Summary . . . 67
4.4 Non-constant cloud single-scattering albedo . . . 68
4.4.1 Realistic cloud single-scattering albedo and constant opacity . 68
4.4.2 SSA Retrieval . . . 69
4.4.3 Al_2O_3 . . . 69
4.4.4 MnS . . . 70
4.4.5 $MgSiO_3$ . . . 71
4.4.6 Fe . . . 72
4.4.7 Realistic cloud single-scattering albedo spectrum and varying opacity . . . 73
4.4.7.1 Retrieval results . . . 75

5 Conclusions and Future Direction **78**
5.1 Conclusions . . . 78
5.2 Future Directions . . . 83
5.2.1 Multidimensional retrieval models . . . 83
5.2.2 Cloud modelling in a retrieval framework . . . 83
5.2.3 Optimal Estimation vs Nested Sampling? . . . 84
5.2.4 Recommendations for the Early Release Science and Guaranteed Time Observations data. . . . 85

A Benckmarking exercises **88**
A.1 NEMESIS vs CHIMERA . . . 88
A.1.1 Forward Modelling . . . 88
A.1.2 Retrieval Modelling . . . 89

B Spectral Retrievals of hot Jupiter Phase Curves Observed with Ariel **93**

C Water Ice Cloud Variability & Multi-Epoch Transmission Spectra of TRAPPIST-1e **98**
C.1 Aims of the Study . . . 98
C.2 Model Setup . . . 98
C.3 Atmospheric Retrievals . . . 99
C.4 Results . . . 99

D Derivation of the General Radiative Transfer Equation from Rutten (2003) 102

D.1 General case 102

Bibliography 106

List of Figures

1.1 Figure taken from Parmentier et al. (2018) showing the emission spectra of hot Jupiters that had been published by 2018. The yellow line through the data is the best fitting blackbody spectrum. Reproduced with permission from Astronomy & Astrophysics, © ESO. 5

2.1 Left: The bound-free and free-free absorption cross sections of the negative hydrogen ion using equations taken from John (1988). Right: Absorption cross sections for a given pressure and temperature taken from Parmentier et al. (2018). Reproduced with permission from Astronomy & Astrophysics, © ESO. 20

2.2 The retrieved chemical abundances presented in Lewis et al. (2020). The histograms show the marginalised probability distributions for the volume mixing ratios for each molecule used in their respective retrieval code. With NEMESIS in green, ATMO in blue and POSEIDON in purple. Reproduced by permission of the AAS. 20

2.3 Common cloud species found in exoplanet atmospheres and their single-scattering albedos. They are calculated for particle radii of 0.1, 0.5, 1.0, 5.0, 10.0 and 50.0 μm over a wavelength range of 0.1 – 20 μm for MnS, S_8, Fe and $CaTiO_3$ and a wavelength range of 0.2 - 20 μm for $MgSiO_3$, $MgFeSiO_3$ and Al_2O_3. Caution needs to be taken when interpreting the results from MnS as the optical constants used in the infrared were inferred from ZnS and Na_2S rather than laboratory experiments (Kitzmann & Heng, 2018). 24

2.4 Example posterior distribution retrieved on a model atmosphere. . . . 26

3.1 Plot showing two planetary spectra considering that a part x of the atmosphere emits like a blackbody and the other part is not emitting any light. The blue curve has a β value of 1.2 and the red curve has the value of 0.8, the function has been plotted using Eq 3.6. The hotter profile covers a smaller fraction of the surface ($x = 0.2$), the opposite is true for the colder profile ($x = 0.8$). For a given wavelength, there exists more than 1 combination of these parameters which give the same flux output. 32

3.2 Ability to disentangle between a planetary spectrum with a hot region with a temperature of 1400K covering a fraction x_0 of the surface and a planetary spectrum with a colder region of $\beta_0 + \Delta\beta = 0.8$, where $\beta_0 = 1$. Hence the colder region has a temperature of $(\beta_0 + \Delta\beta) \times 1400 =$ 1120K. For the colder planetary case the emitting part of the planet covers a larger fraction in order to have the same flux at λ_0. The SNR are calculated following Eq. 3.9 assuming a wavelength range $\Delta\lambda = 2\mu m$ centered at different λ_0 as shown by the x-axis. The plotted threshold can be extrapolated to different contrasts by noting that the SNR scales inversely with the temperature contrast $\Delta\beta$. Note that shorter wavelengths are more important in being able to detect 2-D effects. Increasing the contrast of the profiles shifts the contour lines to longer wavelengths, however the effect is still marginal. 33

3.3 Spectra for the hot ($\beta_{\rm hot} = 1$, magenta) and cold ($\beta_{\rm cold} = 0.4$, green) profiles, alongside the composite spectrum (red) produced with a weighting of x= 80%. For comparison, we also show (in blue) a spectrum generated using the average of the hot and cold TP profiles ($T^4_{\rm average} = \frac{1}{2}(T^4_{\rm hot} + T^4_{\rm cold})$). Note the small, but visible differences between the composite and average spectra, especially at shorter wavelengths. . . 34

3.4 The weighted-by-abundance absorption coefficients of the molecules used in this study. We have highlighted the wavelength coverage of each of the instruments. The absorption coefficients are calculated at a temperature of 1450K and pressure of 0.1bar. 37

3.5 Best fitting models and accompanying posterior distributions for a planet scenario where the hot profile covers 60% of the observed disc as seen using NIRSpec G140M. We overplot the three retrieval styles: 2-D (magenta), 1-D (blue) and Dilution (red) and show in the residuals (model-data) that they present good fits to the data. The retrieved chemical abundances shown in the corner plot on the left are strongly biased compared to the true values (in black) for the 1-D retrieval case. This leads to a spurious detection of CO while no CO feature is seen in the original model (see the opacity comparison in Fig. 3.4). 40

3.6 Best fitting retrievals and accompanying posterior distributions for a planet scenario of 60% flux applied to the hot profile as seen using NIRSpec G235M. We overplot the three retrieval styles: We overplot the three retrieval styles: 2-D (magenta), 1-D (blue) and Dilution (red) and show in the residuals (model-data) that they present good fits to the data. The true values are given by the solid black lines. When analysing the chemistry result presented in the triangle plot, we find a biasing of the result from the 1-D style, we see that the 1-D retrieval detects H_2O and CH_4 at values which are outside 2-σ from the input. 41

3.7 Best fitting retrievals and accompanying posterior distributions for a planet scenario of 60% flux applied to the hot profile as seen using NIRSpec G395M. We overplot the three retrieval styles: 2-D (magenta), 1-D (blue) and Dilution (red) and show in the residuals (model-data) that they present good fits to the data. The true values are given by the solid black lines. When analysing the chemistry result presented in the triangle plot, we find a biasing of the result from the 1-D style, we see that the 1-D retrieval detects CO at a value which is outside 2-σ from the input. 43

3.8 Best fitting retrievals and accompanying posterior distributions for the planet scenarios with weightings $x = 80\%$ (top) and $x = 20\%$ (bottom), as seen using NIRSpec Prism. We overplot the three retrieval styles: 2-D (magenta), 1-D (blue) and Dilution (red) and show in the residuals (model-data) that they present good fits to the data. The true values are given by the solid black lines. When analysing the chemistry result presented in the triangle plots, we find a biasing of the result. Note that performing a 1-D retrieval presents a good fit to the data, however the chemistry is biased, only by exploring 2-D models and comparing the Bayesian evidence would this have been apparent. Hence caution needs to be taken when performing retrievals on data that is not inherently 1-D. 44

3.9 Best fitting retrievals and accompanying posterior distributions for a planet scenario of 60% flux applied to the hot profile as seen by combining NIRSpec G235M and G395M. We overplot the three retrieval styles: 2-D (magenta), 1-D (blue) and Dilution (red) and show in the residuals (model-data) that they present good fits to the data. The true values are given by the solid black lines. When analysing the chemistry result presented in the triangle plot, we find a biasing of the result from the 1-D style, we see that the 1-D retrieval detects H_2O, CH_4, CO and CO_2 at values which are outside 2-σ from the input. . . 45

3.10 **Left:** Weighted-by-abundance absorption coefficients of the molecules from the best fit 2-D model for the 20% hot flux case shown in Fig. 3.8; we also present the sum of the absorption coefficients, which is representative of the absorption of the final best fitting spectrum. The sum is dominated by the water opacity at most wavelengths. **Right:** Weighted-by-abundance absorption coefficients of the molecules from the best fit 1-D model for the 20% hot flux case shown in Fig. 3.8; we also present the sum of the absorption coefficients, which is representative of the absorption of the final best fitting spectrum. We see that the 1-D retrieval requires an increase in the opacity of all the molecules apart from H_2O to fit to the observations. This is because varying H_2O would shift the total opacity up and down without changing the slope of the opacities at large spectral scales. Other molecules, such as CH_4 or CO have a larger variation between 1 and 5 microns and are used by the retrieval to increase the mean slope of the total atmospheric opacities. 47

3.11 Top: Dilution and 1-D forward models generated from the best fitting parameters from the x = 80% case for the G395M observing mode. For the 1-D, $x = 1.0$ and $\beta = 0.94$ were retrieved and used for the forward model, for the dilution, which is analogous for 2-D, $x = 0.82$ and $\beta = 0.94$ were retrieved and used in the forward model. We chose to compare these due to their chemistry being unbiased in both scenarios, hence we are seeing the effect due to the thermal profiles. Bottom: The ratio of the two models. It can be seen that there is a larger gradient between the two at shorter wavelengths and this begins to plateau at longer wavelengths, this is similar to our analytical model in Fig 3.1. 49

4.1 Model atmospheres varying from cloud free (SSA = 0, smooth red line) to completely dominated by the opacity of the cloud (SSA = 0.9, smooth purple line). The thinner lines containing features, which are due to H_2O in the atmosphere, correspond to isothermal atmospheres with a temperature of 1400 K and a cloud with a SSA of 0.9, whose opacity increases by an order of magnitude between each line, from red to purple. We transition from a molecule opacity dominated regime to a cloud opacity dominated regime. It can be seen that the opacity of the cloud results in different temperature layers being probed. 54

4.2 Impact of the SSA on the emission spectra for different TP profiles. The TP profiles corresponding to cases 1, 2 and 3 (top left, top right and bottom left plot, respectively) are shown in the bottom right plot. All models were generated using $\log(\kappa_{\rm cld}) = 3$ and with roughly solar H_2O and CO abundances. The non-isothermal TP profiles were generated using the 3-parameter model given by Equation 4.8, with $\alpha = 0.1$ and -0.1 for cases 1 and 3, respectively. 55

4.3 **Left**: Best-fitting spectra, temperature profiles and retrieved chemistry for three different retrieval models applied to synthetic NIRSpec Prism observations generated from planet with an isothermal TP profile and cloud opacity of 10^4. For each model we retrieve the TP structure with the analytical TP profile described in Chapter 2. In purple we retrieve on the synthetic data with the constant SSA cloud model. In red we fit using the pure absorbing cloud model. In blue we present the fit using a cloud-free model. We present the retrieved temperature-profiles with the true profile represented by a dashed green line. We present the residuals of the fit with grey shading indicating the error in ppm on the measurement. **Right**: we show the retrieved chemistry for each case with the true value in black. 60

4.4 Same simulations as Figure 4.3, but for the MIRI LRS case. 61

4.5 Same simulations as Figure 4.3, but for the combined NIRSpec Prism and MIRI LRS case. We present the full posterior distribution for the scattering cloud retrieval in Fig. 4.6. 62

4.6 We present the corner plot showing the distribution of parameter space explored for the scattering retrieval presented in Fig. 4.5. For the 1-D histograms, we present the median result and the 1-σ values. This are represented by vertical dashed lines. 63

4.7 **Left:** Best-fitting spectra, temperature profiles and retrieved chemistry for three different retrieval models applied to synthetic NIRSpec Prism observations generated from a planet with three-parameter TP profile and cloud opacity of 10^3. In purple we retrieve on the synthetic data with the 3-parameter TP profile described by Equation 4.8 and model which allows for the single-scattering albedo to be fit as a constant value at all wavelengths. In red we retrieve using a similar model to the one shown in purple. However, we fix the single-scattering albedo to be zero, effectively removing the scattering component of the cloud and making the cloud grey. In blue we present a model that has no cloud. We present the retrieved temperature-profiles with the true profile represented by a dashed green line. We present the residuals of the fit with grey shading indicating the error in ppm on the measurement. **Right:** The posterior distributions of the retrieved chemistry with the colours corresponding to the models in the left plot. The black line represents the true value. 65
4.8 Same as Fig 4.7 but for the wavelength grid and errorbars of MIRI LRS. 65
4.9 Same as Fig 4.7 but for the wavelength grid and errorbars of NIRSpec Prism and MIRI LRS. 66
4.10 Same as Fig 4.7 but for the data generated using an inverted thermal profile. 67
4.11 **Left:** The best-fitted spectra for the three models used on the data generated using a cloud made of Al_2O_3. For the cloud model we consider the particle radius to be of 10 μm and to have a variance of 0.1 following a Gamma distribution as shown in Hansen & Travis (1974). In purple we present the new three-parameter cloud, in red we present a cloud with single-scattering albedo of 0 (i.e., a grey cloud) and in blue we present the cloud-free model. Below we present the residuals of each fit. We present the accompanying temperature retrieval for each of the spectra, which have 1-σ and 2-σ shaded regions. The green dashed line is the input temperature-pressure profile. **Right:** We present the chemistry posterior for each case with the true value present in black. 70
4.12 The same simulations as Figure 4.11, but now for the case of an MnS cloud. 71
4.13 The same simulations as Figure 4.11, but for the $MgSiO_3$ cloud case. 72
4.14 The same simulations as Figure 4.11, but for the Fe cloud case. . . . 73

4.15 The best-fitting retrieved single-scattering albedo (SSA) spectrum using the three-parameter cloud parameterisation. In purple we present the retrieved SSA spectra with 1- and 2-sigma envelopes. In green we present the SSA spectrum for each of the cloud condensing species, which are labelled in each of the plots; each species has been modelled with a particle size of 10 μm. 74
4.16 We present the retrieved single-scattering albedo for the 3-parameter model from Fig. 4.17. The purple lines shows 1000 models drawn from the posterior distribution. We over plot the forward model single-scattering albedo generated using CHIMERA for different pressure levels. We note that the photosphere is between 10^{-2} and 10^{-3} bar, our retrieved single-scattering albedo spectrum is between the forward model single-scattering albedo spectra at these values. 76
4.17 The retrieved results from the data generated using CHIMERA, the error bars and noise were generated using PandExo. Left: The best fitting spectra and retrieved temperature profiles. In purple we present the 3-parameter cloud model. In red we present the purely absorbing cloud model. In blue we present the cloud free model. In green we present the input temperature profile. Right: The retrieved chemical abundances, with the true value represented by a black line. 77

A.1 Forward model comparisons between NEMESIS and CHIMERA. In purple we present the NEMESIS model and in green we present the CHIMERA model. The residuals are shown in the bottom panel. . . . 89
A.2 The best fitting NEMESIS model to the data generated using CHIMERA. The bottom panel shows the residuals of the fit, with grey vertical lines showing the 60ppm error envelope. The right panel shows the retrieved thermal structure in purple and the input thermal structure using to generate the data in green. 91
A.3 The posterior distribution of the NEMESIS simulation that is shown in Figure A.2, the vertical black lines represent the true values that were used to generate the data. 92

B.1 Retrieved temperature structures for the cloud free WASP-43b numerical experiment. We present the median, 1-sigma and 2-sigma intervals in decreasing opacity of purple, and the temperature structure from THOR is presented in black. 94

B.2 Retrieved abundances (VMR) and associated uncertainty for the cloud-free WASP-43b simulations. They are shown by the vertical lines for each molecule. The horizontal solid and dashed lines are the disequilibrium and equilibrium abundances respectively, the values are taken to be around ∼0.1 to 0.01 bar, the region in which our simulations are sensitive to. Phase 0° and phase 180° correspond to the transit and the eclipse respectively. Synthetic observations use disequilibrium chemistry. 95
B.3 Retrieved abundances (VMR) and associated uncertainty for the cloudy WASP-43b simulations. They are shown by the vertical lines for each molecule. The horizontal solid and dashed lines are the disequilibrium and equilibrium abundances respectively, the values are taken to be around ∼0.1 to 0.01 bar, the region in which our simulations are sensitive to. Phase 0° and phase 180° correspond to the transit and the eclipse respectively. Synthetic observations use disequilibrium chemistry. 96
B.4 Retrieved temperature structures for the cloudy WASP-43b numerical experiment. We present the median, 1-sigma and 2-sigma intervals in decreasing opacity of purple, and the temperature structure from THOR is presented in black. 97

C.1 Sample retrieved spectra. Each line represents a different pCO_2 case for a single multi-epoch case. 1- and 2- σ contours are included. . . . 100

C.2 The retrieved posterior distributions for 4 of the key parameters explored in this study. From top to bottom the 4 panels are: CO_2 abundance, H_2O abundance, cloud top pressure and temperature. Each coloured histogram represents the retrieved parameter for 1 of the combined spectra (representing 10 different "observed" epochs), for a total 10 different combined spectra, each with different underlying cloud assumption. The thick solid vertical lines show the terminator-average abundance of CO_2 and H_2O from the input models, while the dotted vertical lines represent the best fit value and the 1-σ constraints on it. With the exception of the 1 bar pCO_2 case, the true CO_2 value is within 1-σ of the retrieved values. We present the 0.1 bar temperature as a solid vertical line in the temperature histograms. It is not possible to present a "true" value for the cloud top pressure as this is different for each scenario. The consistency of the retrieved cloud top pressures demonstrates that the precision of the data is not high enough to detect this variability. 101

Chapter 1

Introduction

1.1 A Brief History of Exoplanets

Extrasolar planets, otherwise known as exoplanets, have been postulated to exist even before the invention of telescopes in 1608 and before the discovery of the outer solar system planets Uranus (Herschel & Watson, 1781) and Neptune (Galle, 1846). The most notable account was that of Italian Dominican friar and Hermetic occultist, Giordano Bruno. In Bruno's work De L'Infinito, Universo, E Mondi[1] he writes: *"There are countless suns and countless earths all rotating in exactly the same way as the seven planets of our system. We see only the suns because they are the largest bodies and are luminous, but their planets remain invisible to us because they are smaller and non-luminous. The countless worlds in the universe are no worse or no less inhabited than our Earth."*

Bruno was sadly tried for heresy and burned at the stake for denying several core Catholic doctrines; if he had lived today he would probably only face a slew of insults on Twitter. The idea of the existence of planets orbiting around different stars thankfully did not die with Bruno; if we fast forward to 1855 the first peer-reviewed article claiming a potential planetary companion orbiting the star 70 Ophiuchi was published by William Stephen Jacob (Jacob, 1855). This claim was later refuted by Moulton (1899) who calculated that a three-body system with the claimed orbital parameters would be highly unstable. The search for planets around this system is still on going, with a recent study from Wittenmyer et al. (2006) putting constrains on planetary mass objects around the star.

From the mid-to-late 20th century, there had been a shift away from using astrometry due to the lack of concrete results this technique could provide. It must be

[1]Which translates as "On the Infinite Universe & Worlds."

noted that since the launch of GAIA, astrometry has been a very successful technique for measuring stellar and planetary properties. In 1952 Otto Struve proposed that by studying the wobble of a star due to a planetary mass companion (the radial velocity) we could detect planets that are of Jupiter mass and radius (Struve, 1952). It took until 1995 before one was discovered around a main sequence star using this technique (Mayor & Queloz, 1995), and to date, there have been 4,331 exoplanets discovered[2].

1.2 Characterising Exoplanets using their Secondary Eclipse

By observing a planet going behind its star, it is possible to isolate the light coming from the planet itself. We can do this by taking the difference between the light before the planet goes behind the star, which will be a combination of starlight and planet light, and the light when the planet goes behind the star, which would be light from the star itself. This is known as a secondary eclipse measurement.

There are three main physical quantities we can extract when observing the secondary eclipse of an exoplanet: the time it occurs (hence duration), its depth and its wavelength dependence. These extracted quantities are important in achieving the goals of this thesis.

1.2.1 Time of Secondary Eclipse

In order to observe the secondary eclipse, we need to know the time in which it occurs. This can be determined through radial velocity surveys which can determine the eccentricity of the orbit and the argument of periastron, this is most important for longer orbital period objects as it can be assumed that tidally-locked hot Jupiters have circularised their orbits (Guillot et al., 1996). We can assume hot Jupiters have circularised their orbits through tidal dissipation (Ford et al., 2003). Observing the secondary eclipse without knowing the eccentricity or argument of periastron would let us put a constraint on these values, where we can learn about the atmospheric radiative timescales (Cubillos et al., 2013) and tidal effects (Showman & Guillot, 2002; Wilkins et al., 2017; McCormac et al., 2020).

[2] As of 11th January 2021 from `https://exoplanetarchive.ipac.caltech.edu` covering a range sizes and detection techniques.

1.2.2 Depth and Wavelength Dependence of Secondary Eclipse

The secondary eclipse provides the planet-to-star flux ratio, F_p/F_*, which is a combination of reflected light and thermal emission. It is possible to separate these components by observing the secondary eclipse at different wavelengths. Reflected light is usually observed in the optical wavelengths, whereas thermal emission is usually observed in the infrared. It must be noted that for ultra hot Jupiters, the reflected light and thermal emission can have comparable flux contributions at overlapping wavelengths. Studying the wavelength dependence of the secondary eclipse is known as emission spectroscopy. Emission spectroscopy is a popular technique for studying the atmospheres of exoplanets as it contains information about the object's vertical thermal structure, chemical abundances, cloud structure and dynamics (Komacek et al., 2017). We are able to extract this information using emission spectroscopy from spectral features that are seen in either in absorption or emission. We see absorption features when there is a temperature profile that decreases with height and gaseous absorption features reduce the brightness of out-going radiation. The opposite is true with a temperature profile that increases with height, where spectral regions of high gaseous absorption are seen to be brighter than adjacent wavelengths.

The first light detected from an exoplanet happened in 2005 using the now decommissioned Spitzer Space Telescope by both Deming et al. (2005) and Charbonneau et al. (2005). Deming et al. (2005) detected the light coming from the planet HD 209458b as the planet passed behind its star, they were able to determine the flux came from the planet as the observed flux from the system decreased at the epoch the planet passed behind the star, this measurement used the 24μm channel of the Multiband Imaging Photometer for Spitzer (MIRPS). The same technique was used by Charbonneau et al. (2005) using the 4.5μm and 8.0μm bandpasses of the Infrared Array Camera (IRAC).

Since these first detections, the Spitzer Space Telescope revolutionised the study of exoplanet emission spectra. Due to the large number of observations that have been obtained with IRAC, it has been possible to look for trends in atmospheres of hot Jupiters. A study by Schwartz & Cowan (2015) analysed 50 eclipse measurements, some of which had optical observations, and were able to determine energy budget of the objects. Another study investigated 78 hot Jupiters observed with Spitzer to investigate the thermal structure of these objects; they find statistical evidence for a transition between hot Jupiters and ultra-hot Jupiters at 1660K, where the thermal structure changes from non-inverted to inverted (Baxter et al., 2020; Garhart et al., 2020).

By knowing the timing of the secondary eclipse to a high precision, it is possible to begin to map the surface of the dayside of the planet. This is because the ingress and egress of the secondary eclipse is a function of the spatial distribution of the flux on the surface (Cowan & Agol, 2008). This technique, called Eclipse Mapping, has been explored in a theoretical framework to investigate the spatial information of the dayside of hot Jupiters, however current observations are not precise enough to determine this information (Rauscher et al., 2007; Majeau et al., 2012; Dang et al., 2018; Rauscher et al., 2018). The technique of eclipse mapping has recently been shown to be effective in determining the 3D nature of exoplanets using predicted observations from JWST (Mansfield et al., 2020).

Another instrument that has been pioneering for the studying the emission spectra of exoplanets is the Hubble Space Telescope's Wide Field Camera 3 (WFC3). Figure 1.1 shows the emission spectra of hot Jupiters as of 2018. They have been divided up by different lines to indicate various transition regions. Since 2018, there have only been three more emission spectra published using WFC3: WASP-76b (Edwards et al., 2020a), KELT-7b (Pluriel et al., 2020a) and KELT-9b (Changeat & Edwards, 2021).

The observations from WFC3 have enabled us to determine the atmospheric composition of hot Jupiters: this is due to the observations spanning the range where water is the main opacity source. For example, Kreidberg et al. (2014) studied the emission spectra of WASP-43b to detect and determine the amount of water in the planet's atmosphere. Line et al. (2014) performed a more comprehensive self-consistent study to determine the composition of 9 hot exoplanets and find that these planets tend to have a solar C/O ratio and a thermal structure that decreases with height, with the exception of HD 209458b, which appears to have a thermal inversion. The finding of HD 209458b having a thermal inversion was first put forward by Knutson et al. (2008), they determined this using observations from Spitzer IRAC. The IRAC data was reanalysed by Diamond-Lowe et al. (2014) which found no evidence for a thermal inversion. With this new data reduction, Line et al. (2016) performed an analysis combining the WFC3 and Spitzer observations to confirm that there is no thermal inversion. High resolution observations of HD 209485b also determined the absense of a thermal inversion (Schwarz et al., 2015; Giacobbe et al., 2021).

In recent years, the study of ultra-hot Jupiters have become a topic of interest as their hot day-side temperatures results in high quality observations obtained using WFC3. Their muted features posed puzzling questions about their atmospheric composition, which led to the postulation and confirmation of water dissociation and

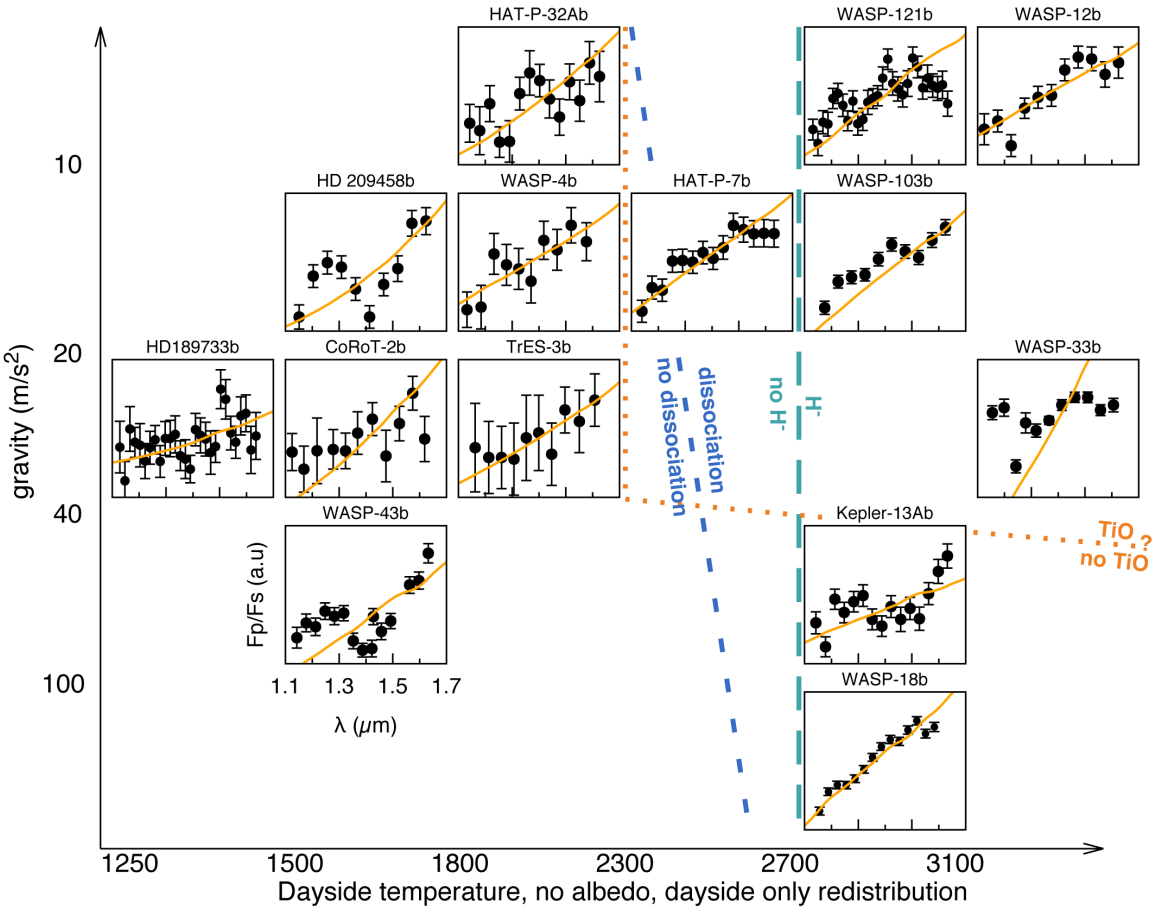


Figure 1.1: Figure taken from Parmentier et al. (2018) showing the emission spectra of hot Jupiters that had been published by 2018. The yellow line through the data is the best fitting blackbody spectrum. Reproduced with permission from Astronomy & Astrophysics, © ESO.

strong opacity from H^- (Evans et al., 2017; Arcangeli et al., 2018; Parmentier et al., 2018; Bell & Cowan, 2018; Mansfield et al., 2020).

The thermal structure of these objects still appear to be elusive. For similar temperature planets their vertical structures vary a lot. For example, WASP-18b exhibits a spectrum which resembles a blackbody (Arcangeli et al., 2018) whereas WASP-121b spectrum has emission features which suggests a thermal inversion (Evans et al., 2017) and Kepler-13Ab, which has a mass between WASP-121b and WASP-18b, shows absorption features indicative of a non-inverted spectra (Beatty et al., 2017). These studies motivated the implementation of the flexible temperature-pressure parameterisation and H^- opacity into NEMESIS which is described in Chapter 2.

1.2.3 Summary of Current Limitations

Studying the emission spectra of exoplanets is challenging as the planet needs to be hot enough that its signal can be differentiated from the host star. The first major limitation of the current secondary eclipse measurements is that the observations were made using infrared telescopes that were not built for these types of observations. Therefore, a huge effort has been made to understand and mitigate the systematics in the observations (Deming et al., 2013; Wakeford et al., 2016; May & Stevenson, 2020; Wakeford et al., 2020). It is extremely important that the process of translating the observations into a usable data product is understood, so that artificial signals are not imposed onto the spectrum which could affect the interpretation of the atmosphere.

Another limitation which was first highlighted by Feng et al. (2016) is that the inhomogeneous nature of planetary atmospheres causes important and detectable effects in the observed spectra. Hence, the one-dimensional technique which has been commonly used will breakdown for high signal-to-noise observations. This has been explored for emission spectra in multiple recent studies including Irwin et al. (2020) who explore a 2.5D approach to modelling the emission spectra and Feng et al. (2020) who take a 2D approach to modelling the atmosphere. The study of Feng et al. (2016) motivated the study conducted in Chapter 3 of this thesis, the contents of which have been published in Taylor et al. (2020), with the techniques used explained in Chapter 2.

Clouds have also been neglected in the analysis of dayside emission spectra; although clouds could form on the dayside of hot Jupiters (Powell et al., 2018), observations indicate that the cloud coverage does not fully cover the dayside (Parmentier et al., 2016; Line et al., 2016). Given that the current population of emission spectra observations are confined to hot objects, the cloud modelling in a retrieval framework

is in its infancy. However, it is important that the community look into this as future observations will be able to study the dayside of cooler objects for which clouds will form on the dayside. The notion that clouds will be studied on the dayside of cooler planets and the nightside of hotter planets led to the study which is presented in Chapter 4 and is published in Taylor et al. (2021), where we explore the impact that scattering clouds have on the emission spectrum.

1.3 Characterising Exoplanets using their Phase Curves

Observing an exoplanet over its full orbit allows us to produce a phase curve, where we can study how the vertical temperature structure of the planet varies with longitude and the observed brightness varies with phase angle. The shape of the phase curve is determined by the variation in the longitudinal structure of the planet. There are two ways to observe a phase curve: photometrically and spectroscopically. Photometric phase curves are ones that observe the planet using a single bandpass, they can be used to track the thermal emission of the planet as it orbits its star, where the longitudinal variation in flux can be used to map the thermal structure of the planet. Spectroscopic phase curves are ones that observe the planets orbit around its star at multiple wavelengths: these can be used to map the chemical abundances and cloud structure as a function on longitude.

Planets with short orbital periods are the ideal candidates to study their atmospheres using phase curves because the short period allows for easy monitoring and they tend to be tidally locked (Guillot et al., 1996). Their tidally-locked nature means that their orbital period is the same as their rotational period, hence the hemisphere facing Earth can be translated to the phase of the orbit. Therefore, longitudinal brightness maps can be created from the observations (Cowan & Agol, 2008).

1.3.1 Observations: Photometric and Spectroscopic

As discussed above, photometric observations in thermal emission can be used to characterise the planet's thermal structure as a function of longitude, this has been achieved using the Spitzer Space Telescope for an array of targets (Knutson et al., 2012; Zellem et al., 2014; Bell et al., 2020; May & Stevenson, 2020). Furthermore, the study of phase curves obtain by Spitzer has provided evidence for nightside clouds on hot Jupiters (Keating et al., 2019; Beatty et al., 2019). Photometric phase curves have been observed in optical bandpasses using Kepler or TESS to probe reflected light

and can therefore provide information about the albedo of the planet as a function of longitude, which can be linked to the cloud coverage. Esteves et al. (2015) utilised the phase curves of 14 planets observed with Kepler to derive planetary properties which include their albedo, day-to-night temperatures and planetary masses. More recently, optical phase curves of planets have been observed with TESS, including WASP-121b (Bourrier et al., 2020; Daylan et al., 2021) and WASP-33b (von Essen et al., 2020).

Spectroscopic phase curves have been obtained using WFC3, but there currently exists only 3 data sets. The lack of data is due to the demand in telescope time needed to obtain the phase curve observations. The first spectroscopic phase curve obtained was by Stevenson et al. (2014) who observed 3 full phase curves of WASP-43b and was able to determine a map of the planet's thermal structure. The second spectroscopic phase curve was of WASP-103b and published by Kreidberg et al. (2018) who detected a lack of water in the planetary atmosphere and attributed this to the presence of H^- opacity. The most recent spectral phase curve to be published is that of WASP-18b (Arcangeli et al., 2019), the results of which are similar to WASP-103b and provide a more consistent understanding of the nature of these ultra-hot Jupiters.

1.3.2 Limitations of Phase Curve Observations

One major issue is how to deal with the systematics of such long observing time. Knutson et al. (2012) reanalysed their 8 μm IRAC phase curve of HD 189733b (Knutson et al., 2007) and found that nearly half of the observation had been contaminated by systematics. Other issues include instrumental drift (Crossfield et al., 2012) and ellipsoidal variations (Cowan et al., 2012).

Interpreting the spectral phase curves requires atmospheric retrieval models which are multidimensional. However, as discussed in Chapter 1.2.3 the majority of models tend to consider the planet as a 1D object. Recent efforts by Irwin et al. (2020) and Feng et al. (2020) analysed the spectral phase curve of WASP-43b to retrieve atmospheric properties in a more self-consistent way, with Irwin et al. (2020) being able to produce a thermal map of the planet and Feng et al. (2020) being able to retrieve the chemical abundances more accurately at each phase angle. Other than WASP-43b, the other two spectral phase curves have currently only been studied in a 1D context.

1.4 Future Direction of the Field

We are slowly moving into an era where we will obtained observations of exoplanets from space-based instruments that were built for the purpose. This will result in an increase in continuous wavelength coverage and signal-to-noise of the observations. Two telescopes which will perform these observations will be the James Webb Space Telescope (Greene et al., 2016) and Ariel (Tinetti et al., 2018).

1.4.1 The James Webb Space Telescope (JWST)

Scheduled to launch in November 2021, JWST is set to revolutionise the way we study the atmospheres of exoplanets. The transiting exoplanet community will be able to utilise all 4 of the instruments of JWST spanning from 0.6 to 12 microns (Bean et al., 2018), providing spectral observations of these alien worlds in never before seen spectral windows. Ranging from Earth-sized planets to Jupiter-sized planets, JWST is equipped to be able to study all types of planets. Of interest to this thesis, it will be able to probe the emission spectra of cooler planets (Piette & Madhusudhan, 2020) and the nightside of hotter planets (Parmentier et al., 2021), something that currently is not possible with HST. Being able to study the emission spectra of these objects will let us explore their cloud structure in more detail, for which we can use the clouds scattering information to characterise their composition. Extracting scattering information from clouds using emission spectra is explored in Chapter 4.

The high quality observations means we will be able to extract more information from a single spectrum than ever before. These spectra can contain spatial information which needs to be correctly modeled to ensure the atmospheric analysis is not impacted by this additional complexity. The impact of inhomogeneities in these expected high quality JWST observations has been a popular topic over the recent years and is discussed further in Chapter 3. Other work has focused on the impact this has on the transmission spectra, which also is impacted by spatial information (Pluriel et al., 2020b)

1.4.2 Ariel

Scheduled to launch in 2029, Ariel will observe the atmosphere of around 1000 exoplanets. This will include secondary eclipses and phase curves. It will perform continuous observations in wavelength from 0.5 - 7.8 μm using 3 photometric channels in the visible and 3 spectroscopic channels in the infrared. The mission will take a three-tier approach to understanding the atmospheres of exoplanets. Tier 1 will be

observations of the complete target list (Edwards et al., 2019) observed at the lowest resolution, this will help to refine planetary parameters such as transit times and produce colour-colour diagrams. Colour-colour diagrams are useful for studying the population of targets to determine their bulk properties and C/O ratios (Dransfield & Triaud, 2020). Tier 2 will perform follow-up spectroscopic observations of around half of the Tier 1 planets to look for atmospheric trends in their atmospheres. Finally, Tier 3 will look at an even smaller subset of planets (around 50 - 100) which will get detailed characterisation to understand their atmospheric chemistry and dynamics.

Around 10% of the mission will be dedicated to the study of exoplanetary phase curves. A recent study by Charnay et al. (2021) highlights the science goals and targets which are best suited for phase curve analysis. They find that for hot Jupiters it is possible to constrain the water abundance at every phase angle for cloudy and cloud-free atmospheres, and for cloud-free atmospheres it is possible to constrain the thermal structure[3].

1.5 Roadmap to the thesis

This thesis will focus on the emission spectra of exoplanets, which have been described in detail in this introduction. In Chapter 2 we describe the upgrades which have been made to the NEMESIS code that allow us to study: the emission spectra of ultra-hot Jupiters; the multidimensional temperature structure that tidally-locked hot Jupiters exhibit; and an agnostic approach to studying the scattering properties of clouds in exoplanet atmospheres. In Chapter 3 we apply the multidimensional technique described in Chapter 2 to understand where biases come from in a retrieval framework, and how to mitigate these when analysing future space-based observations. In Chapter 4 we apply the agnostic cloud parameterisation described in Chapter 2 and demonstrate the impact that scattering has on emission spectra and how we can extract information about the scattering properties of the cloud without causing a bias in the results. Finally, in Chapter 5, we summarise our conclusions and forecast what the future direction of this research might be.

This thesis focuses on developing the optimal techniques to study the emission spectra of hot to ultra hot Jupiters. It is important that we understand these techniques and are able to use them to extract correct information from observations of these objects. These techniques will lay the foundation for future analysis of smaller

[3]I performed the spectral analysis using NEMESIS which lead to these results and the description can be found in Appendix B

and cooler planets, especially planets for which biosignatures could be detected. It is imperative that our techniques are robust so that we can rest assured our interpretation of the data is correct.

Chapter 2

NEMESIS

The **N**on-linear optimal **E**stimator for **M**ultivariat**E** spectral analy**SIS** code (NEMESIS) is a radiative transfer and retrieval framework which was developed at the University of Oxford by Irwin et al. (2008) to study the planetary atmospheres of bodies in the Solar System and has since been adapted to study bodies outside of it. It has the capacity to do so via spectroscopy or via imaging, hence can be applied to data from any instrument and any planetary body. The traditional version of the framework uses a non-linear optimal estimator to find the minimum between the observed and modelled spectra. The optimal estimation framework requires the modelled atmospheric state vector lie close to the *a priori* but given that this thesis focuses on the atmospheres of exoplanets for which the *a priori* is relatively unknown, we used the recently upgraded Bayesian version of the code developed in the thesis of Garland (2018).

The versatility of NEMESIS is shown by the amount of people using the tool to study different objects. Including, but not limited to the Solar System planets (e.g., Giles et al., 2015; Fletcher et al., 2016; Irwin et al., 2015, 2018; Toledo et al., 2019), moons (e.g., Teanby et al., 2018; Bauduin et al., 2018), transmission of exoplanets (e.g., Lee et al., 2014; Krissansen-Totton et al., 2018; Barstow, 2020), emission of exoplanets (e.g., Lee et al., 2012; Barstow et al., 2014) and most recently the direct imaging of brown dwarfs (Garland, 2018), and exoplanet phase curves (Irwin et al., 2020; Taylor et al., 2020).

2.1 Radiative Transfer

To study the atmospheres of exoplanets we need to understand the equations that describe how radiation transfers through matter. This equation is called the radiative

transfer equation and it takes the form:

$$\mu \frac{dI_\lambda}{d\tau_\lambda} = -I_\lambda + S_\lambda \tag{2.1}$$

Where I_λ is the intensity of the beam of light, S_λ is the source function, τ_λ is the optical depth and $\mu = \cos\theta$ is the upward inclination. The optical depth can be thought of as how deep into an atmosphere we can see, where $\tau_\lambda = 1$ represents an approximate limit of what can be seen, hence we reach an opaque layer, and $\tau_\lambda = 0$ represents a clear atmosphere, all light is transmitted. The optical depth has the form:

$$\tau_\lambda = \int_z^{z_\infty} \sigma_\lambda n(z) dz = \int_z^{z_\infty} \kappa_\lambda \rho dz \tag{2.2}$$

where σ is the cross section of the material, $n(z)$ is the material's number density and dz represents the slab of material that the light passes through. The optical depth can also be written as a function of absorption coefficient (κ_λ) and mass density (ρ). To calculate the intensity of the light travelling through the atmosphere we need to solve Eq 2.1 and we can do this integrating the right-hand side of the equation as follows:

$$I_\lambda(\tau_\lambda) = I_{\lambda,\text{deep}} e^{-\tau_{\lambda,\text{deep}}/\mu} + \frac{1}{\mu} \int_0^{\tau_{\lambda,\text{deep}}} S_\lambda(\tau'_\lambda) e^{-\tau'_\lambda/\mu} d\tau'_\lambda(z). \tag{2.3}$$

Here, $\tau_{\lambda,\text{deep}}$ is the optical depth at the bottom of the atmosphere and $I_{\lambda,\text{deep}}$ is the upward intensity from this point in the atmosphere. For a terrestrial planet, this level would be the surface. Therefore, the first term on the right-hand side is the intensity of the beam from the bottom of the atmosphere and the second term is the emission from each layer in the atmosphere. The equation seems relatively simplistic given its current form, however a lot of the intricacies are contained within the source function S_λ. If we assume the source function to consider isotropic scattering it takes the form:

$$S_\lambda(\tau'_\lambda) = \frac{\omega_0 J_\lambda(\tau'_\lambda)}{4\pi} + (1 - \omega_0) B_\lambda(\tau'_\lambda) \tag{2.4}$$

where ω_0 is the single scattering albedo, $J_\lambda(\tau'_\lambda)$ is the mean intensity and $B_\lambda(\tau'_\lambda)$ is the blackbody function. If we consider the simplistic case of no scattering ($\omega_0 = 0$) and no Rayleigh scattering, then the source function is equal to the blackbody function. Hence, the radiative transfer equation can be rewritten as:

$$I_\lambda(\tau_\lambda) = I_{\lambda,\text{deep}} e^{-\tau_{\lambda,\text{deep}}/\mu} + \frac{1}{\mu} \int_0^{\tau_{\lambda,\text{deep}}} B_\lambda(\tau'_\lambda) e^{-\tau'_\lambda/\mu} d\tau'_\lambda(z) \tag{2.5}$$

2.2 Correlated-k

To compute the interaction that molecules have with the light passing through the atmosphere of exoplanets we need to consider the absorption efficiency from the molecules themselves. These are provided to the community in the form of line lists from databases such as ExoMol (Tennyson & Yurchenko, 2017) and HITRAN (Gordon et al., 2017). These molecular line lists contain millions to billions of line transitions which is computationally expensive when calculating the radiative transfer through the atmosphere. Hence, we use the correlated-k technique, which groups absorptions together into predefined spectral bins (Lacis & Oinas, 1991). This technique has been found to be accurate when compared to the computationally expensive line-by-line technique (Garland & Irwin, 2019). Computing the correlated-k tables requires an intermediate step. It requires cross-sections to be computed at a high enough resolution that the spectral lines can be resolved, this can be done using tools such as ExoCross (Yurchenko et al., 2018). Chubb et al. (2020b) made a tool which can generate the correlated-k table from the generated cross sections and has provided this to the community. They use the technique of opacity sampling which enables low-resolution computations while still taking strong opacity fluctuations at high resolution into account (Min, 2017). They created this tool and computed the correlated-k tables for a range of retrieval tools, including NEMESIS, to help the community have up-to-date and consistent opacity sources.

To see how the correlated-k approach is beneficial we need to first consider the mean transmission $\bar{T}(m)$ of an atmospheric layer over a particular wavelength (λ) or wavenumber (ν) interval i.e., $\nu \rightarrow \nu + \Delta\nu$

$$\bar{T}(m) = \frac{1}{\Delta\nu} \int_{\nu}^{\nu+\Delta\nu} \exp\left(- m \sum_{j} k_j(\nu) \right) d\nu \tag{2.6}$$

where m is the total absorber amount (molecule cm^{-2}), and the summation is over all the lines of all the gases contributing to the absorption, where the absorption spectrum of the jth line in the sum (taking into account the volume mixing ratio for each gas) is $k_j(\nu)$ (molecule^{-1}cm^2). Eq. 2.6 needs to be computed with a resolution of $d\nu$ in order to resolve the individual spectral line shapes, given that these may be smaller than the bin-width $\Delta\nu$; this would result in a large number of calculations. It can be seen that the mean transmission can be calculated by only identifying the fraction of the wavenumber space, $f(k)dk$, is occupied by the absorption coefficients

$k + dk$. We can transform Eq. 2.6 into

$$\bar{T}(m) = \int_0^\infty f(k)(-mk)dk. \tag{2.7}$$

If we then define a smooth, single valued, monotonically increasing cumulative function $g(k)$ as

$$g(k) = \int_0^k f(k)dk \tag{2.8}$$

with a unique, smoothly varying inverse $k(g)$, we can transform Eq. 2.7 into

$$\bar{T}(m) = \int_0^1 \exp\left(-k(g)m\right)dg. \tag{2.9}$$

This integral can then be approximated as

$$\bar{T}(m) = \sum_{i=1}^{N} \exp\left(-k_i m\right)\Delta g_i \tag{2.10}$$

where k_i is the value of the k-distribution of the path at the ith quadrature point and Δg_i is the corresponding weight. A Gaussian quadrature scheme is used with $N = 10 - 20$ ordinates.

In Eq. 2.6 it can be seen that $k(\nu)$ is a rapidly varying function of frequency, whereas $k(g)$ is a smoothly varying function of g, hence requiring far fewer integration steps. This is one of the advantages of this approach over the line-by-line approach. To calculate the spectrum of a path, NEMESIS interpolates the correlated k-tables (i.e., those from Chubb et al. (2020b)) for each gas to the path temperature and pressure. If more than one gas contributes to the absorption, the k-tables of the different gases have to be combined. Following Lacis & Oinas (1991), the k-tables are combined assuming that the absorption lines of different gases are not correlated with each other, using the gas volume mixing ratios as weights. Once the overall k-distribution of each path has been calculated we need then to combine several paths together to integrate the radiative transfer equation, as real atmospheres have a vertical structure that is not homogeneous. To be able to perform atmospheric calculations for an inhomogeneous atmosphere, we use the correlated-k approximation. Here, an atmosphere is split up into a suitable number of equivalent homogeneous layers and the k-distributions is then calculated for each layer. It is then found (e.g., Lacis & Oinas (1991)) that regions of high absorption in one layer are usually spectrally well correlated with regions of high absorption in all the other layers, and similarly for regions of middle and weak absorptions.

The mean transmission through the atmosphere can be approximated as

$$\bar{T}(m) = \sum_{i=1}^{N} \exp\left(- \sum_{j=1}^{M} -k_{ij} m_j \right) \Delta g_i \tag{2.11}$$

where M is the number of layers in the atmosphere and k_{ij} is now the value of the k-distribution of the jth layer at the ith quadrature point. It has been found that if the correlated-k approximation is used with 10-20 quadrature points, there is usually less than a 5% difference between correlated-k and line-by-line calculations (Irwin et al., 2008).

2.3 What is a Spectral Retrieval?

One method of studying the atmospheric constituents of an exoplanet is by employing an atmospheric retrieval (Line et al., 2013; Kreidberg et al., 2014; Benneke et al., 2019). Atmospheric retrieval is the act of obtaining the physical and chemical characteristics of an atmosphere based on observations. Observations of exoplanet atmospheres often have a poor signal to noise and different combination of atmospheric parameters can often be compatible with the data. In order to quantify these degeneracies, atmospheric retrievals are often carried out by computing thousands of models allowing to explore a large parameter space and quantify the degeneracies between parameters. However, when performing retrievals on a data set, one has to first carefully choose the forward model that will be used for the data analysis. Such a choice includes a series of assumptions allowing one to reduce the parameter space to explore. These assumptions can sometimes bias the retrieval results towards unrealistic values, leading to precise, but wrong inferences about the atmospheric composition of an exoplanets atmosphere. We explore these biases in this thesis and overview new forward model assumptions in this Chapter.

It must be noted that the scattering assumptions put forward in Section 2.7 are specifically for a retrieval framework, in which scattering has been neglected. Thermal scattering has been neglected in retrieval models of eclipse spectra for a range of reasons, these include: the sparse wavelength coverage of observations, the low number of measured eclipse spectra of hot Jupiters, the current observations of eclipse spectra do not provide evidence for dayside clouds (Parmentier et al., 2016) and the high computation time required to calculate the scattering component of the radiative transfer equation. With the launch of telescopes such as JWST and Ariel, we are

moving into an era where we will obtain a large number of hot Jupiter eclipse spectra with higher resolutions than current space based instruments, hence our retrieval models need to be able to explore the impact that thermal scattering imposes on the observed eclipse spectra, in order to correctly understand the planets atmosphere.

Theoretical forward modelling grids do not concern themselves with the issues stated in the retrieval, this is because the models are precomputed into grids, which can then be rapidly compared to observations. There is an array of literature using forward models which contain scattering (Marley et al., 2002; Gao et al., 2020; Parmentier et al., 2021). Forward models are useful to understand the underlying physics contained within the observations. They also help to guide the retrieval results to ensure that non physical interpretations are avoided.

2.4 Temperature-Pressure (T-P) Parameterisation

The atmospheres of exoplanets span a diverse range of temperatures, thus requiring a flexible parameterisation of the thermal structure to be able to adequately model the vertical structure. Prior to the detection of the thermal inversion in WASP-121b reported in Evans et al. (2017), the mechanisms of thermal inversions in hot Jupiter atmospheres had been long theorised. The presence of TiO and VO absorption at optical wavelengths had been theorised to absorb stellar radiation in the atmosphere of highly irradiated objects which could lead to a stratosphere (Hubeny et al., 2003; Fortney et al., 2008). Therefore, in this thesis we implement a flexible temperature structure parameterisation, which is able to model both inverted and non-inverted thermal profiles.

The T-P parameterisation implemented assumes two independent downwelling visible streams of radiation and one upwelling stream of thermal emission, as the stellar radiation and thermal emission occur at different wavelengths. Two downwelling streams are needed so that a thermal inversion and the greenhouse effect can be modelled, this was not accounted for in the initial development of the parameterisation presented in Guillot (2010).We note that more downwelling streams can be used (Parmentier & Guillot, 2014). Briefly, the temperature as a function of the thermal optical depth, τ, is given by

$$T^4(\tau) = \frac{3T_{\rm int}^4}{4}(\frac{2}{3} + \tau) + \frac{3T_{\rm irr}^4}{4}(1-\alpha)\zeta_{\gamma_1}(\tau) + \frac{3T_{\rm irr}^4}{4}\alpha\zeta_{\gamma_2}(\tau), \tag{2.12}$$

with ζ_{γ_i} is given by

$$\zeta_{\gamma_i} = \frac{2}{3} + \frac{2}{3\gamma_i}[1 + (\frac{\gamma_i\tau}{2} - 1)e^{(-\gamma_i\tau)}] + \frac{2\gamma_i}{3}(1 - \frac{\tau^2}{2})E_2(\gamma_i\tau). \tag{2.13}$$

Here, γ_1 and γ_2 are the ratios of the Planck mean opacities in the two visible streams to the thermal stream where $\gamma_1 = \kappa_{v1}/\kappa_{\rm IR}$ and $\gamma_2 = \kappa_{v2}/\kappa_{\rm IR}$. The parameter α has a range between 0 and 1 and is the weighting used between the two visible streams, κ_{v1} and κ_{v2}. $E_2(\gamma_i\tau)$ is the second order exponential integral function. $T_{\rm int}$ is the internal temperature which gives rise to the heat flux of the planet and it is usually a fixed value as it does not have much effect on the spectra (Thorngren et al., 2019), in general we have fixed it to a value of 100K following Line et al. (2013), a reasonable assumption for hot Jupiters. $T_{\rm irr}$ is the temperature that causes the amount of irradiation the planet receives due to the host star and is of the form

$$T_{\rm irr} = \beta\Big(\frac{R_*}{2a}\Big)^{1/2} T_* \tag{2.14}$$

with R_* and T_* being the stellar radius and temperature respectively, a is the semi-major axis, and β is a parameter that accounts for the albedo, emissivity and day-night redistribution; it is usually on the order of unity. Finally the parameter τ is the grey (independent of wavelength) infrared optical depth

$$\tau = \frac{\kappa_{\rm IR} P}{g} \tag{2.15}$$

where $\kappa_{\rm IR}$ is the mean infrared opacity, P is the pressure in the atmosphere and g is the surface gravity, which we consider to be at the 1 bar pressure level. The profile therefore has five free parameters, these are: α, β, $\kappa_{\rm IR}$, γ_{v1} and γ_{v2}. The parameters γ_{v1} and γ_{v2} control whether there is a temperature inversion.

2.5 H^- Opacity

It has been well known that for brown dwarf and stellar atmospheres in the temperature regime 2000K < T < 8000K, there is the need to consider opacity sources due to H^- (e.g., Lenzuni et al., 1991; Sharp & Burrows, 2007). However it was only until recently, when ultra-hot Jupiters began to be studied in more detail in emission, that it needed to be considered for exoplanets as well (e.g., Arcangeli et al., 2018; Parmentier et al., 2018). At these high temperatures, atomic hydrogen is produced due to the thermal dissociation of H_2 and free electrons are produced due to the ionization of metals in the atmosphere.

This thesis upgraded the NEMESIS code to account for the opacity due to H^-. John (1988) provide the formulae needed to solve for the opacity due to free-free absorption and bound-free absorption of H^-. Here we will briefly overview the processes that cause this to be a source of opacity. At high temperatures, the H_2 molecule dissociates to form a single hydrogen atom; the high temperatures also result in the ionisation of alkali metals such as sodium and potassium, resulting in many free electrons.

The bound-free opacity arises when the H^- ion absorbs a photon according to following interaction:

$$h\nu + \mathrm{H}^- \rightarrow \mathrm{H} + \mathrm{e}^- \tag{2.16}$$

with the absorption (k_λ^{bf} [$\mathrm{cm}^4\mathrm{dyne}^{-1}$]) given by:

$$k_\lambda^{bf}(T) = 0.750 T^{-\frac{5}{2}} e^{\frac{\alpha}{\lambda_0}T}(1 - e^{-\frac{\alpha}{\lambda}T})\sigma_\lambda \tag{2.17}$$

where $\lambda_0 = 1.6149$ microns and is the photo-detachment threshold. For an in depth explanation of this equation and its variables, see John (1988). The H^- opacity resulting from the bound-free interaction is the dominating opacity in the Hubble WFC3 spectral region, specifically covering the spectral range $0.125 \leq \lambda \leq 1.6149$; this is shown graphically by the pink dotted line in Figure 2.1.

The second form of opacity that arises is from a free-free interaction, where photons can be absorbed by electrons that are interacting with neutral hydrogen

$$h\nu + \mathrm{e}^- + \mathrm{H} \rightarrow \mathrm{H} + \mathrm{e}^- \tag{2.18}$$

and has the absorption (k_λ^{ff} [$\mathrm{cm}^4\mathrm{dyne}^{-1}$]) given by:

$$k_\lambda^{ff} = 10^{-29} \sum_{n=1}^{6} \left(\frac{5040}{T}\right)^{(n+1)/2} \times(\lambda^2 A_n + B_n + C_n/\lambda + D_n/\lambda^2 + E_n/\lambda^3 + F_n/\lambda^4). \tag{2.19}$$

The coefficients can be found in John (1988). The free-free absorption produces opacity at all wavelengths i.e, $0.125 \leq \lambda \leq \infty$, although it does not become important until the infrared as seen from the dotted green line in Figure 2.1.

We verified that the implementation of the H^- calculation was correct by comparing it to Parmentier et al. (2018), the results are shown in Figure 2.1. Since incorporation, the H^- calculation implemented in this thesis has led to a range of publications, including the planet HAT-P-41b (Lewis et al., 2020), WASP-79b (Ratchke et al., submitted) and WASP-121b (Mikal-Evans et al., submitted). In (Lewis et al., 2020), three retrieval codes analysed the transmission spectrum of the planet HAT-P-41b

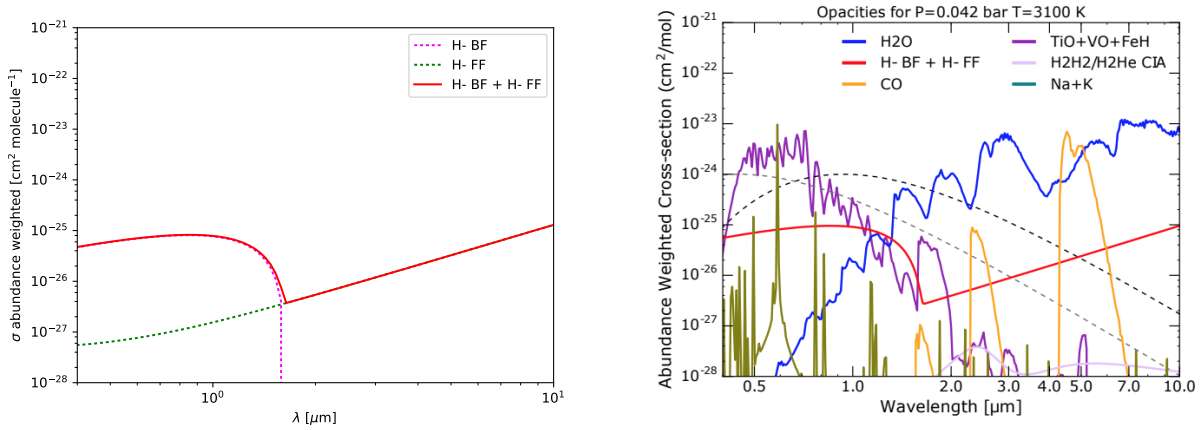


Figure 2.1: Left: The bound-free and free-free absorption cross sections of the negative hydrogen ion using equations taken from John (1988). Right: Absorption cross sections for a given pressure and temperature taken from Parmentier et al. (2018). Reproduced with permission from Astronomy & Astrophysics, © ESO.

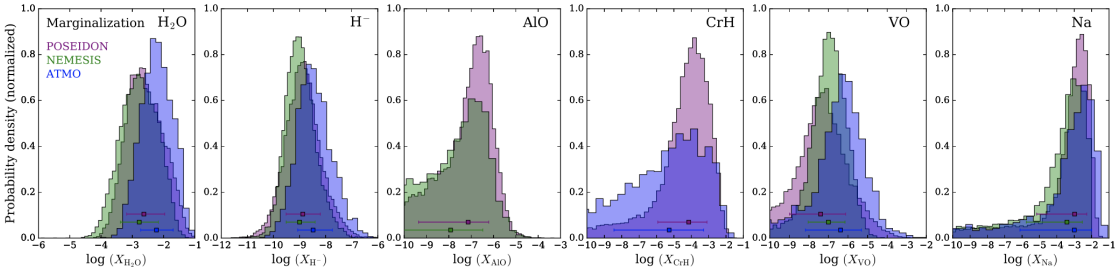


Figure 2.2: The retrieved chemical abundances presented in Lewis et al. (2020). The histograms show the marginalised probability distributions for the volume mixing ratios for each molecule used in their respective retrieval code. With NEMESIS in green, ATMO in blue and POSEIDON in purple. Reproduced by permission of the AAS.

and retrieve consistent abundances for the H^- opacity in the atmosphere, as seen in Fig 2.2. This confirms that the implementation of the calculation is consistent with other radiative transfer codes.

2.6 2-D and Dilution Parameterisations

Planets are 3-D objects, with their thermal structure, chemical composition and cloud coverage varying as a function of altitude, latitude and longitude. To first order approximation, retrieval studies tend to assume that the planet is a 1-D object, where the disc of the planet is homogeneous and there is only variations in altitude. It

was shown by Feng et al. (2016) that if the temperature contrast between the day and nightside of a hot Jupiter is large, this effect will be detectable with current and future space-based instruments and could also cause spurious detections of molecules, if not properly accounted for. They consider a tidally-locked exoplanet at quadrature, i.e., where we see the planet with the terminator on the central meridian. They then develop composite models which are formed from different temperature contrasts from day to nightside and then they retrieve on these models considering the wavelength coverage and noise from JWST.

In this thesis we develop a general approach to this technique by considering that the coverage of the hot and cold parts of the planet are unknown quantities and retrieve them independently. This can also be used to study the dayside of ultra-hot Jupiters which exhibit large temperature contrast between their hot spot and the rest of the visible disc. To do this we employ a linear weighting scheme

$$F_{\text{weighted}} = xF_{\text{hot}} + (1 - x)F_{\text{cold}}, \tag{2.20}$$

where F_{hot} is the spectrum generated from a hot 1-D TP profile, F_{cold} is the spectrum generated from a cooler 1-D TP profile and x represents the weight applied to the hotter profile and is a free parameter in our retrievals. This technique, developed in this thesis and published in Taylor et al. (2020), has since been used to study the spectral phase curve of WASP-43b to constrain the hotspot shift and retrieve the chemical abundances (Feng et al., 2020). We apply this developed technique in more detail in Chapter 3 and explore where the biases in retrieval come from.

To complement the 2-D parameterisation, we also consider a simplified version by *a priori* assuming that the colder part of the planet is so cold that it does not contribute to the disc averaged emission spectrum at all, effectively having zero flux output. Equation 2.20 can then be simplified as a dilution of the hot part of the planet as follows

$$F_{\text{diluted}} = xF_{\text{hot}}, \tag{2.21}$$

The parameter x effectively scales the 1-D forward model F_{hot} to fit to the observations. The forward model will be of a higher temperature than the disc average as it is seeing a smaller emitting area on the disc of the planet, this is demonstrated in Chapter 3. The scaling is wavelength independent and mutes the features equally.

The "dilution" factor, x, retrieved is consistent with the weighting of the hot profile, which is shown in Chapter 3 to be consistent with the 2-D approach. The technique gives freedom for the retrieval to adjust to accommodate systematics in the

observations as well as account for the non 1-D nature of the spectrum. This technique is useful to use as it reduces the number of free parameters needed to conduct a meaningful retrieval simulation (extra parameter compared to the parameters needed to simulate a second TP profile). We define a meaningful retrieval to be one which is data-driven and not driven by the model. We aim to seek the optimal information content contained within the data (Line et al., 2012). There are some retrieval studies that add multiple different molecules to their forward models to determine the presence of such molecules in the atmosphere. This is a dangerous technique, as adding more parameters gives the model more freedom to fit the observations in nonphysical ways (e.g., MacDonald & Madhusudhan, 2017; Chubb et al., 2020a). The dilution retrieval makes sense to use when considering an emission spectrum where the colder part of the planet is much colder than the hotter part, hence being completely dominated by the spectral features in the hotter region. For the large temperature contrast, the colder region could also be seen as a cloudy profile (Irwin et al., 2020).

2.7 Single Scattering Albedo (SSA) Parameterisation

The importance of clouds, particularly their scattering properties, in exoplanet emission spectra has been highlighted in the context of directly-imaged planets and brown dwarfs (Lee et al., 2013; Lavie et al., 2017; Burningham et al., 2017; Mollière et al., 2020). However, the effects of scattering on the emission spectra of transiting exoplanets has been relatively unexplored; it was thought that the complicated effects of multiple scattering were negligible for the data quality. Barstow et al. (2014) used optimal estimation and a grid model search to study the effects of multiple scattering on the dayside reflectance spectrum of HD189733b, but found little evidence of strong reflection. de Kok et al. (2011) explore the effects of multiple scattering using forward models and their findings suggest that the scattering of clouds in thermal emission can cause up to a 10% difference in spectra compared to their cloud-free counterpart.

An additional consideration is the way that cloud parameterisations are treated within Bayesian retrieval frameworks, usually relying upon *a priori* knowledge of which condensate species are most prominent. For example, the retrievals conducted in Venot et al. (2020) assume[1] the species of the cloud *a priori*. Hence, they use fixed properties for the cloud such as its mean molecular weight and SSA. Given that such

[1]The emission retrievals with TauREx and Pyrat Bay used in this work did not account for multiple scattering in emission.

assumptions cannot generally be made *a priori* when exploring the atmosphere of an unknown planet, it would be preferable to take a more agnostic approach, e.g., by using general parameterisations styles that can encompass a range of cloud compositions and configurations. Given that the scattering properties of clouds depend on the real and imaginary refractive index as well as on particle size, these three properties are frequently retrieved simultaneously for the solar system planets (which generally entail in situ high spatial resolution, high signal-to-noise spectra at multiple viewing angles) (Irwin et al., 2015; Toledo et al., 2019; Braude et al., 2020). This technique requires a large number of free parameters, which is problematic for typical exoplanet spectral coverage and precision (even for JWST quality). Instead, we propose a "middle ground" parameterisation that fits for a simplified SSA wavelength dependence of the cloud species, as this property encompasses the effects of both the real and imaginary index spectra and the particle size. In this approach, we are agnostic to the chemical and physical properties of the cloud.

For this parameterisation the cloud is assumed to be a uniformly mixed grey opacity throughout the whole atmospheric column and the scattering phase function is assumed to be isotropic. We model the SSA as a step function with one break point. The parameters are the SSA value before the break, the wavelength of the break, and the SSA value after the break. We call this retrieval style the "three-parameter" case as three free parameters are used to constrain the SSA. More break points could be added in future, but we adopted this prescription because it keeps the number of free parameters low, while adequately capturing the shape of the SSA spectrum of many cloud condensing species (Figure 2.3).

We explore the biases and degeneracies involving multiple scattering in the thermal infrared in Chapter 4.

2.8 Nested Sampling

The retrieval framework used in the classical NEMESIS framework is not ideally suited to exoplanet studies since it assumes an a priori solution, and tries not to vary too far from it. The reason why the classical framework does not deviate too far from the prior solution is because the algorithm tries to minimise the cost function, which relies on the solving the difference between the a priori and measured atmospheric state vectors, more details can be found in Irwin et al. (2008). Therefore, Garland (2018) wrapped the radiative transfer model in a Bayesian framework, opting for the Nested Sampling approach, implemented into NEMESIS by using the open source

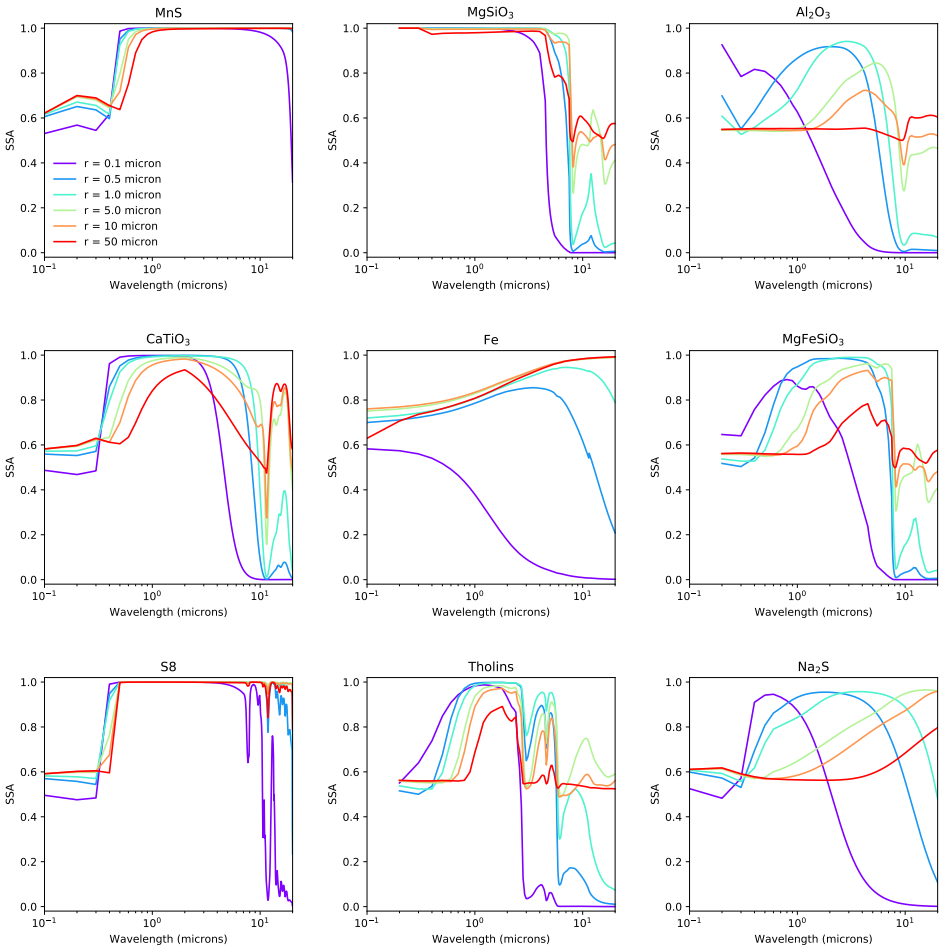


Figure 2.3: Common cloud species found in exoplanet atmospheres and their single-scattering albedos. They are calculated for particle radii of 0.1, 0.5, 1.0, 5.0, 10.0 and 50.0 μm over a wavelength range of 0.1 – 20 μm for MnS, S_8, Fe and $CaTiO_3$ and a wavelength range of 0.2 - 20 μm for $MgSiO_3$, $MgFeSiO_3$ and Al_2O_3. Caution needs to be taken when interpreting the results from MnS as the optical constants used in the infrared were inferred from ZnS and Na_2S rather than laboratory experiments (Kitzmann & Heng, 2018).

package PyMultiNest (Buchner et al., 2014). This technique is efficient in exploring large parameter spaces by distributing ellipsoids that constrain the regions of highest likelihood (Feroz & Hobson, 2008; Feroz et al., 2013); this also allows for multimodal distributions to be found, which is important when the problem of studying the atmospheres of exoplanets can be degenerate or bimodal. An example of retrieved atmospheric parameters are shown in Figure 2.4.

This form of sampling the parameter space is underpinned by Bayes' theorem which states

$$P(\theta|x, M) = \frac{\mathbb{L}(x|\theta, M)Pr(\theta, M)}{P(x, M)} \tag{2.22}$$

where $P(\theta|x, M)$ is the posterior probability of parameters θ given a data set x and assuming a model M. $Pr(\theta, M)$ is the Bayesian prior based on the parameters given a certain model, constrained by the physics of the problem. The likelihood function is given by $\mathbb{L}(x|\theta, M)$, which gives how likely to find x given θ and M; usually this can be considered Gaussian if we assume independent Gaussian noise on the measurements. The denominator $P(x, M)$ is the Bayesian evidence, it is used to test the adequacy of the model and is given by the equation needed to normalise the numerator

$$P(x, M) = \int \mathbb{L}(x|\theta, M)Pr(\theta, M)d\theta \tag{2.23}$$

2.8.1 Why Nested Sampling over MCMC?

Markov Chain Monte Carlo (MCMC) is another sampling technique that is used to find the probability distribution of the parameters explored, giving us the "best-fitting" results. It is similar to the Nested Sampling approach, in that it is driven using Bayes' theorem, but there are two major differences. The first difference is the technique it uses to explore the parameter space. MCMC uses a random walk process by building Markov Chains, with each chain having a higher likelihood of being the "true" value. This technique has a pitfall when it comes to exploring degenerate problems as it cannot model multimodal distributions. The chains could converge in a local minimum in a specific part of the parameter space which may not encompass all the possible results. Nested sampling, on the other hand, distributes nested shells around the parameter space, shrinking the shells when exploring parameter spaces of higher likelihood. When exploring the parameter space, the nested shells can explore multiple regions of highly probable likelihood, hence finding multimodal results.

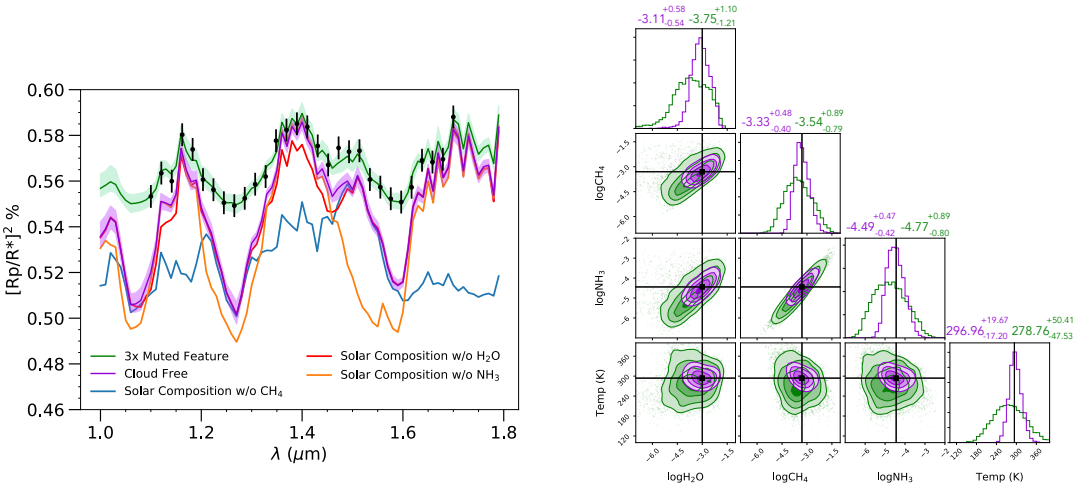


Figure 2.4: Simulated observations of HIP41378 f (Santerne et al., 2019) for a clear atmosphere (purple) and for clouds reducing the signal by 2/3 (green). We also show cases with either water (red), methane (blue) or ammonia (orange) are artificially removed to highlight the detectability of different spectral features. The corner plot shows the retrieved posterior distribution of relevant parameters for both cloudless (purple) and cloudy (green) cases (we omit cloud parameters, planetary radius and reference pressure from the plot). NH_3, CH_4 and H_2O abundances can be retrieved with a precision of 0.5 dex in the clear case and 0.8 dex in the cloudy case. Overall, a reduction of more than a factor of 10 in the strength of the spectral features (due to an unlikely high metallicity ($> 300\times$ solar) or an unexpectedly high cloud deck) would be needed to completely mute the signal.

The second advantage of using nested sampling over MCMC is the ability for nested sampling algorithms to rapidly compute the Bayesian evidence which can be used for model comparison.

2.8.2 Bayesian Evidence and Model Selection

We use Bayesian model comparison to evaluate the statistical significance of one retrieval model over another (e.g., Ford & Gregory, 2007; Schulze-Hartung et al., 2012). We compute the Bayes factor $\ln B = \ln P(x, M_2) - \ln P(x, M_1)$, where $P(x, M_1)$ and $P(x, M_2)$ are the evidences for the model 1 and model 2, respectively, as calculated in the nested sampling algorithm using Equation 2.23. If the Bayes factor is significantly less than unity ($\ln B < 0$), the data supports model 1. If it is significantly greater than unity, the reverse is true. If $|\ln B|$ is close to zero, one cannot discriminate between the two models. It is common practice, when using the Bayes factor for model comparison, to interpret the results using the adapted Jeffrey scale (Kass & Raftery,

1995). For example, the preference for model 2 over model 1 is considered statistically significant only if $\ln B > 3$. However, our target audience of astronomers and planetary scientists is most familiar with degrees of significance expressed in terms of the number of standard deviations, σ (these are directly related to confidence intervals if the distribution in question is Gaussian). To make our results easily accessible to this audience, we converted our $\ln B$ values to a number of standard deviations, following the prescription of Trotta (2008). We then consider a particular model to be strongly favoured if it is supported at the $> 3.6\,\sigma$ level. We use $> 3.6\,\sigma$ as this is what $\ln B > 3$ is when converted into number of standard deviations.

Chapter 3

Understanding and Mitigating Biases of Inhomogeneous Emission Spectra with JWST

The contents of this Chapter has been published in the Monthly Notices of the Royal Astronomical Society, the study can be found here Taylor et al. (2020). The analytical derivation in 3.2 was done jointly with my supervisor Prof. Vivien Parmentier. The abundances presented in Table 3.1 were calculated by Dr Elspeth Lee. The rest of the content in this Chapter are my contributions only.

3.1 Introduction

In this chapter we will look specifically at the assumption that atmospheres are horizontally homogeneous. Such a 1-D assumption has been widely used to study exoplanet atmospheres (e.g., Kreidberg et al., 2014; Barstow et al., 2017; Wakeford et al., 2018; Evans et al., 2017, 2018). However, it is clear that the atmosphere of exoplanets are often intrinsically three-dimensional. In the specific case of tidally-locked hot Jupiters, the large irradiation received on the dayside and the poor day-to-night heat redistribution can lead to variations of up to a thousand degrees between the dayside and the nightside (Showman & Guillot, 2002; Knutson et al., 2007; Parmentier et al., 2016).

Recently, Feng et al. (2016) showed that when retrieving the spectrum of an inhomogeneous planet with a 1-D model the inferred molecular abundances could be strongly biased. In several cases, this could even lead to spurious molecular detections. They concluded that such biases can already be seen in current data, but will likely be much stronger when better observations become available. For their JWST-like

simulations (λ = 1 – 10 μm) they find that 2-D effects become significant if the temperature contrast between two thermal profiles observed at planetary quadrature is larger than 40%. One thing that Feng et al. (2016) did not explore is what the cause of the spurious molecular detections that they found were.

This study follows on from the study of Feng et al. (2016). Our goal is understand the mechanisms leading 1-D retrieval models to infer the presence of spurious atmospheric constituents when applied to observations from inhomogeneous atmospheres.

3.2 Analytical Description

We start by deriving an analytical model to determine what precision and wavelength range are necessary to detect the presence of horizontal inhomogeneities based on a single spectrum only. In order to simplify the problem we will assume that a fraction $x = x_0$ of the visible disc emits like a blackbody at the temperature $T_{\rm hot} = T_0$ whereas the rest of the disc is not emitting any light (i.e., $T_{\rm cold}$=0). The resulting spectrum, plotted in Fig. 3.1 is therefore a blackbody spectrum diluted by a factor x_0.

As shown by the lines crossing in Fig. 3.1, for a given wavelength λ_0, the flux $F(\lambda_0)$ that is observed could also correspond to a planet with a hotter hot part covering a smaller area or a colder hot part covering a larger area. Indeed if observations at a single wavelength are made there is an intrinsic degeneracy between the temperature of the hot region and the area covered by it. If we write the hot temperature as $T_{\rm hot} = \beta T_0$, we can write that the flux emitted by the planet is:

$$F(\lambda) = xB(\beta, \lambda) \times \frac{\pi a^2}{D^2}, \tag{3.1}$$

Where a is the planet radius and D is the distance from the Earth and $B(\beta, \lambda)$. For convenience we will now assume $\frac{\pi a^2}{D^2} = 1$. $B(\beta, \lambda)$ is the Planck function taken at a temperature $T = \beta T_0$:

$$B(\beta, \lambda) = \frac{2hc^2}{\lambda^5} \frac{1}{e^{\frac{hc}{\lambda k \beta T_0}} - 1}, \tag{3.2}$$

The total flux emitted by the planet at a given wavelength can be written:

$$F(\lambda) = x_0 B(\beta_0, \lambda), \tag{3.3}$$

For a specific wavelength λ_0, the ensemble of models that can match the planetary flux is described by :

$$F(\lambda_0) = x_0 B(\beta_0, \lambda_0) = xB(\beta, \lambda_0). \tag{3.4}$$

This can also be written as a relationship between β and x:

$$x = \frac{x_0 B(\beta_0, \lambda_0)}{B(\beta, \lambda_0)}. \tag{3.5}$$

We can see that at a given wavelength λ_0, there exists a continuous ensemble of solutions (β,x) that can match the planetary flux. However, as is seen if Fig. 3.1, the different solutions will diverge and become distinguishable away from λ_0. We now wonder what additional observations could allow us to distinguish between the real planet parameters x_0, β_0 and the ensemble of solutions degenerate at $\lambda = \lambda_0$. We first write the flux of one of these solution as:

$$F(\lambda) = xB(\beta, \lambda) = \frac{x_0 B(\beta_0, \lambda_0)}{B(\beta, \lambda_0)} \times B(\beta, \lambda)\,. \tag{3.6}$$

Now let us imagine that we have two observations, one at a wavelength λ_0 and one at a wavelength $\lambda_0 + \Delta\lambda$. We want to derive a criteria to understand what signal-to-ratio would be necessary to disentangle between the true solution and a planet model where the temperature of the hot part of the atmosphere differ from the cooler part by $\Delta\beta$.

If the difference between the profiles is larger than the error on the measurement (σ_{F_p}) then the model at $\beta_0 + \Delta\beta$ will not be a good fit to the observations. This can be written as:

$$|F(\lambda_0 + \Delta\lambda, \beta_0, x_0) - F(\lambda_0 + \Delta\lambda, \beta_0 + \Delta\beta, x_0)| > \sigma_{F_\mathrm{p}} \tag{3.7}$$

We now suppose that we try to disentangle two models that differ by a small value $\Delta\beta$. We further assume that the model fluxes are approximately linear over the wavelength range $\Delta\lambda$ considered. This last approximation would hold best away from the peak of the Planck function.

We perform a Taylor expansion on Eq 3.7 of order one as a function of β and λ, which leads to the following equation:

$$\frac{\partial}{\partial\beta}\Big(\frac{\partial F}{\partial\lambda}\Big)_{\lambda_0,\beta_0} \Delta\lambda\Delta\beta > \sigma_{F_p}. \tag{3.8}$$

We now divide both sides of 3.8 by the flux (F_p) and define the signal-to-noise ratio as SNR= $F_p/\sigma_{F_\mathrm{p}}$, hence we obtain a criterion for the detectability of spatial inhomogeneities in a planet atmosphere:

$$\frac{1}{F_p}\frac{\partial}{\partial\beta}\Big(\frac{\partial F}{\partial\lambda}\Big)_{\lambda_0,\beta_0} \Delta\lambda\Delta\beta > \frac{\sigma_{F_p}}{F_p} \approx \frac{1}{SNR}. \tag{3.9}$$

We note that this equation can be seen as a function of λ_0 and β_0 or as a function of λ_0 and x_0 since β_0 and x_0 are related by Eq 3.5.

We use this criterion to show the ability to disentangle 2-D structures for a planet with a hot isotherm of 1400K covering different fraction of the visible planetary disc, x_0 in Fig. 3.2, we chose to model a wavelength coverage of $\Delta\lambda = 2\mu m$ to represent the majority of bandpasses covered by JWST instruments. We see from the plot that the contour lines do not vary much with the hot profile covering fraction, x_0. Secondly we see that as we increase the central wavelength, the ability to disentangle the inhomogeneous structures becomes harder, requiring a higher SNR. Lastly, the contour lines scale with the temperature contrast $\Delta\beta$ as seen from Eq 3.9, with a larger temperature contrast shifting the contour lines to the right, hence requiring a lower SNR, this effect is marginal.

We can see that the contour line at 1 micron corresponds to a SNR ~ 1 for a low contrast ($\Delta\beta = 0.2$) This means that with the observation centred at 1 micron, and a wavelength coverage of 2 microns ($\Delta\lambda$), we are able to easily disentangle 2-D effects even if the secondary eclipse is measured with an SNR of 1 only. The SNR required increases as we move to longer wavelengths, where at 10 microns we need a SNR in the range 10 – 100. To conclude, we find that observing shorter wavelengths and a large wavelength coverage is best to disentangle temperature inhomogeneities from a disc-averaged spectrum.

3.3 Model Setup

3.3.1 Composite Spectra

We have now explored the impact that an inhomogeneous thermal structure can have when considering blackbody planetary spectra. We now want to explore with more realistic planetary spectra. Similarly to Feng et al. (2016) we build a uniformly mixed, cloud-free model atmosphere assuming that part of the atmosphere is hotter than the rest. We now want to model the spectrum of a horizontally inhomogeneous planet atmosphere. For this we assume that a projected fraction x of the planet hemisphere we are looking at is hotter. To do this we employ a linear weighting scheme

$$F_{\text{weighted}} = xF_{\text{hot}} + (1-x)F_{\text{cold}}, \tag{3.10}$$

where F_{hot} is the spectrum generated from the hot 1-D TP profile, F_{cold} is the spectrum generated from the cooler 1-D TP profile and x represents the weight applied to the hotter profile and is a free parameter in our retrievals. We vary the weights used

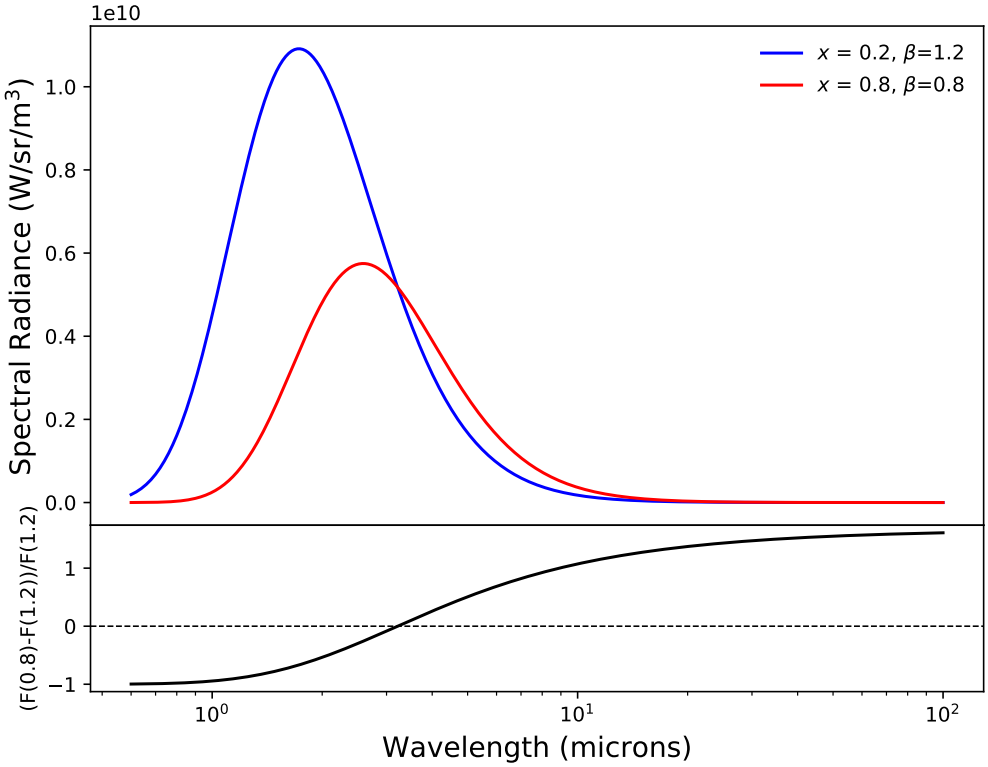


Figure 3.1: Plot showing two planetary spectra considering that a part x of the atmosphere emits like a blackbody and the other part is not emitting any light. The blue curve has a β value of 1.2 and the red curve has the value of 0.8, the function has been plotted using Eq 3.6. The hotter profile covers a smaller fraction of the surface ($x = 0.2$), the opposite is true for the colder profile ($x = 0.8$). For a given wavelength, there exists more than 1 combination of these parameters which give the same flux output.

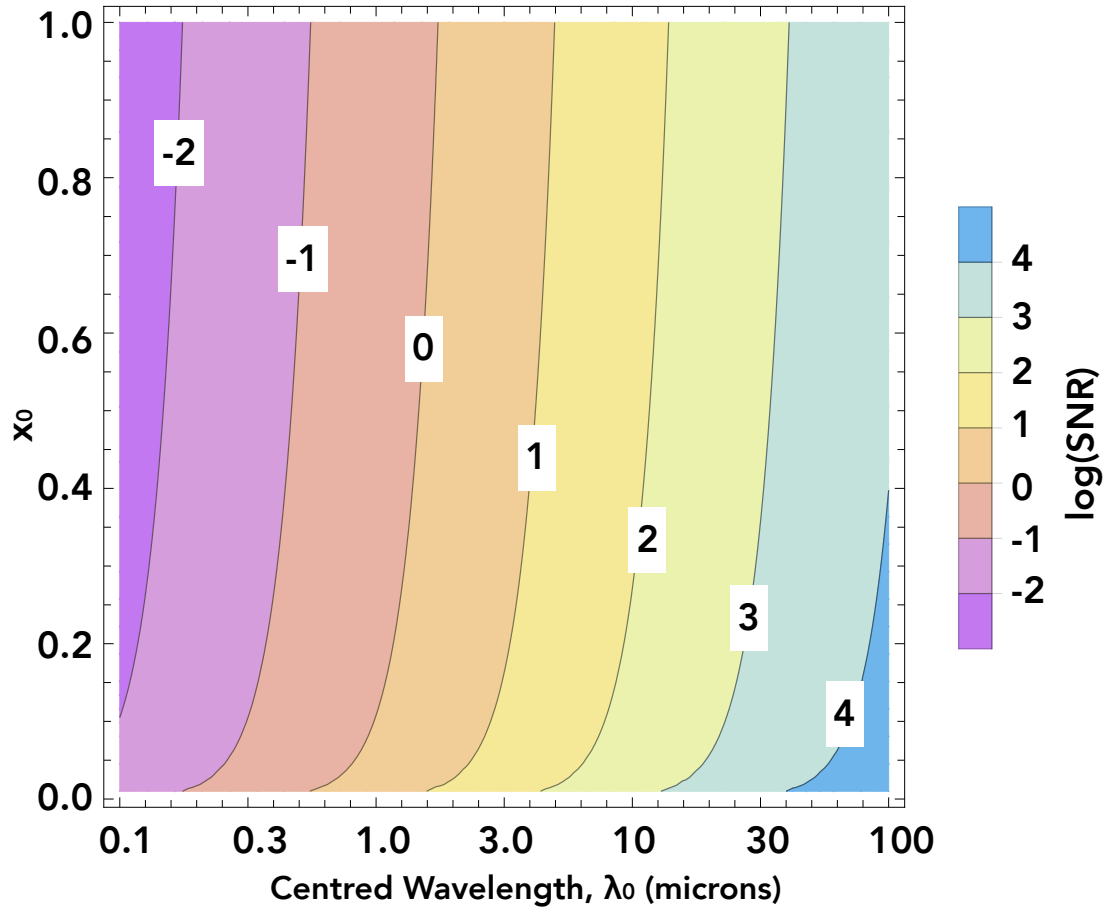


Figure 3.2: Ability to disentangle between a planetary spectrum with a hot region with a temperature of 1400K covering a fraction x_0 of the surface and a planetary spectrum with a colder region of $\beta_0 + \Delta\beta = 0.8$, where $\beta_0 = 1$. Hence the colder region has a temperature of $(\beta_0 + \Delta\beta) \times 1400 = 1120$K. For the colder planetary case the emitting part of the planet covers a larger fraction in order to have the same flux at λ_0. The SNR are calculated following Eq. 3.9 assuming a wavelength range $\Delta\lambda = 2\mu m$ centered at different λ_0 as shown by the x-axis. The plotted threshold can be extrapolated to different contrasts by noting that the SNR scales inversely with the temperature contrast $\Delta\beta$. Note that shorter wavelengths are more important in being able to detect 2-D effects. Increasing the contrast of the profiles shifts the contour lines to longer wavelengths, however the effect is still marginal.

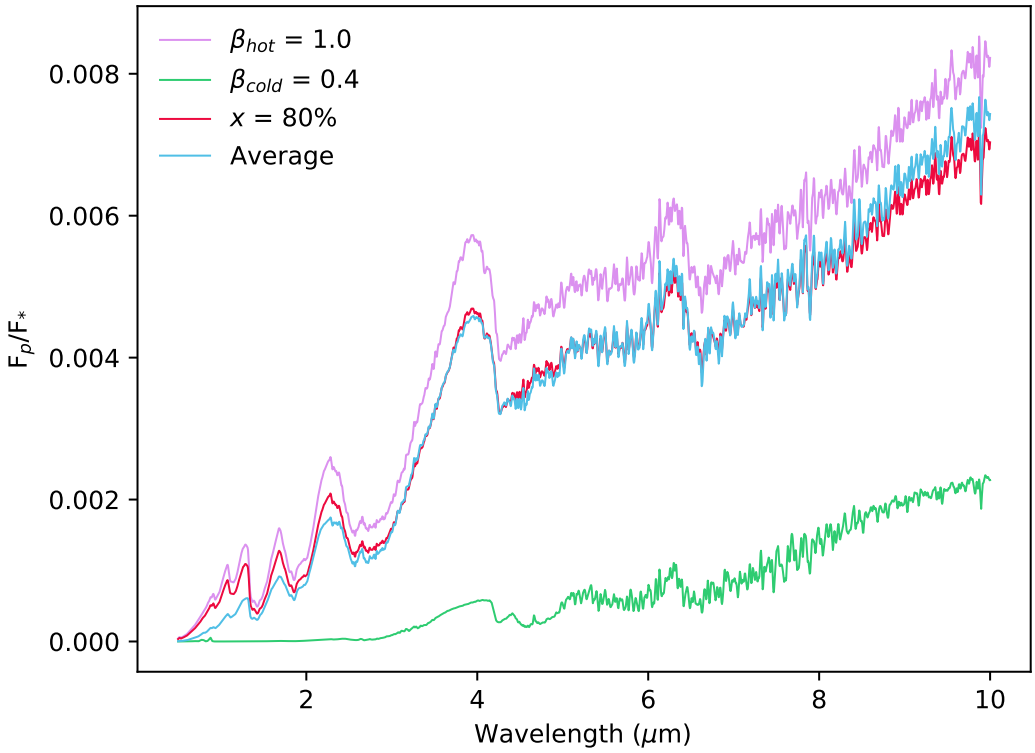


Figure 3.3: Spectra for the hot ($\beta_{\rm hot} = 1$, magenta) and cold ($\beta_{\rm cold} = 0.4$, green) profiles, alongside the composite spectrum (red) produced with a weighting of x= 80%. For comparison, we also show (in blue) a spectrum generated using the average of the hot and cold TP profiles ($T^4_{\rm average} = \frac{1}{2}(T^4_{\rm hot} + T^4_{\rm cold})$). Note the small, but visible differences between the composite and average spectra, especially at shorter wavelengths.

to generate the observed spectra to be x = 80%, 60%, 40% and 20%. Figure 3.3 gives an example of how the observed spectrum was generated for a weighting of 0.8. In physical terms, if the hot and cold profiles correspond to the day- and nightside respectively, then the weights x = 80%, 60%, 40% and 20% represent approximately a planet observed at phase angles of $\theta = 144°$, 108°, 74° and 36° respectively (also $360° - \theta$). While we show that these simulations *mimic* the observations obtained of a spectral phase curve, they can also be applicable to a single secondary eclipse spectrum.

3.3.2 Treatment of angles

We appreciate that when observing a planet at different points in its phase there is a need to consider different zenith angles at which a hot spot might be observed. However, we chose to fix the zenith angle to be 45° for all simulations to reduce the layer of complexity. It has been shown by Irwin et al. (2020) that for a 1-D retrieval, the assumed zenith angle has second order effects on the temperature-pressure profile; as our technique is a combination of two 1-D models, it should not have an extreme influence.

As we are focusing on the abundances retrieved rather than the temperatures, having a fixed zenith angle is a useful approximation. If the hotter region of the planet was modelled with a varying viewing angle, the retrieval would have to adjust the TP profile shape to compensate, which might effect the retrieved abundances.

3.3.3 WASP-43b

The planet and stellar parameters are based on the exoplanet WASP-43b and its star discovered by (Hellier et al., 2011), we present the key parameters used in the modelling in Table 3.1. We use these parameters to generate a stellar spectrum from the Kurucz ATLAS9 model atmospheres (Castelli & Kurucz, 2003). We use the average TP profile and assume equilibrium chemistry to calculate the volume mixing ratios (VMR) using GGchem (Woitke et al., 2018) and take the approximate values at 100 mbars to create a uniformly mixed atmosphere; these values are also listed in Table 3.1. We appreciate that the atmospheres may not be uniformly mixed and that the different profiles may have different chemistry if the atmosphere is not quenched (Moses et al., 2011; Changeat et al., 2019). We aim to explore this in a later study. For this study we use two TP profiles with a large contrast, representative of the expected day-night contrast for some hot Jupiters. Specifically, our model atmosphere is based on WASP-43b, which is known to have a day-night contrast of ∼1000K (Kataria et al., 2015; Mendonça et al., 2018; Morello et al., 2019). The cold and hot profiles are consistent with retrieved TP profiles of the nightside and dayside respectively found in Stevenson et al. (2017). Other hot Jupiters have been shown to have even larger day-night contrasts (Komacek & Showman, 2016; Parmentier et al., 2016), so our present study is by no means an extreme case.

Chemistry		Planet		Star		TP	
logH_2O	-3.42	R_P (R_J)	1.036	R_* ($R_\odot$)	0.667	log κ_{IR}	-1.0
logCO	-3.34	M_P(M_J)	2.052	T_* (K)	4520	log γ_1	-1.0
logCO_2	-6.63	log(g) (cm s^{-2})	3.69	M_*($M_\odot$)	0.717	log γ_2	-1.0
logCH_4	-8.20	T_{int} (K)	200	[Fe/H]	-0.01	α	0.5
		a (AU)	0.01526			β_{hot}	1.0
						β_{cold}	0.4

Table 3.1: Values used to create the forward model atmospheres. In column 1 we present the volume mixing ratios of the molecules which make up the atmosphere, with the rest of the atmosphere consisting of 85% H_2 and 15% He. In column 2 and 3 we present the physical parameters of the planet WASP-43b and the star WASP-43 respectively (Gillon et al., 2012). In column 4 we present the parameters used to create the two temperature-pressure profiles used in this study.

3.3.4 Application to NIRSpec

Once the weighted spectrum is generated (i.e., the red spectrum shown in Fig. 3.3) it is binned to the wavelength grid of the different instruments in this study. We used PandExo (Batalha et al., 2017) to generate the wavelength grid and noise for the NIRSpec Prism (0.6 – 5.3 μm), NIRSpec G395M (2.87 – 5.10 μm), NIRSpec G235M (1.66 – 3.07 μm) and NIRSpec G140M (0.97 – 1.84 μm), this is done for the integration time of the secondary eclipse of WASP-43b. For the NIRSpec Prism (nominal resolving power ∼100) we use the resolution of the largest bin step as shown in Krissansen-Totton et al. (2018) and for the different NIRSpec gratings (nominal resolving power ∼1000) we use a resolution of R=100.

We chose to focus this study on the various NIRSpec instrument modes (G140M, G235M, G395M and Prism) as these will be used for transiting exoplanet observations and also provide a large overlapping wavelength grid. We decided to also use the medium resolution gratings (R $\sim$ 1000) as opposed to the higher resolution gratings (R $\sim$ 2700) to test the lower limits of the resolution obtained by JWST. We ask, is the wavelength coverage of these instruments good enough to break the degeneracy, hence requiring a 2-D approach to better analyse the observations? And, if it is possible to retrieve the 2-D effects, is there evidence to support a 2-D approach over a 1-D approach?

We note that the NIRSpec Prism will saturate for bright targets and so for brighter objects an observer would opt to use the gratings (Stevenson et al., 2016). The gratings provide a much smaller wavelength coverage so an observer may want to combine observations of different gratings. We investigate if by combining G235M and G395M we can recover information better than if we just had observations of

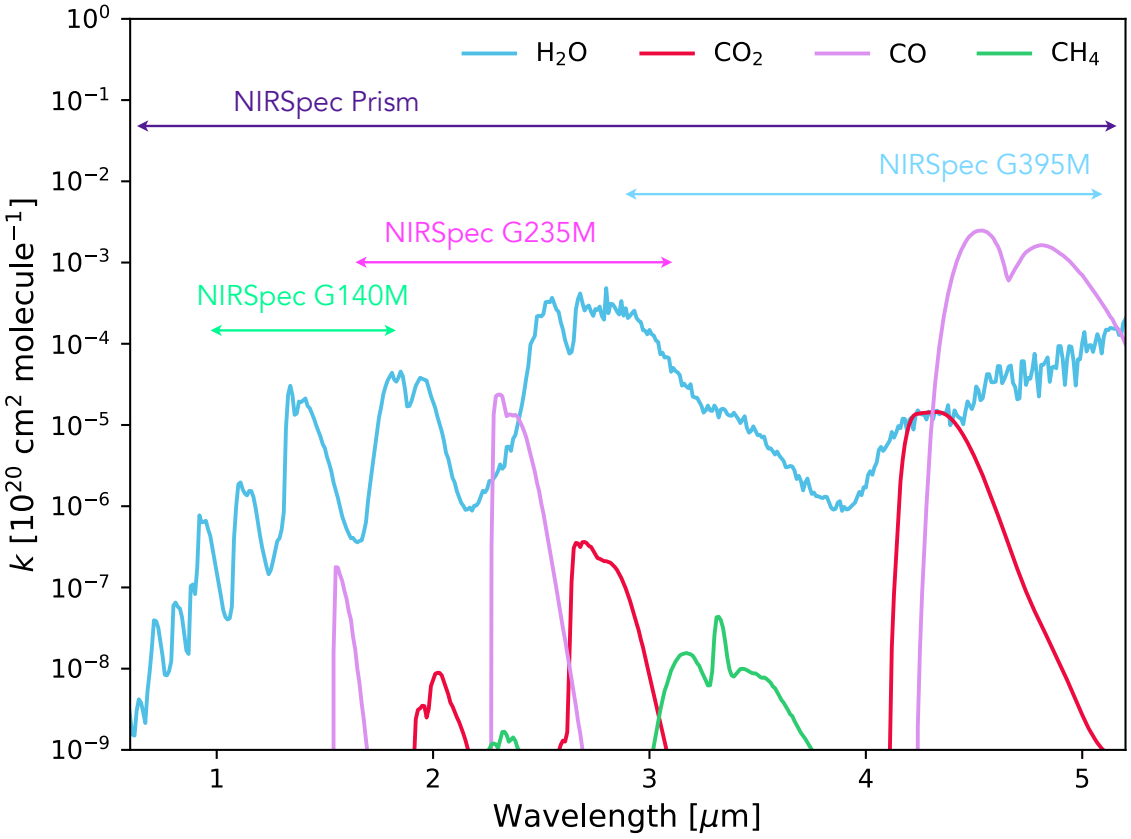


Figure 3.4: The weighted-by-abundance absorption coefficients of the molecules used in this study. We have highlighted the wavelength coverage of each of the instruments. The absorption coefficients are calculated at a temperature of 1450K and pressure of 0.1bar.

the individual gratings; in addition, we test if we are biasing our retrievals when we do not combine the instruments. It has been shown that combining observations can introduce biases in the retrieval and so systematic correction also needs to be considered (Barstow et al., 2015).

3.4 Retrieval Results

We retrieve on the model atmospheres with 3 different retrieval styles: a 1-D model (i.e., $F_{\text{1-D}} = F_{\text{average}}$, where F_{average} is the disc-averaged spectrum assuming a homogeneous temperature profile), a 1-D model with a free parameter, which is able to dilute the spectrum ($F_{\text{dilution}} = xF_{\text{average}}$) and then a model with 2 TP profiles which follows Eq 2.20, this model is 2-D. These will be referred to as 1-D, dilution and 2-D styles respectively from now on. These parameterisations were discussed in Chapter

2.

We aim to show which atmospheric retrieval style is most appropriate in retrieving on an atmosphere which has 2 TP profiles. The results of these simulations are shown in Table 3.2 and are for the different planet types: with 80%, 60%, 40% and 20% weighting applied to the hot profile, where the hot profile has a $\beta_{\rm hot} = 1.0$ and the cold profile has a $\beta_{\rm cold} = 0.4$. These results are instructive: they show when there is evidence to suggest that 2 TP profiles and also a more simple dilution retrieval will be needed to perform a more robust analysis of data obtained from different NIRSpec observing modes. Alongside the σ-significance of the retrieval method, we have presented whether or not the retrieved chemistry is biased (B) or unbiased (U). For this study, we define an unbiased retrieval to be one where the volume mixing ratio (VMR) of the species that have features in the wavelength region observed were constrained to values within 2-σ of the input values. We define a biased retrieval to be one where one of the molecular abundance is constrained outside 2-σ of the true value.

In the next subsections we describe our results for different instruments and different planet models. For each observing mode apart from Prism, we have presented the best fitting retrieved models and accompanying posterior distributions for the 60% case. For Prism we show the best fitting retrieved models and accompanying posterior distributions for the 20% and 80% case.

3.4.1 NIRSpec G140M

This is the most narrow wavelength region (0.97 – 1.84 μm) which is similar to the coverage of the Wide Field Camera 3 (WFC3) on the Hubble Space Telescope (1.1 – 1.7 μm): hence, the main absorber in this region is H_2O (See Fig. 3.4). This instrument would therefore be ideal if repeat studies of objects observed with WFC3 were required at a higher spectral resolution.

With regards to the ability to disentangle the contribution from two profiles, Table 3.2 shows it has the capability to do so with a planet with 60%, 40% and 20% of the flux contribution coming from the hot profile. For these simulations, the 1-D retrieval style produced biased chemistry results, whereas the 2-D and the dilution approaches did not. As the main absorber in this region is H_2O, an unbiased retrieval would be one where it was possible to constrain the abundance of this molecule and it was only possible to put an upper limit on the abundance of the other molecules. We present in Fig. 3.5 a comparison for the 60% scenario, where the 2-D and dilution retrievals were unbiased and the 1-D was biased.

$x = 80\%$						$x = 60\%$					
Observing Mode	2-D		Dilution		1-D	Observing Mode	2-D		Dilution		1-D
NIRSpec G140M	1.85σ	U	2.11σ	U	B	NIRSpec G140M	4.58σ	U	4.52σ	U	B
NIRSpec G235M	1.97σ	U	$< 1\sigma$	U	U	NIRSpec G235M	4.56σ	U	4.46σ	U	B
NIRSpec G395M	$< 1\sigma$	U	$< 1\sigma$	U	U	NIRSpec G395M	$< 1\sigma$	U	$< 1\sigma$	U	B
NIRSpec Prism	9.89σ	U	9.64σ	U	B	NIRSpec Prism	17.06σ	U	17.00σ	U	B
G235M + G395M	11.11σ	U	11.12σ	U	B	G235M + G395M	18.94σ	U	18.86σ	U	B
$x = 40\%$						$x = 20\%$					
Observing Mode	2-D		Dilution		1-D	Observing Mode	2-D		Dilution		1-D
NIRSpec G140M	4.12σ	U	4.18σ	U	B	NIRSpec G140M	4.53σ	U	4.61σ	U	B
NIRSpec G235M	4.42σ	U	4.32σ	U	B	NIRSpec G235M	5.18σ	B	5.23σ	B	B
NIRSpec G395M	$< 1\sigma$	B	$< 1\sigma$	B	B	NIRSpec G395M	2.77σ	U	2.36σ	U	B
NIRSpec Prism	19.16σ	U	18.9σ	U	B	NIRSpec Prism	16.15σ	U	16.03σ	U	B
G235M + G395M	21.31σ	U	21.31σ	U	B	G235M + G395M	18.57σ	U	18.64σ	U	B

Table 3.2: The results for all the test cases and instrument modes for the 3 retrieval styles used in this study. We calculated the Bayes factor of the 2-D and dilution style with respect to the 1-D approach (difference in the ln(Z) values) and then converted this to a significance estimate for the detection of more complex models in terms of standard deviation σ. We consider a strong detection if $>3.6\sigma$. The letters U and B indicate whether the retrieval was either biased or unbiased in terms of chemistry. All models had a reduced χ^2 of below 1.

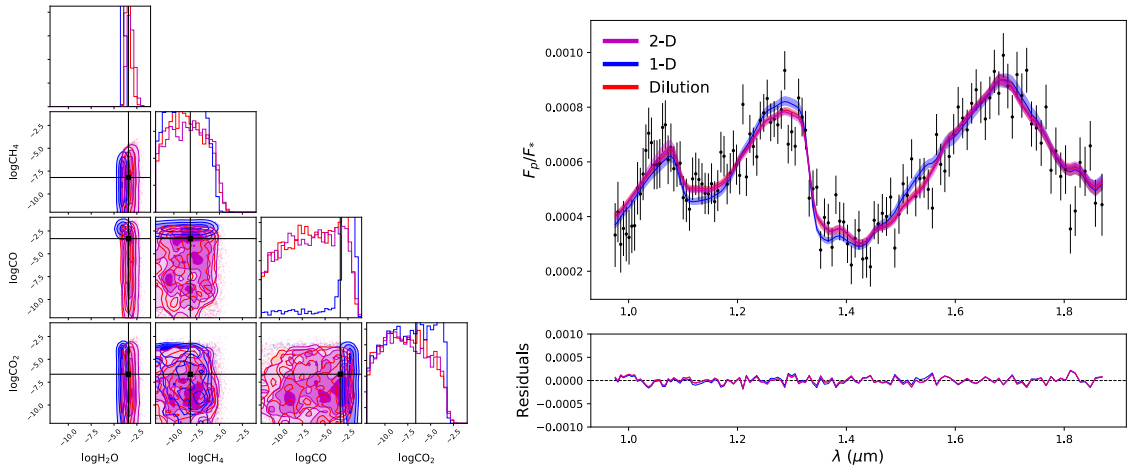


Figure 3.5: Best fitting models and accompanying posterior distributions for a planet scenario where the hot profile covers 60% of the observed disc as seen using NIRSpec G140M. We overplot the three retrieval styles: 2-D (magenta), 1-D (blue) and Dilution (red) and show in the residuals (model-data) that they present good fits to the data. The retrieved chemical abundances shown in the corner plot on the left are strongly biased compared to the true values (in black) for the 1-D retrieval case. This leads to a spurious detection of CO while no CO feature is seen in the original model (see the opacity comparison in Fig. 3.4).

In the $x = 80\%$ case, the H_2O abundance was constrained correctly for the 1-D retrieval. However, we also obtain a tight constraint on the CO_2 abundance at 3 orders of magnitude higher than the input value, corresponding to a spurious detection. For $x = 60\%$, 40% and 20% the H_2O abundance from the 1-D retrieval was accurately constrained to smaller values than the input and CO was constrained to an order of magnitude larger than the input. Again this would be a spurious detection of CO as the absorption due to H_2O is roughly 1 order of magnitude higher than CO in this region (see Fig. 3.4).

For an atmosphere that has a flux contribution that is 80% from the hotter profile, it is not possible to distinguish between 2-D or 1-D retrieval styles. This can be understood as the contribution from the colder profile, which already has muted spectral features, now has only a 20% contribution to the final spectrum, which are lost in the noise.

3.4.2 NIRSpec G235M

For all of the cases apart from $x = 20\%$ we see that only the 2-D or the dilution retrieval styles can correctly interpret the data. However, for the $x = 80\%$ case the

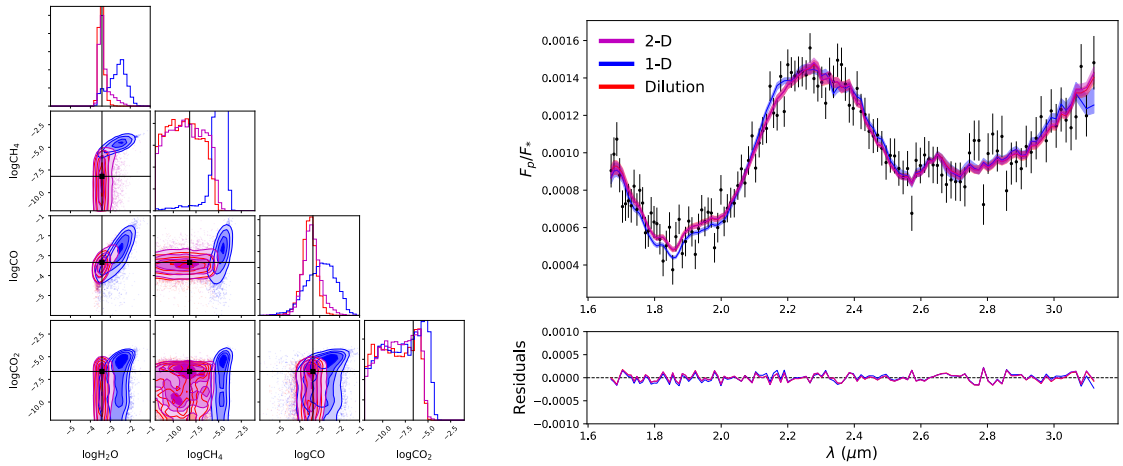


Figure 3.6: Best fitting retrievals and accompanying posterior distributions for a planet scenario of 60% flux applied to the hot profile as seen using NIRSpec G235M. We overplot the three retrieval styles: We overplot the three retrieval styles: 2-D (magenta), 1-D (blue) and Dilution (red) and show in the residuals (model-data) that they present good fits to the data. The true values are given by the solid black lines. When analysing the chemistry result presented in the triangle plot, we find a biasing of the result from the 1-D style, we see that the 1-D retrieval detects H_2O and CH_4 at values which are outside 2-σ from the input.

significance of using 2-D or the dilution over a 1-D style would be considered as a non-detection; the chemistry in the 1-D style was also not biased.

For all the unbiased scenarios, it was possible to constrain the abundance of H_2O and CO, but it was only possible to put upper limits on CH_4 and CO_2; this is to be expected as these molecules do not have strong features over this wavelength region (Fig. 3.4).

Table 3.2 shows that for the $x = 20\%$ case, all three retrieval styles produced biased results. We performed another retrieval with the same model, this time without any noise added (but keeping the same uncertainties) and again we get biased chemistry. However, the posteriors were multimodal and one mode sampled the true chemistry values. We attribute this to SNR of the observation being too low that the retrieval is not able to pick out discerning features. We present in Fig. 3.6 a comparison for the 60% scenario, where the 2-D and dilution retrievals were unbiased and the 1-D retrieval was biased.

3.4.3 NIRSpec G395M

For all of the planet cases, it is not possible to detect the 2 TP profiles. In all cases apart from $x = 40\%$, if 2 TP profiles were not used in the retrieval, then biases in the chemistry arose. We ran the 40% case with no noise model added and the results were then consistent with the other cases. Hence, the noise realisation used was causing the bias and not the SNR. The wavelength region covered by this instrument (2.87 – 5.10 μm) has been deemed to be a crucial grating as it covers the molecular features of CO and CO_2 (See Fig. 3.4) and the photometry points of the Spitzer Space Telescope. By performing tests on this grating it has become apparent that long wavelength coverage by itself is not what is crucial, but it is the specific wavelength region we cover. This is highlighted from Fig. 3.2, we can see that for the wavelengths covered by this grating, a SNR in the range of $\sim$10 would be needed to disentangle the 2-D effects in temperature, depending on the contrast of the profiles, hence we require shorter wavelengths to be able to disentangle the effects more efficiently.

We want to emphasise that, despite there being no evidence to use a 2-D retrieval or dilution retrieval, if one is not use, the chemistry will tend to be biased. Thus, caution needs to be taken when interpreting Bayesian evidence.

We present in Fig. 3.7 a comparison for the 60% scenario, where the 2-D and dilution retrievals were unbiased and the 1-D retrieval was biased.

3.4.4 NIRSpec Prism

With the largest wavelength coverage of the study, we find significant evidence for using a 2-D or a dilution retrieval for each of the planetary cases. We show in Fig. 3.8 the best fitting models for each of the retrieval cases for both $x = 80\%$ (top) and $x = 20\%$ (bottom), the residuals for the fits and also the posteriors. It can be seen that each case provides a fit that has a reduced χ^2 of below one; hence, without performing a model comparison, we could conclude that 1-D fit is good enough for the data. However, if we analyse the triangle plot, we see that for $x = 80\%$ the 1-D retrieval style produces a bias in the abundance and achieves a tight constraint on CH_4. For the $x = 20\%$ case, the 1-D retrieval style biases all of the chemistry apart from the H_2O content.

3.4.5 G235M + G395M

By combining the two gratings we achieve a similar level of σ confidence as using the Prism. What is interesting is that G395M alone was not able to disentangle the 2 TP

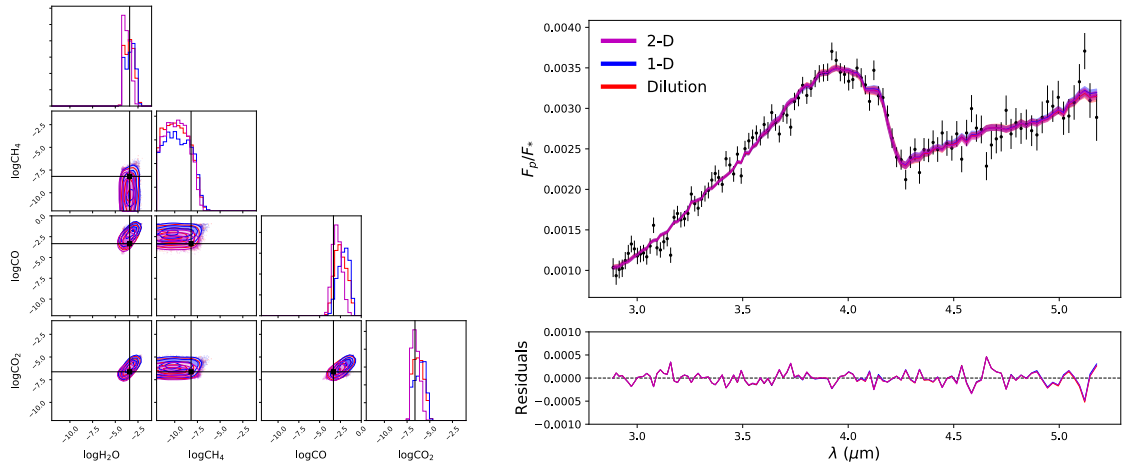


Figure 3.7: Best fitting retrievals and accompanying posterior distributions for a planet scenario of 60% flux applied to the hot profile as seen using NIRSpec G395M. We overplot the three retrieval styles: 2-D (magenta), 1-D (blue) and Dilution (red) and show in the residuals (model-data) that they present good fits to the data. The true values are given by the solid black lines. When analysing the chemistry result presented in the triangle plot, we find a biasing of the result from the 1-D style, we see that the 1-D retrieval detects CO at a value which is outside 2-σ from the input.

profiles. The addition of the G295M grating meant that the spectral coverage was over a range that has a shorter wavelength, which is shown in Fig. 3.2 to be a crucial spectral region that needs to be covered. The required SNR increases as we move to longer wavelengths. We present in Fig. 3.9 a comparison for the 60% scenario, where the 2-D and dilution retrievals were unbiased and the 1-D was biased.

3.4.6 2-D vs Dilution styles

From Table 3.2 it can be seen that the σ significance of the 2-D and dilution retrieval styles compared to the 1-D style are comparable. The difference is insignificant and can be considered as a non-detection. We can interpret this to mean that fitting for a second TP profile for a planet which we know to have one, is not favoured given the resolution of the data. Instead, a dilution factor applied to a 1-D retrieval style is all we can interpret. The dilution factor mimics the weight that is applied to the hotter profile; for example, the dilution factor obtained from NIRSpec Prism for $x =$ 0.8, 0.6, 0.4 and 0.2 are $s = 0.84$, 0.67, 0.51, and 0.32 respectively.

It can be seen from Table 3.2 that the performance of the chemistry retrieval for both styles is comparable. Out of the 20 retrievals performed with each technique,

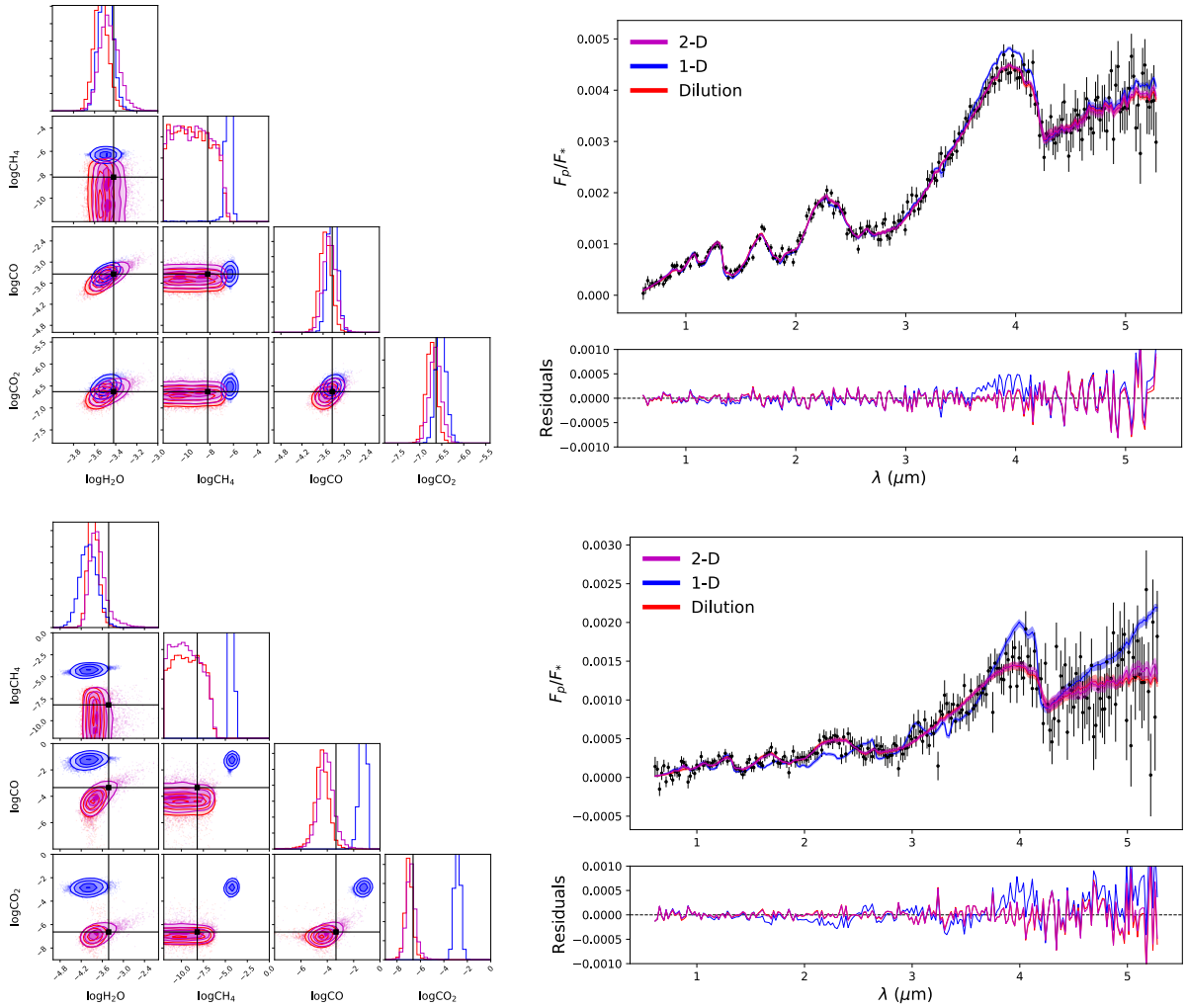


Figure 3.8: Best fitting retrievals and accompanying posterior distributions for the planet scenarios with weightings $x = 80\%$ (top) and $x = 20\%$ (bottom), as seen using NIRSpec Prism. We overplot the three retrieval styles: 2-D (magenta), 1-D (blue) and Dilution (red) and show in the residuals (model-data) that they present good fits to the data. The true values are given by the solid black lines. When analysing the chemistry result presented in the triangle plots, we find a biasing of the result. Note that performing a 1-D retrieval presents a good fit to the data, however the chemistry is biased, only by exploring 2-D models and comparing the Bayesian evidence would this have been apparent. Hence caution needs to be taken when performing retrievals on data that is not inherently 1-D.

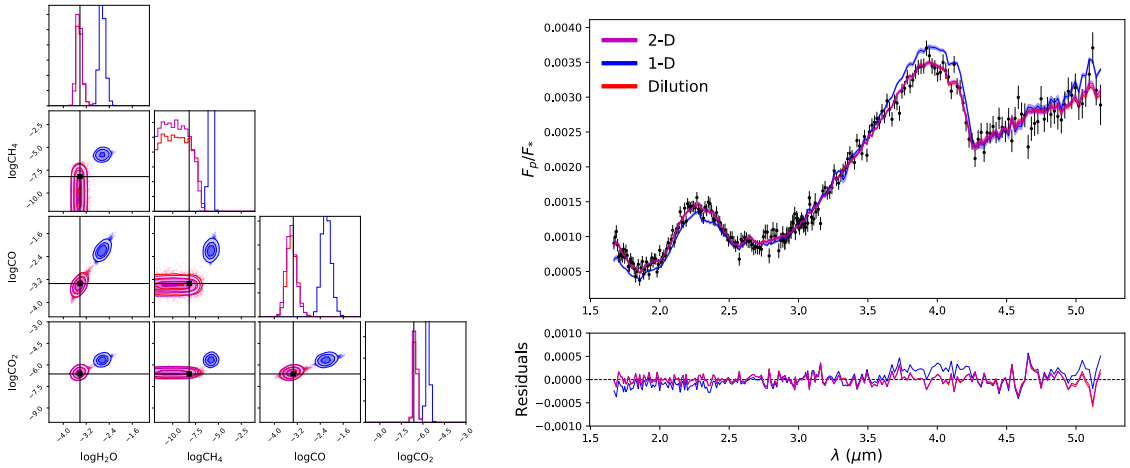


Figure 3.9: Best fitting retrievals and accompanying posterior distributions for a planet scenario of 60% flux applied to the hot profile as seen by combining NIRSpec G235M and G395M. We overplot the three retrieval styles: 2-D (magenta), 1-D (blue) and Dilution (red) and show in the residuals (model-data) that they present good fits to the data. The true values are given by the solid black lines. When analysing the chemistry result presented in the triangle plot, we find a biasing of the result from the 1-D style, we see that the 1-D retrieval detects H_2O, CH_4, CO and CO_2 at values which are outside 2-σ from the input.

both the 2-D and dilution retrievals produced biased chemistry in 2/20 of the cases. This is by far an improvement over the 1-D style which produced biased chemistry in 18/20 of the retrievals.

3.4.7 Origins of the chemistry bias

As we have seen in Section 3.4 and as discussed in Feng et al. (2016), in many cases performing a 1-D retrieval on a model created with 2 TP profiles can lead to biased retrieved abundances and even the spurious detection of chemical species. We now try to understand which mechanism can produce this bias.

To first order, we can assume that a planets atmosphere emits at a given wavelength with an amount of flux equivalent to the Planck function at the temperature corresponding to τ=2/3 at this wavelength. For a planet with a temperature that decreases with decreasing pressure (i.e., a non-inverted temperature-pressure profile), the thermal emission is larger if there are less absorbers in this region, and smaller if there are more absorbers in this region.

An emission spectrum at the resolution of JWST contains information at different scales. At small spectral scales, the molecular features corresponding to single

molecules are detected and their slope puts a strong constraint on the slope of thermal profile, with each band constraining the temperature gradient at a different layer. We see from our simulations the retrieval uses the numerous H_2O bands to determine the thermal structure of the atmosphere. However, as seen in the bottom panel of Fig. 3.1, the presence of an inhomogeneous atmosphere should affect the general slope of the spectrum (e.g. the mean slope between 1 and 5 microns, hence a larger spectral scale). Such a slope could be interpreted by the retrieval as a change in the slope of the temperature-pressure profile, however, because the temperature gradient is set in each layer by the small spectral scales (e.g., the slope of molecular features), the model cannot change the temperature-pressure profile to adjust the general slope of the spectrum. It must therefore rely on varying the opacities, hence the abundances.

Now let us imagine that we try to retrieve the abundances and temperature profile of a planet with a diluted hot spot, i.e., a hot temperature profile on a contained part of the visible hemisphere of the planet. At a given layer, the diluted blackbody would be given by the blue curve in Fig. 3.1. When trying to retrieve the planetary spectrum with a 1-D model, a typical blackbody would look like the red curve of Fig. 3.1. The ratio between the two, shown in the bottom panel of Fig. 3.1, have a slope: the 1-D emission is always smaller than the diluted 2-D emission at short wavelengths and larger at large wavelengths.

One could adjust this slope in two possible ways, the first is to vary the vertical temperature gradient, so that different layers are probed at different wavelengths. However, the temperature gradient is already determined by the small scale molecular spectral bands that are detected. The other way, is to change the levels that are probed, i.e. to change the opacities so that the long wavelengths probe cooler layers and the short wavelengths probe hotter layers. For a non-inverted temperature-pressure profile that means that the opacity should be increased at long wavelengths and decreased at short wavelengths. As seen in the left panel of Fig. 3.10, H_2O is dominating the diluted hot spot spectrum. Hence increasing the H_2O abundance cannot significantly change the large scale spectral slope of the opacities. As seen in the right panel of Fig. 3.10, to change the spectral slope of the opacities we can increase the abundances of species for which the opacity bands gets larger with increasing wavelengths, e.g., CH_4 and CO. The combination of CH_4 and CO opacity can mimic the small scale H_2O features while increasing the general spectral slope of the opacities. We note that NH_3, considered in Feng et al. (2016) but not in this study, could play a similar role as CH_4 and CO, giving even more opportunities to mimic the small scale signatures of H_2O while giving more liberty to adjust the large

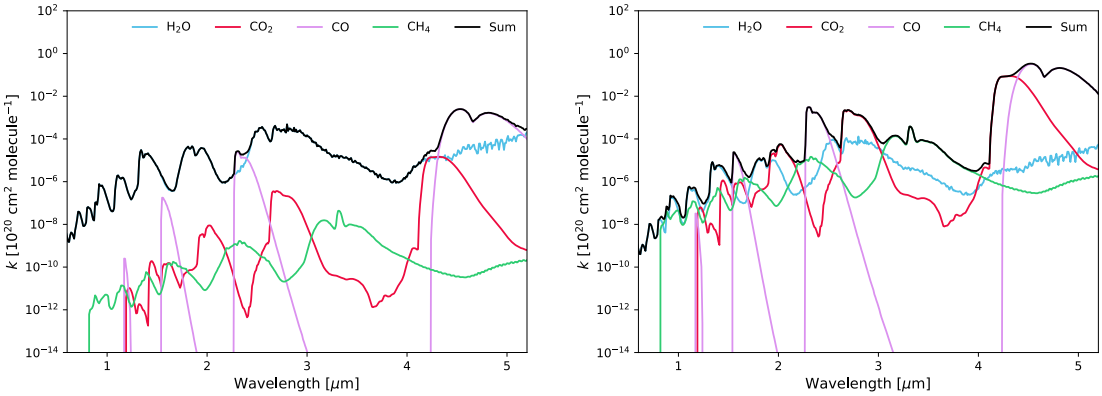


Figure 3.10: **Left:** Weighted-by-abundance absorption coefficients of the molecules from the best fit 2-D model for the 20% hot flux case shown in Fig. 3.8; we also present the sum of the absorption coefficients, which is representative of the absorption of the final best fitting spectrum. The sum is dominated by the water opacity at most wavelengths. **Right:** Weighted-by-abundance absorption coefficients of the molecules from the best fit 1-D model for the 20% hot flux case shown in Fig. 3.8; we also present the sum of the absorption coefficients, which is representative of the absorption of the final best fitting spectrum. We see that the 1-D retrieval requires an increase in the opacity of all the molecules apart from H_2O to fit to the observations. This is because varying H_2O would shift the total opacity up and down without changing the slope of the opacities at large spectral scales. Other molecules, such as CH_4 or CO have a larger variation between 1 and 5 microns and are used by the retrieval to increase the mean slope of the total atmospheric opacities.

scale spectral slope of the opacities. More generally, any additional molecule would give an additional leverage to adjust the spectral slope and compensate the lack of 2 TP profiles in the original fit. This would then lead to spurious molecule detection when using a model with 1 TP profile. Given that any additional molecule considered in a retrieval framework would increase the ability of the retrieval to compensate for the lack of inhomogeneities, this has the potential to lead to numerous spurious detection of molecules in JWST spectra. We therefore urge future modellers to carefully quantify the possible effects of temperature inhomogeneities in a planet atmosphere before claiming the detection of an unexpected molecule.

3.4.8 Wavelength dependent radius effect

Recent investigation into other biases that arise when studying emission spectra include the wavelength dependence of the planet radius (Gandhi & Madhusudhan, 2018; Fortney et al., 2019). Fortney et al. (2019) highlight that this effect is not an offset,

and can cause a planet-to-star flux ratio variation of 5% for a typical hot Jupiter. Our results would remain unchanged when modelling the wavelength dependent radius effect, this is because the biases we find arise from the gradient of the opacities observed over a large wavelength range (i.e., a large spectral scale), whereas the radius effect would have its largest effect on the smaller scales of the spectrum, particularly by changing the shape of each molecular absorption bands. We demonstrate this in Fig 3.11 by showing the ratio of the 2-D and 1-D best fitting models from the x = 80% G395M simulations which had unbiased chemistry results. We see that there do not appear to be many small scale fluctuations in the residuals (bottom panel of Fig. 3.11, compared to bottom panel of Fig. 2 from Fortney et al. (2019)) hence the wavelength dependent radius effect and bias due to 2-D structures are independent of one and other, and given good enough SNR, it should be possible to disentangle both of them.

We also would like to note that modelling the wavelength dependent radius effect in 1-D would probably lead to the over estimation of the effect for the dayside spectrum of a planet. The effect of the variation of the radius is proportional to the scale height at the limb and is therefore sensitive to the limb temperature. However, the spectrum is sensitive to the temperature of the planets dayside, which is usually hotter than the limb temperature. By assuming that the correction due to the radius effect must be done at the same temperature as the retrieved temperature from the spectrum, one would likely overestimate the importance of the radius effect. One possible way to model the radius effect would be to model it in a 2-D framework like the one this study presents. When analysing a dayside spectrum, the transit radius variation should be determined by the retrieved cold temperature. For phase curve observations, the viewing angle of the limb will vary depending on the phase of the observation, hence $\Delta R_p(\lambda) = |yR_p(T_{\rm hot}) + (y-1)R_p(T_{\rm cold})|$ where y would be a parameter which would represent the weighting of the limb seen by the observer.

3.5 Summary

In this Chapter we have shown the impact that an inhomogeneous temperature structure has on the observed emission spectrum of an exoplanet and how to mitigate the potential retrieval biases that arise from this. The study has not considered clouds, which is unrealistic for the atmosphere of an exoplanet. Hence, the next Chapter will explore the impact that scattering clouds have on the emission spectrum and how to best model the scattering properties of clouds with future space-based observations.

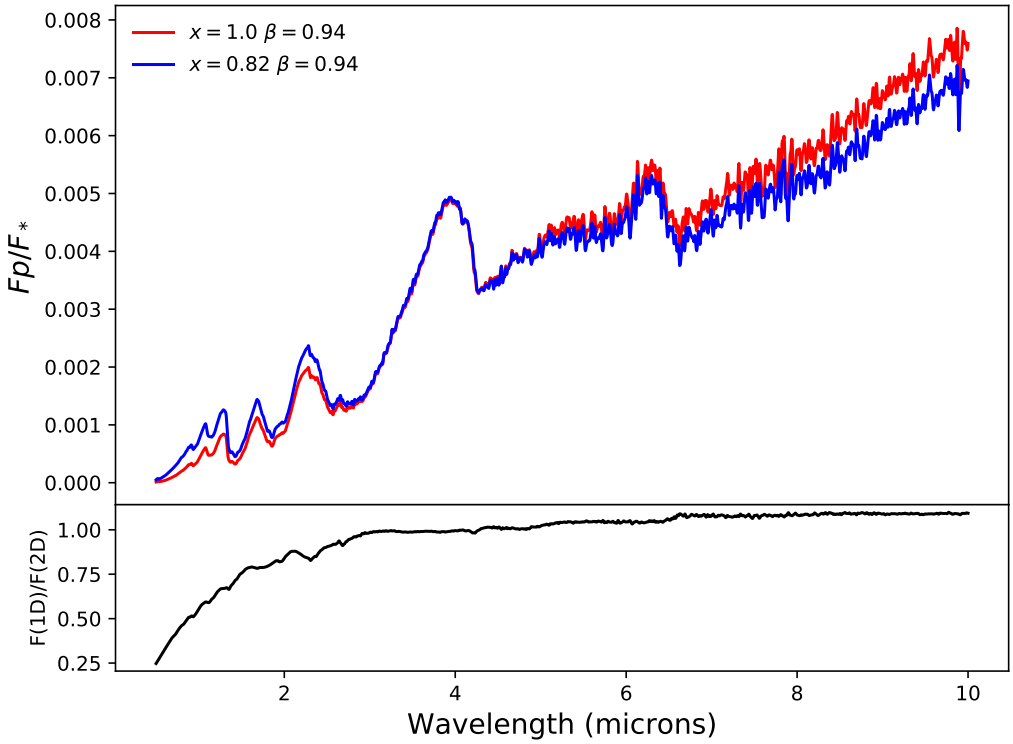


Figure 3.11: Top: Dilution and 1-D forward models generated from the best fitting parameters from the x = 80% case for the G395M observing mode. For the 1-D, $x = 1.0$ and $\beta = 0.94$ were retrieved and used for the forward model, for the dilution, which is analogous for 2-D, $x = 0.82$ and $\beta = 0.94$ were retrieved and used in the forward model. We chose to compare these due to their chemistry being unbiased in both scenarios, hence we are seeing the effect due to the thermal profiles. Bottom: The ratio of the two models. It can be seen that there is a larger gradient between the two at shorter wavelengths and this begins to plateau at longer wavelengths, this is similar to our analytical model in Fig 3.1.

Chapter 4

Thermal Scattering of Cloudy Exoplanets with JWST

The contents of this Chapter have been published in the Monthly Notices of the Royal Astronomical Society, the study can be found here Taylor et al. (2021). The CHIMERA model used in Section 4.4.7 was computed by Dr Michael Line of Arizona State University. The rest of the content in this Chapter are my contributions only. The work conducted in this Chapter was done during the COVID-19 pandemic.

4.1 Introduction

Clouds are present in all solar-system atmospheres and have been shown to be ubiquitous in exoplanet atmospheres (Iyer et al., 2016; Sing et al., 2016; Wakeford et al., 2019). They often hinder our ability to probe large regions of the atmosphere and are currently the main source of uncertainty when estimating the abundances of chemical species from exoplanet spectra (Deming et al., 2013), a situation that will still remain a challenge with the arrival of the James Webb Space Telescope (JWST) (Greene et al., 2016).

Currently, most studies addressing the role of clouds in atmospheric retrievals have tackled the case of transmission spectra (Lee et al., 2014; Barstow et al., 2017; Wakeford et al., 2017; Fisher & Heng, 2018; Tsiaras et al., 2018; Benneke et al., 2019; Carter et al., 2020). They have shown that different cloud parameterisations lead to similar retrieved abundances (Mai & Line, 2019; Barstow, 2020), but that neglecting the presence of clouds or neglecting their spatial variability could lead to incorrect retrieved abundances (Line & Parmentier, 2016; Welbanks & Madhusudhan, 2019; Pinhas et al., 2019). Another way to sense exoplanet atmospheres is through their emission spectrum. Phase curves can be used to measure the emission spectrum of the

planet at different phase angle, from the dayside to the nightside. Phase curves have been used to build temperature and cloud maps, showing the prevalence of clear and hot daysides (Kreidberg et al., 2014; Parmentier et al., 2016; Stevenson et al., 2017; Irwin et al., 2020) and cloudy and cold nightsides (Showman et al., 2009; Kataria et al., 2015; Parmentier et al., 2016; Helling et al., 2019; Beatty et al., 2019; Keating et al., 2019). Furthermore, the radiative effect of nightside clouds have been shown to complicate the link between observable quantities, such as the phase curve amplitude and fundamental atmospheric properties such as the heat redistribution efficiency (Parmentier et al., 2021).

Several cloud formation models of varying degrees of complexity have been used to investigate the formation of clouds and the diversity of their compositions in exoplanetary atmospheres, (e.g., Ackerman & Marley, 2001; Woitke & Helling, 2003; Sharp & Burrows, 2007; Helling et al., 2008; Ohno & Okuzumi, 2018; Powell et al., 2018; Samra et al., 2020). Most recently, Gao et al. (2020) use microphysical models to predict the most likely outcome of cloud formation in planetary atmospheres, concluding that for planets with a temperature greater than 800K the clouds would be silicate dominated. The impact of these various cloud compositions have been thoroughly explored in transmission (Wakeford & Sing, 2015; Pinhas & Madhusudhan, 2017; Kitzmann & Heng, 2018; Mai & Line, 2019), and it has been found that the variation in cloud optical properties leads to a wide range in spectral shapes.

We have already highlighted the important role that scattering plays in the atmospheres of planets in Chapter 2. In this Chapter we will apply the techniques outlined and developed in Chapter 2 and highlight the need for scattering to be invoked when studying the emission spectra of cloudy exoplanets.

4.2 How thermal scattering shapes the emission spectrum

4.2.1 Single Scattering Albedo and Emissivity

Cloud particles can interact with photons by either absorption or scattering. The Single-Scattering Albedo (SSA) is the probability that a photon colliding with a particle is scattered rather than absorbed, and can be defined as:

$$\omega_\lambda = \frac{Q_{\rm scat}(\lambda)}{Q_{\rm ext}(\lambda)} \tag{4.1}$$

where the total extinction cross-section, $Q_{\rm ext}$ is the sum of the scattering cross-section $Q_{\rm scat}$ and the absorption cross-section $Q_{\rm abs}$. Additionally, the ability of particles to re-emit light is determined by their emissivity ϵ_λ. In general, the source function in an atmosphere can be written as the combination of the scattering and the thermal emission terms:

$$S_\lambda = \omega_\lambda J_\lambda + \epsilon_\lambda B_\lambda. \tag{4.2}$$

where B_λ is the Planck function and J_λ is the first moment of the intensity. Kirchhoff's law states that at any particular wavelength, a particle is as good an emitter as it is an absorber. This means that the emissivity and the SSA must be linked by:

$$\epsilon_\lambda + \omega_\lambda = 1. \tag{4.3}$$

The source function therefore only depends on the atmospheric emissivity (or only on the SSA) and can be used to solve the radiative transfer equations for a plane-parallel atmosphere at local thermodynamic equilibrium. The full solution for non-isothermal atmospheres can be found in Rutten (2003). In the following sections we discuss some simplified cases in more detail.

4.2.2 Solution in the isothermal case

An isothermal atmosphere is often thought to emit like a blackbody. However, when thermal scattering is present the source function is no longer a Planck function and the planetary flux becomes:

$$F_p = \frac{2\pi}{\sqrt{3}} \frac{2\sqrt{\epsilon_\lambda}}{1+\sqrt{\epsilon_\lambda}} B_\lambda, \tag{4.4}$$

where the numerical prefactor depends on the choices of boundary conditions (see Parmentier & Guillot, 2014, Section 2.3.2 for a discussion). For unit emissivity, $\epsilon_\lambda = 1$, we recover the standard result, namely the planetary flux is equal to the Planck function. For smaller emissivity, however, the outgoing planetary flux is smaller than the blackbody cases, and vanishes for a purely scattering atmosphere.

When the emissivity is constant with wavelength, the resulting planetary spectrum is a diluted blackbody. This is demonstrated in Figure 4.1, where the purple curve corresponds to a model entirely dominated by a cloud opacity, with SSA $\omega = 0.9$, and hence emissivity $\epsilon = 0.1$.

In the general case, emissivity should depend on wavelength for two reasons. First, the cloud emissivity itself depends on wavelength (see Section 4.2.1 and Fig. 4.2).

Second, the local emissivity is the weighted sum of the cloud and gas emissivities. As we take the latter to be unity in this work, the local emissivity amounts to:

$$\epsilon_\lambda = \frac{\epsilon_{\rm cld}\,\kappa_{\rm cld} + \kappa_{\rm gas}}{\kappa_{\rm cld} + \kappa_{\rm gas}}, \tag{4.5}$$

where $\kappa_{\rm cld}$ and $\kappa_{\rm gas}$ are the cloud and gas opacities, respectively.

This equation shows that, for a constant cloud opacity and emissivity, the local emissivity is a monotonically decreasing function of the molecular opacity. The dilution factor before the Planck function in Equation 4.4 is then a monotonically-decreasing function of the molecular opacities. As a consequence, inside molecular absorption bands the emissivity will be high, the dilution factor will be small and the planetary flux will be large, whereas it is the opposite outside molecular bands. In summary, *an isothermal atmosphere with a cloud that has a constant opacity and constant emissivity will mimic molecular emission features.*

Figure 4.1 demonstrates this behaviour for an isothermal atmosphere with H_2O and CO in solar-composition proportions and a constant opacity, constant emissivity cloud. If the cloud opacity is much smaller than the gas opacity, the spectrum follows a Planck function as expected. As the cloud opacity increases, it becomes comparable to the gas opacities, and emission bands of H_2O and CO start to appear. For very large cloud opacity, the emissivity is entirely dominated by the cloud contribution and the spectrum reverts to that of a blackbody, albeit diluted by a constant factor.

4.2.3 Non-isothermal case

In the non-isothermal case the situation is more complex and the planetary flux takes the form:

$$F_p = \frac{2\pi}{\sqrt{3}} \left(\frac{2\sqrt{\epsilon_\lambda}}{1+\sqrt{\epsilon_\lambda}} \right) B_\lambda \left(\tau_\lambda = \frac{1}{\sqrt{3\epsilon_\lambda}} \right), \tag{4.6}$$

the derivation of which can be found in Appendix D. Scattering therefore affects the planetary flux in two ways. First, as for the isothermal case, it multiplies the planetary flux by a dilution factor, which is a monotonically decreasing function of the gaseous opacity. Second, it increases the effective depth of the photosphere by a factor $1/\sqrt{\epsilon_\lambda}$.

For an atmosphere with a temperature that increases with increasing altitude, the flux is generally smaller outside molecular bands. However, that is where the emissivity is low, hence the photosphere probes deeper, colder layers and the flux is reduced. Similarly, the dilution factor is small when the emissivity is low. Thus, for an atmosphere with a temperature inversion and emission features, both effects

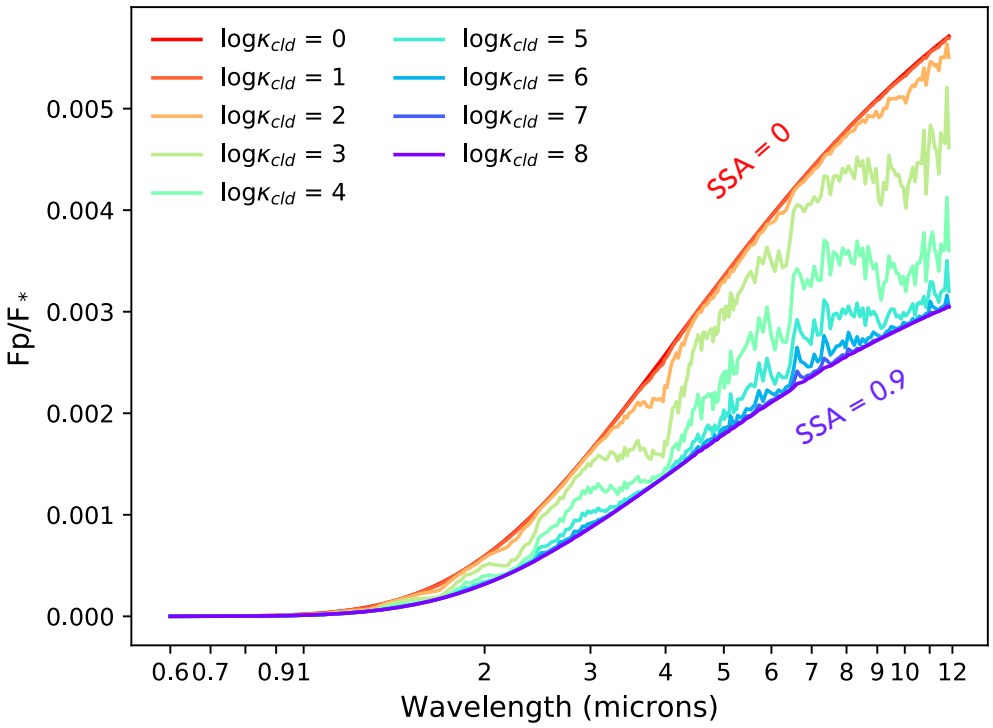


Figure 4.1: Model atmospheres varying from cloud free (SSA = 0, smooth red line) to completely dominated by the opacity of the cloud (SSA = 0.9, smooth purple line). The thinner lines containing features, which are due to H_2O in the atmosphere, correspond to isothermal atmospheres with a temperature of 1400 K and a cloud with a SSA of 0.9, whose opacity increases by an order of magnitude between each line, from red to purple. We transition from a molecule opacity dominated regime to a cloud opacity dominated regime. It can be seen that the opacity of the cloud results in different temperature layers being probed.

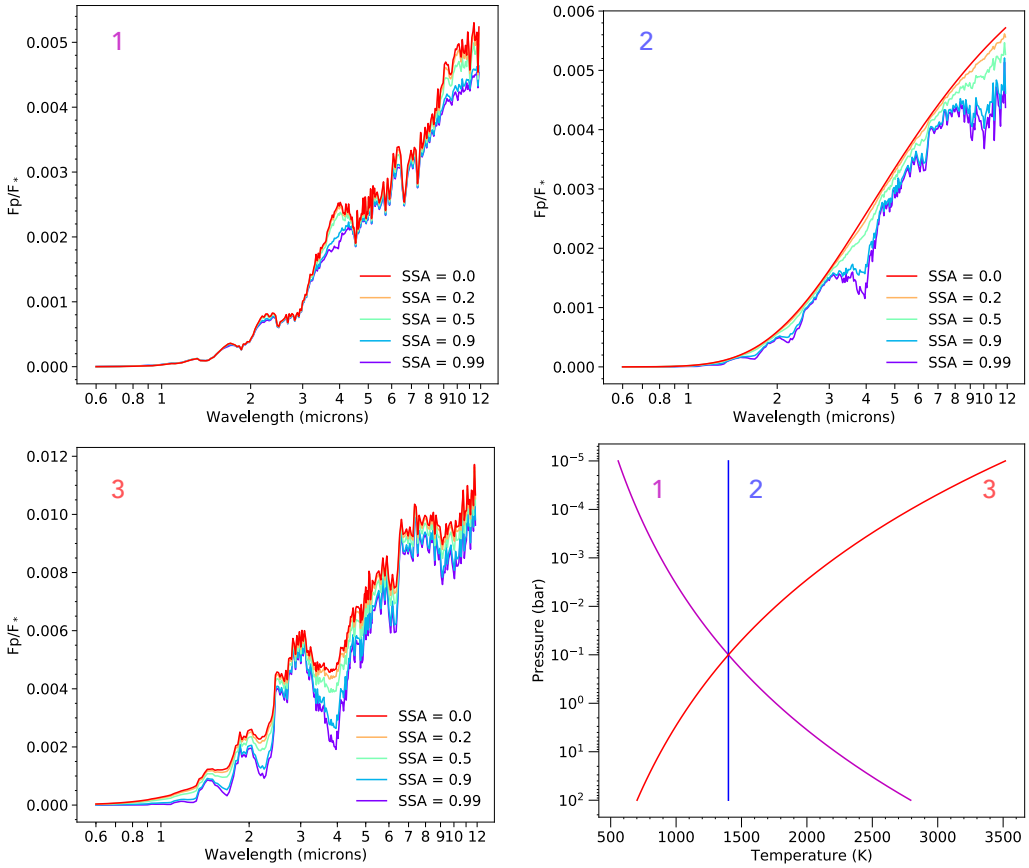


Figure 4.2: Impact of the SSA on the emission spectra for different TP profiles. The TP profiles corresponding to cases 1, 2 and 3 (top left, top right and bottom left plot, respectively) are shown in the bottom right plot. All models were generated using $\log(\kappa_{\rm cld}) = 3$ and with roughly solar H_2O and CO abundances. The non-isothermal TP profiles were generated using the 3-parameter model given by Equation 4.8, with $\alpha = 0.1$ and -0.1 for cases 1 and 3, respectively.

act jointly to reduce the planetary flux more strongly outside molecular bands than within them, hence increasing the relative contrast of the emission features.

For an atmosphere with a temperature that decreases with increasing altitude, the flux is generally larger outside molecular bands. However, that is a region where the emissivity is low, hence the photosphere probes deeper, hotter layers. We see an opposite effect with the dilution factor, as it is small when the emissivity is low. Therefore, for an atmosphere without a temperature inversion, the two effects of the scattering act in opposition. Whether the amplitude of molecular features is increased or decreased by scattering depends on the strength of the temperature gradient.

These different behaviours are shown in Figure 4.2. In the first panel, we show the case of a non-inverted atmosphere with a temperature gradient that is weak enough that the effect of the dilution factor dominates, and the amplitude of the molecular features decreases with increasing SSA. In the second panel, we show the case of an isothermal atmosphere, where emission features appear as the SSA increases. Finally, the third panel show that case of an inverted atmosphere, where the strength of the emission features increases with increasing SSA.

4.2.4 Expected degeneracies

We have shown that thermal scattering can change the shape of the spectral features in a planet atmosphere and even create emission features in the isothermal case. This will naturally lead to degeneracies between parameters: the spectra produced by atmospheres with scattering can look very much like those of atmospheres without scattering, but with a different set of physical properties.

The most obvious degeneracy arises when comparing the brightness temperature of a planet to the actual atmospheric temperature. Indeed, for an isothermal atmosphere with a constant, non-zero emissivity, Eq. (4.4) shows that the spectrum is a diluted blackbody. If we observe the atmosphere at long wavelengths, where the Planck function is linear in temperature, the brightness temperature measured in a given bandpass would become:

$$T_{\text{bright}} = \frac{2\sqrt{\epsilon}}{1+\sqrt{\epsilon}}\, T_{\text{atm}}. \tag{4.7}$$

For example, measuring the brightness temperature from the spectrum produced by an atmosphere with an emissivity of $\epsilon = 0.5$ would lead to a retrieved brightness temperature roughly 20% smaller than the actual atmospheric temperature. With an emissivity of $\epsilon = 0.1$, the brightness temperature is roughly 50% smaller than the true atmospheric temperature. This has far reaching implications for the night-side

of hot Jupiters, which have been shown to have cooler than expected temperatures (Beatty et al., 2019; Keating et al., 2019; Parmentier et al., 2021). These results could be explained by the presence of low emissivity, high single-scattering clouds, such as pure silicate clouds, which would lead to an apparent brightness temperature much smaller than the actual atmospheric temperature.

The second degeneracy arise from the dilution factor itself. In Chapter 3 we showed, in the context of a planet with an inhomogeneous thermal structure, that such a dilution factor can be mimicked by the spurious addition of molecules such as methane or ammonia. We therefore expect that the lack of scattering in retrieval models could lead to the spurious detection of molecules in cloudy atmospheres.

The third degeneracy we can expect is linked to the spectral variation of the atmospheric emissivity, which could affect either the inferred strength and sign of the temperature gradient, or the inferred molecular abundances. As highlighted in Fig. 4.2, the wavelength dependence of the emissivity generally reduces absorption features and increases emission features. This can be compensated in at least three different ways by a non-scattering retrieval. First, the thermal structure could be biased towards more positive temperature gradients. Second, the molecular abundances could be biased towards lower values for non-inverted atmospheres, so that the increased pressure broadening of the lines reduces the spectral features. Conversely, the abundances could be biased towards larger values for inverted atmospheres, so that the reduction of the pressure broadening of the lines enhances the size of the features. Finally, the change in the strength of molecular features could be compensated by the addition of a gradient in the molecular abundances. As shown by Parmentier et al. (2018), spectral features are increased if abundances increase with height and decreased if abundances decrease with height.

4.3 Results from constant cloud single-scattering albedo case

In this section we start with a simplistic model to understand the biases and degeneracies that thermal scattering can induce when extracting information from the emission spectra of exoplanets. For this we focus on the addition of a cloud with a constant opacity and constant emissivity. We first explore the simplest case of an isothermal atmosphere and then move to the non-isothermal case.

Parameter	Value
log(H_2O)	-3
log(CO)	-3
Temp [K]	1400
SSA	0.9
log(Opacity)	4

Table 4.1: Atmospheric and cloud properties used to create the isothermal model atmosphere.

4.3.1 Isothermal atmosphere

As seen in Section 4.2.2 we expect a cloud with a constant SSA in an isothermal solar-composition atmosphere to produce features that mimic emission that could be interpreted as the presence of an inverted thermal structure. We now want to quantify this in a retrieval framework.

We base our physical parameters of the system around the canonical exoplanet WASP-43b (Hellier et al., 2011) which have been refined by Gillon et al. (2012). We present the physical parameters and atmospheric parameters used in Table 4.1.

We used NEMESIS to generate a forward-modelled spectrum given the atmospheric parameters in Table 4.1 and then we used PandExo to generate the wavelength grid and the error bars for a single eclipse observation of WASP-43b. We consider the observing modes by NIRSpec Prism and MIRI LRS. We generate these observations considering a resolution of R = 50. We do not employ a random noise instance, but rather assume the data points at the exact model value in order to mitigate biases due to random noise instances (Feng et al., 2018; Mai & Line, 2019; Changeat et al., 2019)

In order to estimate which wavelengths are most sensitive to the effects of thermal scattering we focus on three different possible observing strategies:

1. A single eclipse observation using the NIRSpec Prism observing mode. Wavelength coverage: 0.6 - 5.3 μm

2. A single eclipse observation using the MIRI LRS observation mode. Wavelength coverage: 5.0 - 12.0 μm

3. Combining both NIRSpec Prism and MIRI LRS observations to investigate the complete wavelength coverage of JWST (0.6 - 12.0 μm).

We then perform retrievals of temperature and composition assuming the Parmentier & Guillot (2014) pressure-temperature profile from Chapter 2 and an atmosphere

with H_2O and CO gaseous absorption. Additionally, each of our three retrievals treats the clouds with an increasing complexity:

1. A cloud-free model, shown in blue in upcoming figures.
2. A pure absorbing cloud with constant opacity. This model is shown in red in upcoming figures.
3. A constant single-scattering albedo (SSA) cloud, with a constant emissivity and a constant opacity as described in Chapter 2. This model is shown in purple in upcoming figures.

In order to quantify the fit each model, we calculate the Bayesian evidence and convert the result to a sigma significance following the same method as Taylor et al. (2020). We compare the cloud free and the pure absorbing cloud model to the scattering cloud model, as the scattering cloud model is representative of the "true" model, and is hence the reference model for the model comparison analysis. In this comparison, the larger the value of the sigma significance, the more rejected the model is.

4.3.1.1 Observing scenario 1: NIRSpec Prism (0.6 - 5.3 μm)

The wavelengths observed with NIRSpec Prism cover a broad array of molecular species encompassing the dominant nitrogen, oxygen, and carbon reservoirs. Hence, NIRSpec is one of the instruments which will be highly used by the exoplanet community (Stevenson et al., 2016; Bean et al., 2018). The NIRSpec Prism is the lowest resolution instrument at around R $\sim$ 100, but with the broadest simultaneous wavelength coverage.

Fig 4.3 summarizes the retrieval results (fits, TP profile, and abundance constraints) under the 3 different retrieval model parameterisations. When calculating the sigma significance of excluding the cloud free and the pure absorbing cloud model we find that they are excluded at 8.3-σ and 4.8-σ respectively. Both the pure absorbing cloud and the cloud-free models require a temperature inversion to be able to fit to the data. However, when considering the scattering and retrieving for the SSA using the constant SSA cloud model, we are able to retrieve the correct profile, as we should given this retrieval forward model is identical to the input forward model.

Interestingly, the non-scattering cloud forward model is able to retrieve the CO and H_2O abundances with a similar precision and accuracy as the "true" scattering

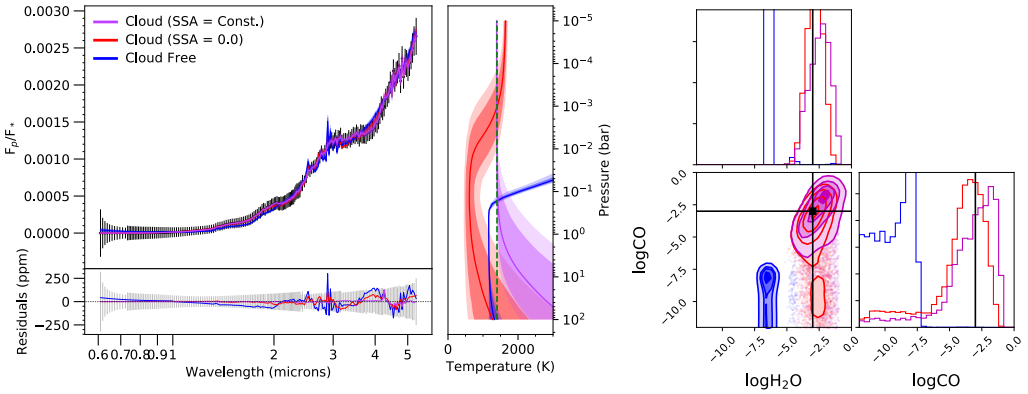


Figure 4.3: **Left**: Best-fitting spectra, temperature profiles and retrieved chemistry for three different retrieval models applied to synthetic NIRSpec Prism observations generated from planet with an isothermal TP profile and cloud opacity of 10^4. For each model we retrieve the TP structure with the analytical TP profile described in Chapter 2. In purple we retrieve on the synthetic data with the constant SSA cloud model. In red we fit using the pure absorbing cloud model. In blue we present the fit using a cloud-free model. We present the retrieved temperature-profiles with the true profile represented by a dashed green line. We present the residuals of the fit with grey shading indicating the error in ppm on the measurement. **Right**: we show the retrieved chemistry for each case with the true value in black.

forward model. Despite this success, however, we would incorrectly retrieve an inverted thermal profile. This suggests, in this scenario, that the scattering-TP profile degeneracy is largely decoupled from the abundances. The cloud-free model is not able to retrieve the correct abundances. In fact the retrieved abundances for H_2O and CO are so low that it appears the model is using the H_2-H_2 collision induced absorption to fit to the synthetic data.

4.3.1.2 Observing scenario 2: MIRI LRS (5.0 - 12.0 μm)

The 5.0 - 12.0 μm spectral range contains the strongest H_2O features and is crucial in studying the clouds in exoplanet atmospheres as it covers such cloud features as a silicate 'bump' (Cushing et al., 2006; Wakeford & Sing, 2015). Therefore, we have decided to explore its ability to recover the atmospheric properties from model observations generated using a simple scattering cloud. Fig 4.4 summarizes the retrieval constraints (similar to Fig 4.3) achieved under the MIRI observational setup.

The non-scattering cloud and cloud free retrievals produce nearly identical fits to the simulated data. This is due to the pure absorbing cloud model fitting for a near zero opacity which is consistent with a cloud-free atmosphere. When compared to

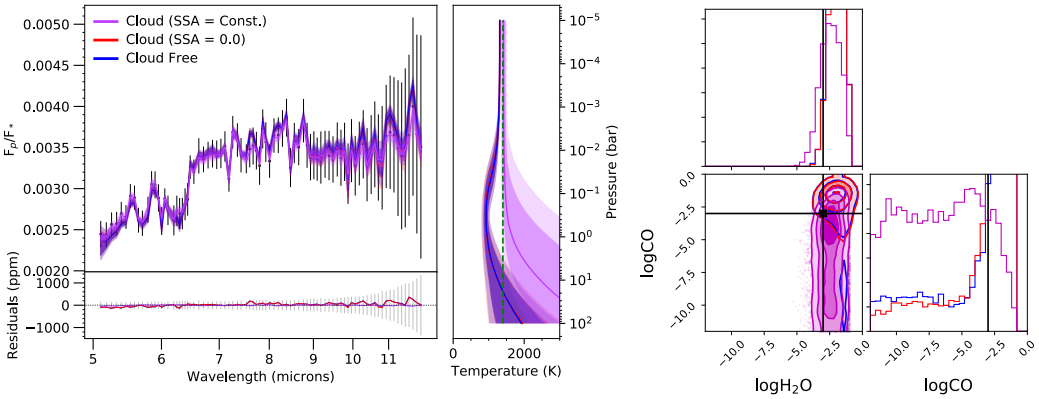


Figure 4.4: Same simulations as Figure 4.3, but for the MIRI LRS case.

the scattering cloud model, they can be excluded with a sigma significance of 4.3-σ and 4.4-σ respectively. Both these cases produce a slightly inverted TP profile. The residuals show that the fits are good given the error on the observations, and by not considering the effects of scattering, we could consider this atmosphere to be cloud-free with a temperature inversion. We also see that the retrieved TP profiles for these models are different from the TP profiles retrieved when studying the short wavelength case. The constant SSA cloud model fits best to the observations, with the TP profile converging to the true isothermal input.

The constant SSA model is able to retrieve the abundance of H_2O, but not CO. This makes sense as there are no CO features in this wavelength region. The cloud-free and pure absorbing cloud model slightly overestimates the abundance of H_2O and find an upper limit on the CO which is higher than the input.

4.3.1.3 Observing scenario 3: Full Wavelength Range

Figure 4.5 summarizes the retrieved constraints when combining the NIRSpec and MIRI modes for full 0.6 - 12 μm coverage.

By combining the observations the fit to the data is now worse for the cloud-free model, which now can be excluded with a sigma significance of 14.8-σ, with the most extreme deviations over the MIRI LRS wavelength coverage. It can be seen to have a slight temperature inversion and a retrieved H_2O abundance that is 2 orders of magnitude larger than the input value. We also find that we are unable to detect CO, despite it being present in the forward model.

We find that for the cloud-free models, the retrieved TP profiles for the short (0.5 - 5.3 μm) and long (5.0 - 12.0 μm) wavelength ranges are extremely different

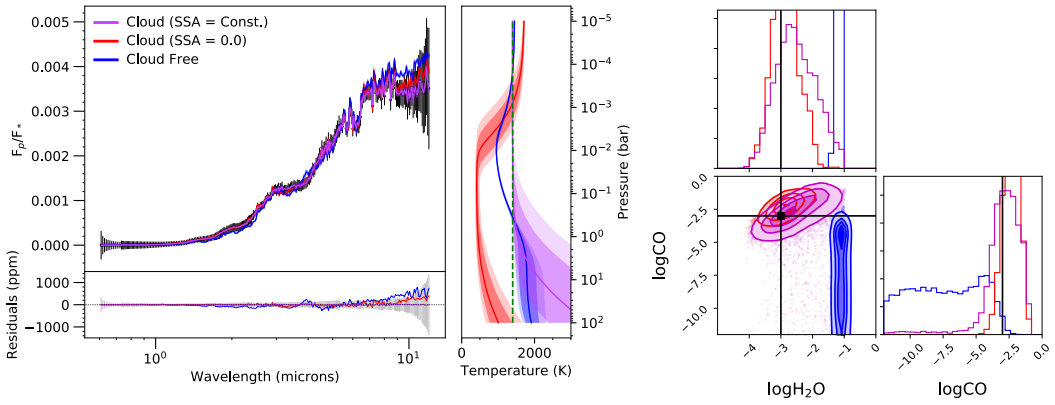


Figure 4.5: Same simulations as Figure 4.3, but for the combined NIRSpec Prism and MIRI LRS case. We present the full posterior distribution for the scattering cloud retrieval in Fig. 4.6.

and mutually exclusive. As a consequence, when fitting the full wavelength range the cloud-free model is unable to provide a good fit to the synthetically generated observed data.

Interestingly, similar to the NIRSpec only case, the non-scattering cloud model produces abundance constraints reasonably consistent with the truth (and the scattering cloud constraints). The non-scattering cloud model can be excluded with a sigma significance of 7.1-σ. Hence, if we did not compare with a scattering cloud model, we could be tricked into believing that this model is the best fitting model and also conclude that this planet has a temperature inversion, which is not, in fact, the case and not what we would conclude using the constant SSA model.

4.3.2 Non-isothermal atmosphere

We now explore the retrieval biases expected in a more realistic case of a planet with a temperature that decreases with decreasing pressure. The set up is the same as in Section 4.3.1, but this time the TP profile used is that described by three-parameter model which allows us to fit for the gradient of the temperature profile. It takes the form:

$$T = T_0 \times \left(\frac{P}{P_0}\right)^{\alpha} \tag{4.8}$$

where T_0, P_0 and α are free parameters. This parameterisation allows us to investigate how the gradient of the TP profile varies for the different model assumptions. For these simulations, the input parameters for the TP profile are $T_0 = 1400$ K, $P_0 = 0.1$

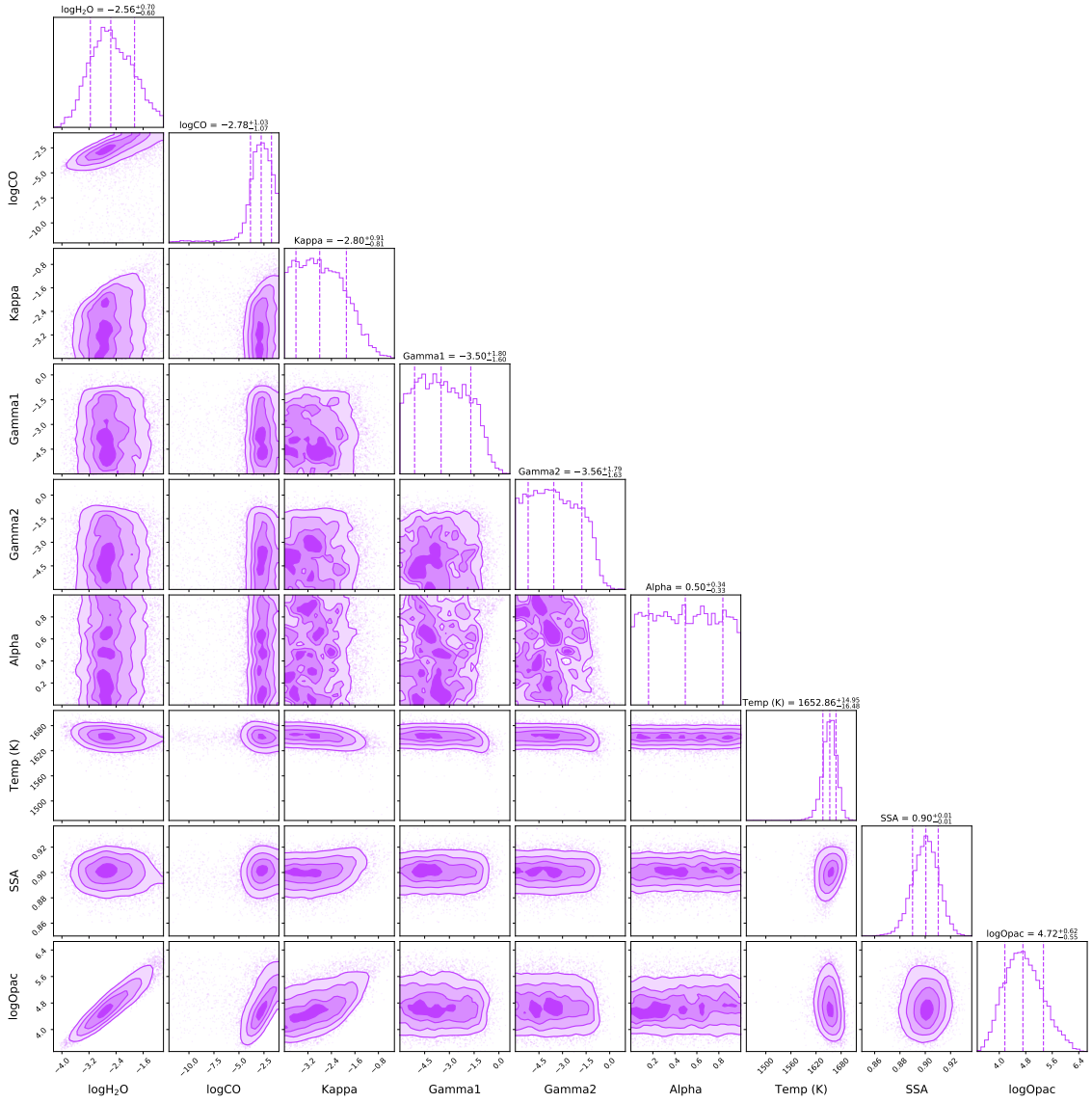


Figure 4.6: We present the corner plot showing the distribution of parameter space explored for the scattering retrieval presented in Fig. 4.5. For the 1-D histograms, we present the median result and the 1-σ values. This are represented by vertical dashed lines.

bars and $\alpha = 0.1$. We also reduced the $\log\kappa_{(\mathrm{cld})}$ to be 3. Similar to Section 4.3.1 we consider the same three observing cases.

4.3.2.1 Observing scenario 1: NIRSpec Prism

We first investigate the three retrieval forward models on the NIRSpec Prism data, just as in Section 4.3.1.1. Fig. 4.7 summarises these results.

The residuals show that both the constant SSA model and pure absorbing cloud model have similar fits to the data and that the cloud-free model deviates the most, with significant deviation at around 4 μm, the region where CO should be present. The cloud free and pure absorbing cloud models have an excluded sigma significance of 9.3-σ and 2.4-σ respectively, suggesting that the cloud free model is firmly rejected by the data but the non-scattering cloud model cannot be rejected. For the cloud-free model, we retrieve a steeper TP profile compared to the input, as anticipated from the analytic arguments. Only the constant SSA model can retrieve the input TP profile, with the pure absorbing cloud model retrieving a larger temperature at higher pressures.

All models are able to retrieve the correct composition to within 2-σ, with nearly consistent posteriors. The pure absorbing cloud model is the least accurate and has the widest posterior distribution.

4.3.2.2 Observing scenario 2: MIRI LRS

Fig 4.8 summarises the retrieval results under the MIRI LRS observational setup.

The residuals show that the cloud-free fit is not as good as either the pure absorbing cloud or SSA cloud models. The cloud free and pure absorbing cloud models are both considered consistent with the data (e.g., neither is rejected with cloud free at 2.3-σ, and purely absorbing at $<$ 1-σ). The same trends that can be seen in the NIRSpec Prism retrieved TP profiles are also seen with MIRI LRS. However, the profiles are less constrained.

The abundance posteriors are much wider than those obtained using NIRSpec Prism, with the cloud-free model not being able to retrieved the correct chemistry. The pure absorbing cloud and the constant SSA cloud model are able to retrieve the H_2O abundance with a posterior distribution which spans 5 orders of magnitude. This is a result of the large errors on the data, the data quality is not good enough to distinguish from the different models or say anything meaningful about the abundances.

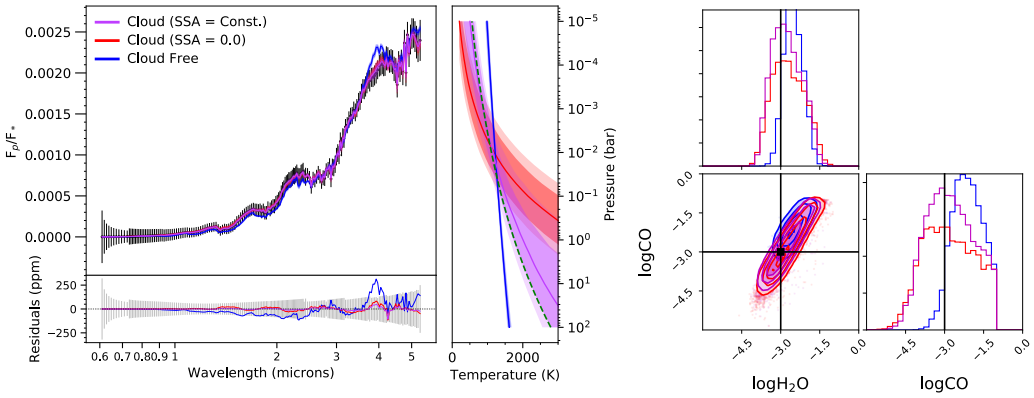


Figure 4.7: **Left:** Best-fitting spectra, temperature profiles and retrieved chemistry for three different retrieval models applied to synthetic NIRSpec Prism observations generated from a planet with three-parameter TP profile and cloud opacity of 10^3. In purple we retrieve on the synthetic data with the 3-parameter TP profile described by Equation 4.8 and model which allows for the single-scattering albedo to be fit as a constant value at all wavelengths. In red we retrieve using a similar model to the one shown in purple. However, we fix the single-scattering albedo to be zero, effectively removing the scattering component of the cloud and making the cloud grey. In blue we present a model that has no cloud. We present the retrieved temperature-profiles with the true profile represented by a dashed green line. We present the residuals of the fit with grey shading indicating the error in ppm on the measurement. **Right:** The posterior distributions of the retrieved chemistry with the colours corresponding to the models in the left plot. The black line represents the true value.

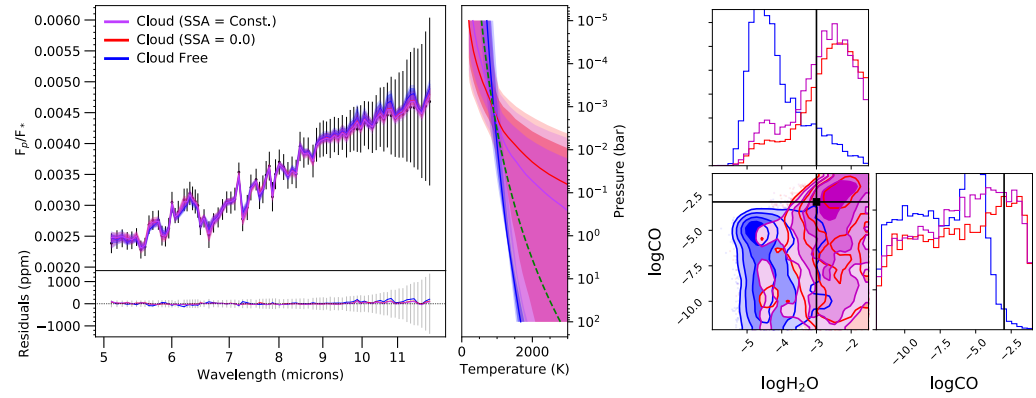


Figure 4.8: Same as Fig 4.7 but for the wavelength grid and errorbars of MIRI LRS.

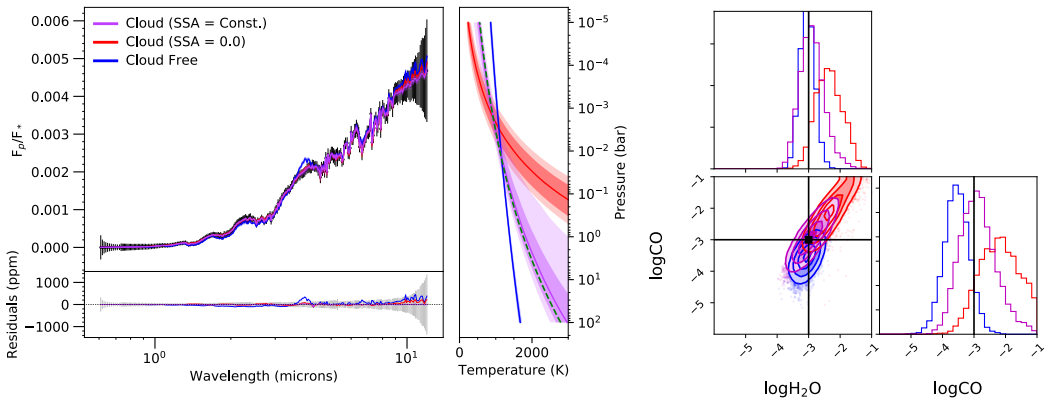


Figure 4.9: Same as Fig 4.7 but for the wavelength grid and errorbars of NIRSpec Prism and MIRI LRS.

4.3.2.3 Observing scenario 3: Full Wavelength Range

Fig 4.9 shows the constraints under the three retrieval forward model assumptions given the NIRSpec Prism + MIRI LRS "full" wavelength coverage observational scenario. The cloud free and pure absorbing cloud models have an excluded sigma significance of 11.2-σ and 3.1-σ respectively, this suggests that the cloud free model is firmly rejected, however the pure absorbing cloud is only marginally rejected, with the rejection limit being at 3-σ.

Interestingly, the cloud-free and the constant SSA cloud cases retrieve relatively similar H_2O abundances. However, the cloud-free model constrains a lower value of the CO abundance by around 2-σ compared to the input value. The pure absorbing cloud model constrains higher values of both the H_2O and CO abundances by around 3-σ compared to the input model value. This suggests that the broader wavelength coverage introduces more bias into the retrieved abundances when using the incorrect cloud model.

We find that the broad wavelength coverage results in higher precision constraints on the TP profile when using the correct forward model.

4.3.3 Inverted Thermal Profile

We now explore whether the biases exist if the when the atmosphere has an inverted thermal profile. We use the same setup from Section 4.3.2, this time setting the α parameter to be α = -0.1 when generating our synthetic spectra, this results in an atmosphere with a thermal structure where the temperature increases with height.

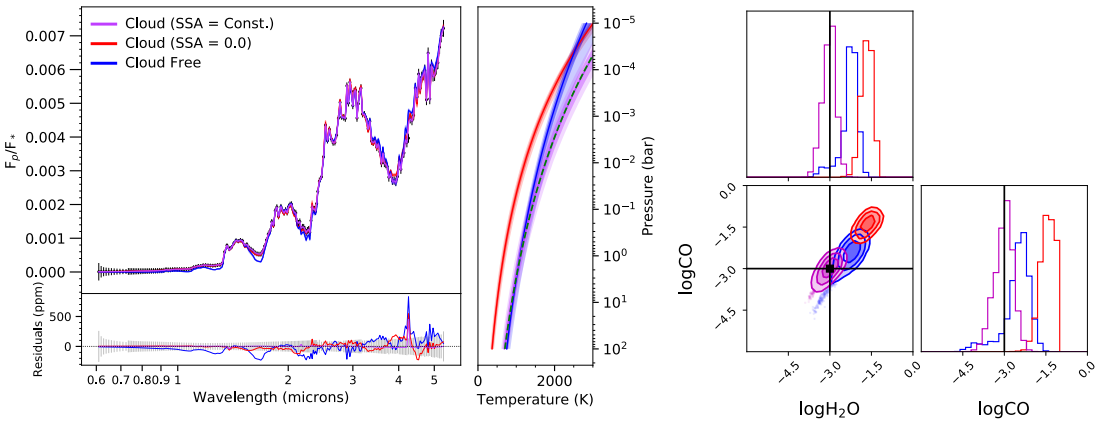


Figure 4.10: Same as Fig 4.7 but for the data generated using an inverted thermal profile.

We then re-retrieve on this spectrum using the three models described in Section 4.3.1.

For this case, we only consider the observing scenario of NIRSpec Prism. Fig. 4.10 summaries these results. It can be seen the fit of the scattering cloud and the pure grey cloud models are consistent within the error bars, however, the cloud free model shows the largest deviation. The cloud free and pure absorbing cloud models have an excluded sigma significance of 15.4-σ and 8.0-σ respectively, this suggests that both the cloud free and pure absorbing cloud models are firmly rejected. Only the scattering model is able to retrieve the input thermal structure and chemistry.

4.3.4 Summary

In summary, we demonstrated that failure to account for scattering can result in biased results in both the abundance inferences and in the derived thermal structures, though a greater bias appears in the temperature profiles. For the simple isothermal, scattering atmosphere, the interaction of the cloud opacity with the gas opacity can mimic emission features in a non-scattering atmosphere. A non-scattering retrieval forward model will interpret it as such, resulting in an inverted thermal profile. Despite the incorrectly retrieved TP profile, the non scattering cloud can accurately retrieve the abundances with a largely negligible bias.

We find for the more realistic case of an atmosphere with a decreasing with height TP profile and a scattering cloud, a non-scattering cloud retrieval model cannot be distinguished between the scattering model. We find that for each wavelength range that retrieved temperature gradient for the non-scattering cloud model is smaller

than the truth, with the opposite being true for the cloud free model. The retrieved abundances for the non-scattering cloud model are consistent with the scattering model for the individual instruments, however when combined for the "full" JWST range the abundances become biased by roughly 1 dex for both CO and H_2O in the non-scattering cloud case, and by roughly 1 dex for CO in the cloud free case.

4.4 Non-constant cloud single-scattering albedo

In the above proof of concept we have used a relatively simple setup, where we consider the single-scattering albedo and the opacity to be constant with wavelength. In this section we present some atmospheric simulations where we have used Mie theory to calculate the single-scattering albedo for some common cloud condensing species. We present the single-scattering albedo as a function of particle size and wavelength for these common cloud species in Figure 2.3, with their properties taken from Kitzmann & Heng (2018) apart from S_8, which was taken from Fuller, K. A. et al. in Palik (1998).

4.4.1 Realistic cloud single-scattering albedo and constant opacity

We explore whether our three-parameter cloud parameterisation scheme is able to account for the scattering properties of potential clouds without introducing bias in the retrieved abundances or thermal structure. This three-parameter cloud approach is independent of the choice of specific condensate, making it a favorable approach for a generalized cloudy retrieval. We consider four cloud condensing species: Al_2O_3, MnS, $MgSiO_3$ and Fe, chosen as these condensates span the range of relevant optical morphologies. For each of the forward models we consider the particle radius to be of 10 μm and to have a variance of 0.1 following a Gamma distribution as shown in Hansen & Travis (1974). We consider the condensates to be vertically mixed, with a fractional scale height of 1 and to have abundance of $\log(\kappa_{\rm cld}) = 4$. As in Section 4.3.1, we assume an isothermal atmosphere, resulting in "emission-like" features due to the scattering itself. Simulated observations are produced using the same procedure described in Section 4.3 for the "full" wavelength range.

We then retrieve on the four different condensate set ups with three different models. We use the analytical pressure-temperature profile from Chapter 2 and an atmosphere with H_2O and CO gaseous absorption with abundances the same as those

used in Section 4.3. Additionally, each of our three retrievals treats the clouds with an increasing complexity:

1. A cloud-free model, shown in blue in upcoming figures.
2. A pure absorbing cloud model, shown in red in upcoming figures.
3. A three-parameter cloud model. This is our novel cloud parameterisation, which is discussed in Chapter 2. This model is shown in purple in upcoming figures.

4.4.2 SSA Retrieval

For each of the cloud condensing species we retrieved the single- scattering albedo spectrum which we have shown in Fig 2.3 follows either a step-like shape or a straight line. We therefore have parameterised the shape of the SSA in attempts to retrieve it, as we described in Chapter 2. We plot the retrieved single-scattering albedo spectrum of the cloud in Figure 13. It can be seen that for all species it is possible to retrieve the overall shape of the actual single-scattering albedo spectrum of the cloud condensates. This is a very powerful result, given the approach was completely agnostic to the chemical and physical properties of the cloud, hence verifying that it works with a range of different shaped SSA spectra means that it is possible to learn about the clouds physical properties by comparing the retrieved SSA spectrum with various different cloud condensing species. We now go into further detail about each individual cloud case and nuances faced.

4.4.3 Al_2O_3

Al_2O_3 clouds have been predicted to form in the atmospheres of hot Jupiters over a range of temperatures (Parmentier et al., 2016; Gao et al., 2020). Out of all of the cloud condensing species investigated in this study, this one produces a spectrum that is relatively featureless compared to the others. We present the best-fitting spectra, temperature profiles and chemistry posteriors in Figure 4.11.

The residuals show that all models fit to the data well and do not deviate too much from each other. As predicted, the cloud- free model produces a temperature inversion in an attempt to fit to the spectral features and the three-parameter cloud model is able to retrieve the isothermal nature of the TP profile. The story is more complicated with the pure absorbing cloud model, which appears to retrieve the TP within 1-σ. However, it does not converge to an isothermal profile. In none of the cases can we retrieve the abundance of CO. This can be expected as the information for

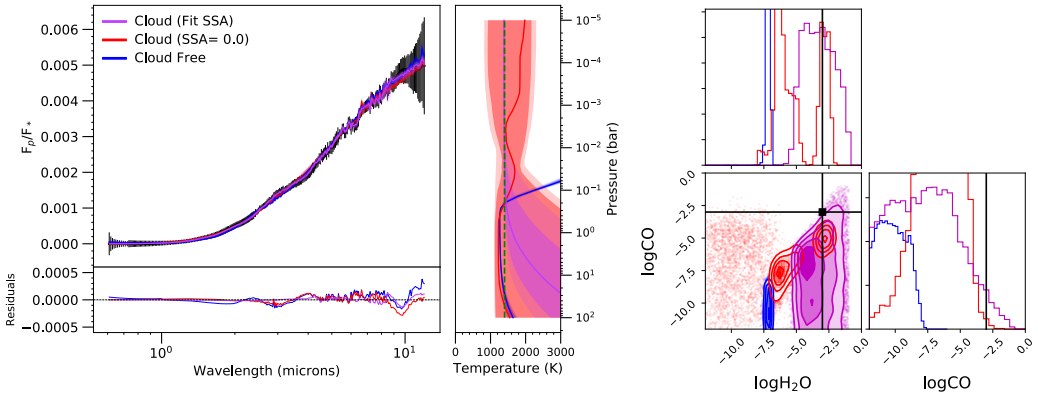


Figure 4.11: **Left:** The best-fitted spectra for the three models used on the data generated using a cloud made of Al_2O_3. For the cloud model we consider the particle radius to be of 10 μm and to have a variance of 0.1 following a Gamma distribution as shown in Hansen & Travis (1974). In purple we present the new three-parameter cloud, in red we present a cloud with single-scattering albedo of 0 (i.e., a grey cloud) and in blue we present the cloud-free model. Below we present the residuals of each fit. We present the accompanying temperature retrieval for each of the spectra, which have 1-σ and 2-σ shaded regions. The green dashed line is the input temperature-pressure profile. **Right:** We present the chemistry posterior for each case with the true value present in black.

CO would be at around 4 μm and we can see from the spectrum that this is relatively featureless. The H_2O abundance is recovered in the three-parameter cloud model, it is also recovered in the pure absorbing cloud model, however the posterior distribution is bimodal. Despite the good fit to the data, the cloud-free model cannot recover the H_2O abundance and underestimates it by four orders of magnitude. Given the low abundance retrieved in the cloud-free case, it can be understood that the retrieval is using the H_2-H_2 collision-induced absorption to fit to the spectrum, similar to that seen in Section 4.3.1.1.

4.4.4 MnS

MnS produces bright clouds, with a single-scattering albedo of nearly 1 across the JWST wavelength grid. However, it needs to be taken into account that the optical constants have not been measured in the infrared. Hence, we take the optical constants from Kitzmann & Heng (2018), which were calculated based on experimental data produced by Huffman & Wild (1967), and extrapolate using ZnS and Na_2S data trends for infrared wavelengths. This method was originally used by Morley et al.

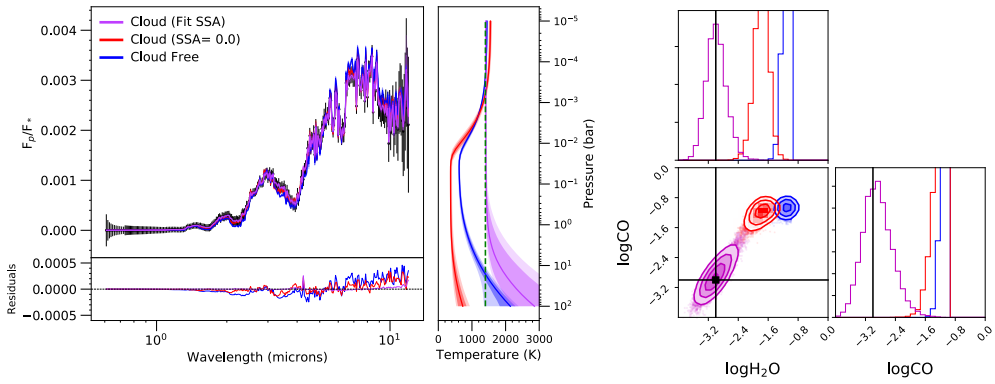


Figure 4.12: The same simulations as Figure 4.11, but now for the case of an MnS cloud.

(2012). We present the best-fitting spectra, temperature profiles and chemistry posteriors in Figure 4.12. The residuals of the fit show that the three-parameter cloud model fits the best. However, the cloud-free and pure absorbing cloud model still provide good fits to the data. It could be concluded that either of these fits were good if the true state of the atmosphere was unknown. It can be seen that the three-parameter cloud model is able to retrieve the TP profile. However, the other two models cannot, and in fact, they both produce a temperature inversion. Only the three-parameter cloud model can retrieve the 'true' abundances of H_2O and CO; the other two models both overestimate it in order to fit to the data.

4.4.5 $MgSiO_3$

Recently it has been found that the majority of hot exoplanets should be dominated by silicate clouds (Gao et al., 2020). We present in Figure 4.13 the best fitting spectra, TP profiles and the posterior distribution of the retrieved chemistry.

The single-scattering albedo of $MgSiO_3$ has a sharp transition at around 8 μm, which results in a kink in the spectrum. It can be seen that the cloud-free and pure absorbing cloud model cannot account for this, whereas the three-parameter cloud model can. Below 8 μm, the cloud-free and pure absorbing cloud models produce a near identical fit, which is evident by their complete overlap in the TP profile and chemistry. The cloud-free and pure absorbing cloud models are 3-σ different from the input for H_2O and are unconstrained for CO.

The three-parameter cloud model is able to retrieve the abundance of H_2O to within 1-σ and the abundance of CO to within 2-σ. This model is also able to

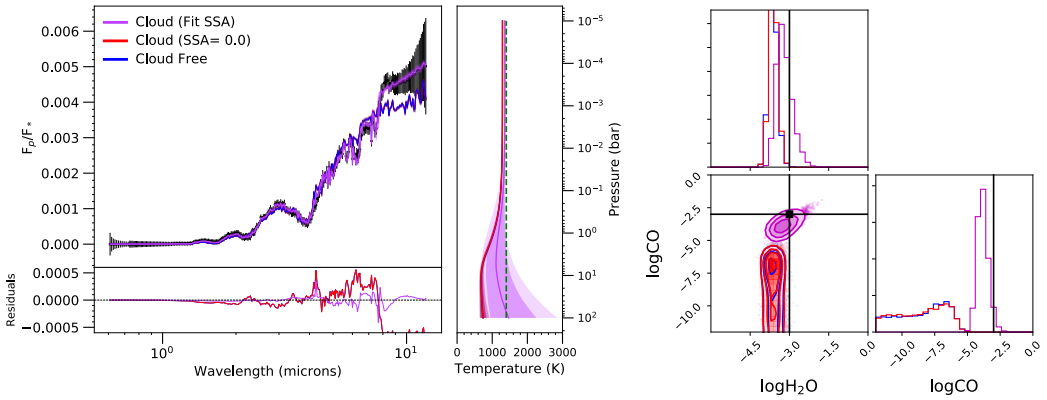


Figure 4.13: The same simulations as Figure 4.11, but for the $MgSiO_3$ cloud case.

retrieve the general shape of the SSA spectrum, which is shown in Figure 4.15. If the dominant cloud species in hot exoplanet atmospheres are silicate based, then the three-parameter cloud parameterisation will be able to retrieve the atmospheric properties accurately.

4.4.6 Fe

Fe clouds have been detected in hotter exoplanets such as WASP-76b (Ehrenreich et al., 2020). Our retrieval scenarios will be analogous to the ability to detect and study the chemistry of the nightside of these hot exoplanets, where Fe condenses. We present in Figure 4.14 the best fitting spectra, TP profiles and the posterior distribution of the retrieved chemistry.

It can be seen that the cloud-free model does not fit to the synthetic observations well. Consequently the TP profile exhibits an inversion and the chemistry is incorrect, with the H_2O being precisely retrieved to an abundance nearly two orders of magnitude higher than the input and the CO abundance being unconstrained. Both the pure absorbing cloud model and three-parameter cloud model fit well to the observations, but the pure absorbing cloud cannot fit to the features longward of 8 μm. Both models are able to retrieve the correct chemistry input, but the pure absorbing cloud model exhibits a TP inversion whereas the three-parameter cloud model converges to the correct TP profile. Similarly as we have seen before in this study, modelling with a pure absorbing cloud can provide a good fit and good retrieved chemistry, but infers an inverted TP profile.

In summary, all retrievals that do not take thermal scattering into account estimate biased abundances and converge towards the wrong thermal structure (see

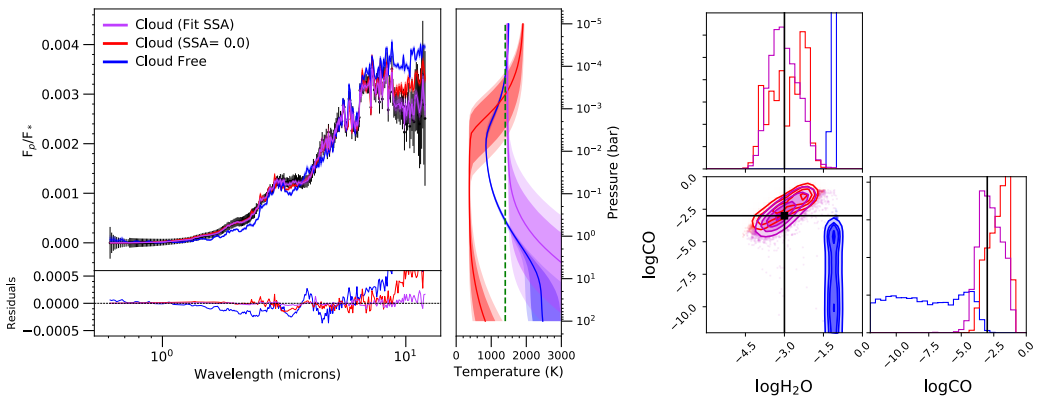


Figure 4.14: The same simulations as Figure 4.11, but for the Fe cloud case.

Fig. 4.11, 4.12, 4.13 and 4.14.) Importantly, as shown in Fig. 4.15, we are able to retrieve the overall wavelength dependent shape of the single-scattering albedo for all species considered. This is a very powerful result, given the approach was completely agnostic to the chemical and physical properties of the cloud, hence verifying that it works with a range of different shaped SSA spectra means that it is possible to learn about the clouds physical properties, this can be done by comparing the retrieved SSA spectrum with various different cloud condensing species.

4.4.7 Realistic cloud single-scattering albedo spectrum and varying opacity

We now investigate how the three-parameter cloud model would perform when retrieving on a spectrum that has a more physically motivated cloud. For this we use the CHIMERA (Line et al., 2013) retrieval tool[1] which employs the Ackerman & Marley (2001) cloud model to produce realistic vertical droplet profiles over a broad range of droplet sizes (for a specific condensate), given a sedimentation efficiency (f_{sed}), eddy diffusivity (K_{zz}, simplistically assumed to be 10^8 cm^2/s), cloud base pressure, and the condensate mixing ratio at the cloud base (see Mai & Line (2019) for implementation details). Here we assume enstatite ($MgSiO_3$) physical/optical properties, given a condensate mixing ratio of $10^{-5.5}$ at the cloud base (200 mbar). Along with these cloud properties, we include gaseous opacity due to H_2O (4×10^{-4}), CO (2×10^{-4}), and H_2-H_2/He (0.86/0.137) CIA, and employ the analytical TP profile as discussed in Chapter 2 (T_{irr} = 1400, $\log\kappa_{ir}$ = -1.5, $\log\gamma_1$ = -0.7, T_{int} = 300K), under WASP-43b system properties. Molecular (and continuum/condensate) opacities are

[1] https://github.com/mrline/CHIMERA

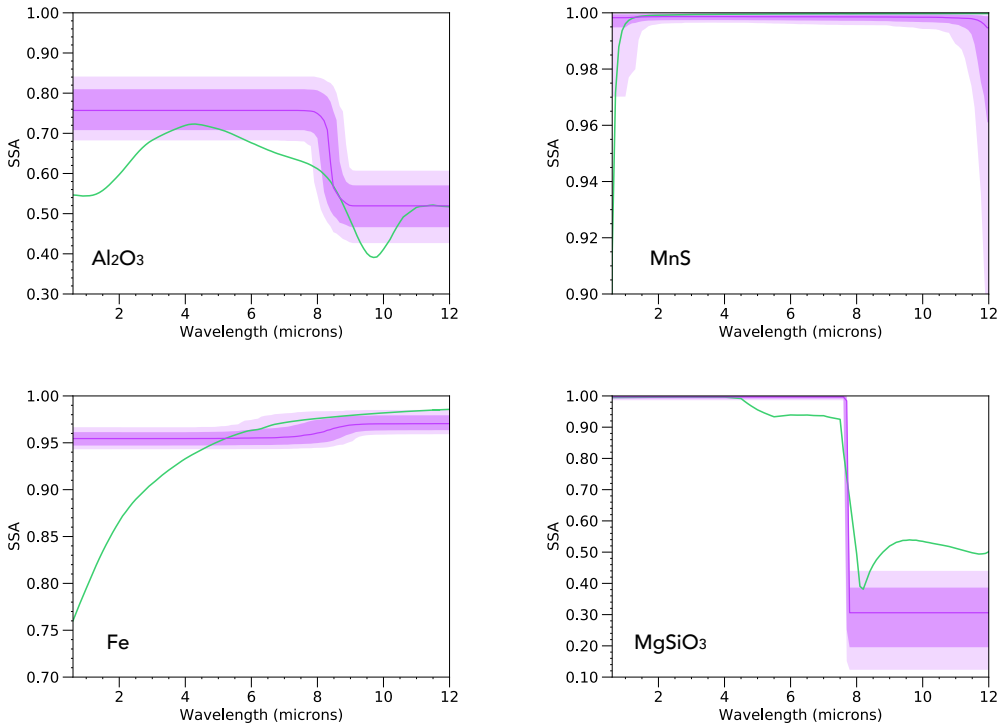


Figure 4.15: The best-fitting retrieved single-scattering albedo (SSA) spectrum using the three-parameter cloud parameterisation. In purple we present the retrieved SSA spectra with 1- and 2-sigma envelopes. In green we present the SSA spectrum for each of the cloud condensing species, which are labelled in each of the plots; each species has been modelled with a particle size of 10 μm.

treated within the correlated-K resort-rebin framework (e.g., Mollière et al. (2015); Amundsen et al. (2017)). The Toon et al. (1989) two stream source function technique is used to solve for the fluxes (both up, down, stellar, and planetary) in these non-homogeneous multiple scattering atmospheres (a different approach to the multiple scattering problem than NEMESIS). While stellar reflected flux is a natural consequence of multiple-scattering atmospheres, here, we explore only the retrieval biases arising from the thermal component. We assume an extended cloud scenario for these tests ($f_{sed} = 0.1$, a nearly constant with altitude condensate profile).

We then used this forward model in PandExo to generate the observations for one eclipse observation of WASP-43b using NIRSpec Prism and MIRI LRS configurations at a resolution of R = 50. These simulations are similar to the ones calculated in Section 4.3. However, for this scenario we have kept the random noise instance to emulate a "real observation". We then retrieve on these data with the same three models described in Section 4.4.1.

To validate CHIMERA and NEMESIS for this work we performed a benchmark test, which is described in Appendix A. We used NEMESIS to retrieve on a cloud free model generated by CHIMERA with an error envelope of 60ppm. We find consistent results as shown in Fig. A.2 and A.3. Therefore the differences that are found due to the 3 parameter SSA modelling approach and the Ackerman & Marley cloud parameterisation are not due to the choice of radiative transfer assumptions in the respective codes.

4.4.7.1 Retrieval results

Figure 4.17 shows the best fitting models, their temperature profiles and abundances. The purely absorbing cloud and cloud free retrievals produce nearly identical fits to the simulated data. This is due to the pure absorbing cloud model fitting for a near zero opacity which is consistent with a cloud-free atmosphere. Both models fit for an inverted TP profile and retrieve abundances that are lower than the input model.

The three point cloud model is able to retrieve the correct H_2O abundance, however the CO abundance is nearly 2 order of magnitudes larger than the input. This model is able to retrieve a temperature profile that is decreasing with height. Despite the CO abundance, the retrieved results are more consistent with the input, therefore, the scattering cloud model is an improvement compared to the non scattering and cloud free models. We find that the retrieve SSA spectrum is representative of the SSA spectra of the photosphere of the forward modelled atmosphere which is around 10^{-2} to 10^{-3} (Fig. 4.16). However, the change of SSA with altitude, related to a

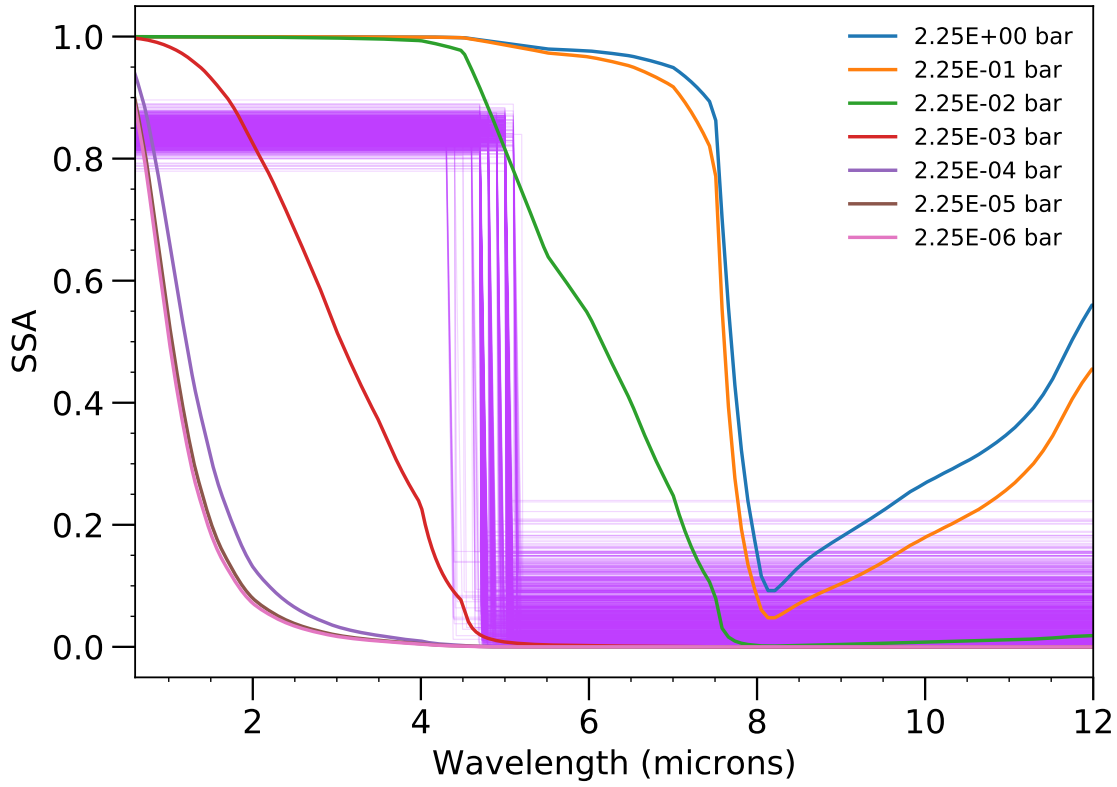


Figure 4.16: We present the retrieved single-scattering albedo for the 3-parameter model from Fig. 4.17. The purple lines shows 1000 models drawn from the posterior distribution. We over plot the forward model single-scattering albedo generated using CHIMERA for different pressure levels. We note that the photosphere is between 10^{-2} and 10^{-3} bar, our retrieved single-scattering albedo spectrum is between the forward model single-scattering albedo spectra at these values.

change of particle size with altitude cannot be taken into account in our modelling framework and is probably leading to the bias in the retrieved abundances. We compute the Bayesian evidence to conclude which model is most supported by the data. We find that the data supports the 3-parameter scattering model over the purely absorbing and cloud free models by 8.25-σ and 8.00-σ respectfully.

We note that the model used here to test our framework is probably a bit pessimistic. The nightside of the real WASP-43b planet is likely to have a larger thermal gradient than predicted by the semi-grey thermal profile, which should lead to larger spectral features than the ones predicted here.

We note that our 3 parameter SSA method offers an improvement over cloud free or purely absorbing clouds, but does not offer a perfect solution. This is likely due to the additional simplifications in our cloud model, such as the constant-with-altitude

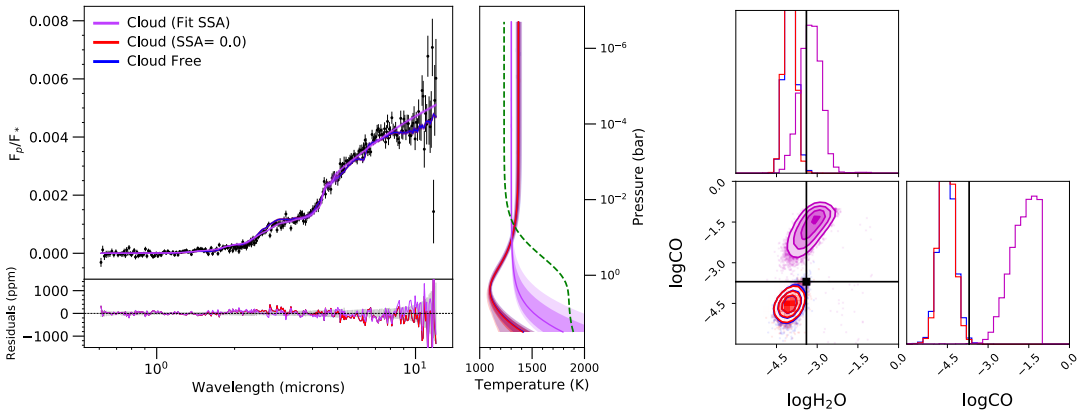


Figure 4.17: The retrieved results from the data generated using CHIMERA, the error bars and noise were generated using PandExo. Left: The best fitting spectra and retrieved temperature profiles. In purple we present the 3-parameter cloud model. In red we present the purely absorbing cloud model. In blue we present the cloud free model. In green we present the input temperature profile. Right: The retrieved chemical abundances, with the true value represented by a black line.

mixing and different choice of particle size distribution. Future work will focus on implementing more realistic vertical cloud droplet profiles. A hybrid approach between an Ackerman & Marley type vertical droplet parameterisation and an "N-parameter" SSA retrieval may provide a better representation of "realistic" clouds. We also do not consider the influence of inhomogeneities (e.g., "holes" or "patchy clouds") which could further complicate thermal emission inferences.

Chapter 5

Conclusions and Future Direction

In this section we summarise the conclusions of this thesis and discuss the future direction of this research. We recommend how to analyse upcoming Early Release Science and Guaranteed Time Observations based on the results of this thesis.

5.1 Conclusions

In this thesis we have demonstrated that complex models are required to interpret the next generation of space-based observations of exoplanet atmospheres. The contents of this thesis have focused on the emission spectra of exoplanet atmospheres, a powerful technique to study the chemical composition, spatial structure and cloud composition of these alien worlds.

In Chapter 2 we upgraded the NEMESIS code to be able to study the atmospheres of ultra hot Jupiters by implementing H^- opacities, which is a strong opacity source for these planets. We implemented a flexible temperature parameterisation that is capable of modelling temperature inversions. We upgraded the code to retrieve conditions on the dayside and nightside of exoplanets simultaneously and applied this technique in Chapter 3. Finally, we upgraded the code to retrieve the single-scattering albedo spectrum of a cloud present in an exoplanet atmosphere and demonstrate the impact of this in Chapter 4.

In Chapter 3 we investigated how an inhomogeneous horizontal temperature structure affects the way we perform emission retrievals. We aimed to understand the origins of the biases and how to mitigate them with JWST's NIRSpec instrument. We summarise the conclusions as follows:

1. We first derive an analytical criterion which can be used to find the signal-to-noise ratio required to disentangle inhomogeneous temperature structures. We

find that the signal-to-noise ratio needed increases for longer wavelengths; this is demonstrated in Fig. 3.2. This is because the longer the wavelength, the closer the emission spectra from the hot and cold parts of the atmosphere are to each other.

2. We then build planetary scenarios with varying hot and cold flux contributions. We generate synthetic observations for the NIRSpec observing modes and perform atmospheric retrievals on them. We find that performing a homogeneous retrieval will often result in biased chemical abundances, as shown from Table 3.2.

3. We show that a novel method of applying a dilution factor to a 1-D model can provide a similar retrieval capability as using the 2-D technique for cases where the hot-spot is significantly hotter than the surrounding atmosphere, suggesting that it might be an ideal technique for studying the chemistry of the atmosphere while saving on computation time. This is because it has the capability to perform the same as either a 1-D retrieval (if the dilution = 1) or a 2-D retrieval (if dilution $\neq$ 1) without facing biases in the chemistry.

4. Due to the large amount of dedicated time needed to perform phase curve observations, it is prudent to know which instruments are necessary to study the 2-D structure in more detail. We find that with a large enough spectral coverage we can break the correlation between the amount of flux output and the temperature for all of the planetary cases explored in this study (i.e., using Prism or combining G235M and G395M). Crucially, we show that the shorter the wavelength observed the better the detection of 2-D effects. We find that, despite G395M being the grating with the largest spectral coverage, there was no evidence to support using a 2-D or dilution retrieval over a 1-D style, but if these retrieval styles were not used, then biased results were produced. This reiterates that not only do we need a large wavelength coverage, but this coverage needs to sample shorter wavelengths. As Ariel (Tinetti et al., 2018) has a large wavelength coverage of 0.5 - 7.8 μm, it is ideal for detecting and quantifying inhomogeneities.

5. Shorter spectral coverage can also break the degeneracy, such as using G140M (sampling before the peak of the blackbody function), although with smaller significance and only if the hot profile contributes 60% or less to the final spectrum. This is something that would not be known for the dayside of a planet

unless performing *a priori* studies with GCM models. It would, however, be known for tidally-locked planets that are observed at various points in its phase around the star.

6. Finally, we explain the origins of the biases that we face when performing 1-D retrievals on a planetary system that has an inhomogeneous temperature structure. A 1-D model matching an emission spectrum from an inhomogeneous planet underestimates the spectrum at short wavelength and overestimate it at long wavelengths. As a consequence, the 1-D model requires larger opacities at longer wavelengths and smaller opacities at shorter wavelengths. In other words, the mean slope of the opacity vs. wavelength needs to be larger in the 1-D model than in the original spectrum. When H_2O dominates the original spectrum, this naturally leads to an increase in the abundance of molecules that have an opacity that increases more sharply with wavelength than H_2O, e.g., CH_4 or CO. Importantly, the larger the number of molecules considered, the easier it is for the 1-D retrieval to find a way to compensate for its lack of inhomogeneities. We therefore recommend that future works should consider the possibility of temperature inhomogeneities when searching for new molecules in JWST data sets in order to ensure that these detections are not spurious.

In Chapter 4 we have explored the impact that a scattering cloud has on the interpretation of an emission spectrum as observed with JWST. We summarise our conclusions as follows:

1. The presence of a scattering cloud reduces the emissivity of the atmosphere and leads to brightness temperatures that are smaller than real temperatures; this can been seen from Eq 4.7. We further show that even when the cloud has a constant single-scattering albedo, the emissivity of the atmosphere varies with wavelength. This results in spectral features being present due to the cloud even if the atmosphere is isothermal. Finally we show that the variation of SSA with wavelength can introduce additional cloud features in the emission spectrum.

2. We show that using a pure absorbing cloud, which is commonly used when interpreting clouds in exoplanet atmospheres, would lead to the inference of a systematically smaller than truth temperature gradient in an atmosphere with a non-inverted temperature profile. In the specific case of an isothermal atmosphere, the emission features produced by the thermal scattering would lead to the spurious detection of a thermal inversion. Similarly we find that

when the scattering is not taken into account, we retrieve the incorrect chemical abundance for the molecules in the atmosphere. This is important, as the fits from the pure absorbing cloud and the clouds that account for the scattering are of similar quality. Hence, if the scattering was not considered, we would be tricked into believing that the exoplanet atmosphere has a thermal inversion and the accompanying incorrect chemical abundances.

3. We develop a new three-parameter cloud parameterisation that can be used as an agnostic approach to fitting for clouds in emission. We show that the chemical abundance for a range of atmospheres with different cloud condensing species can be retrieved without assuming anything about the cloud. This is an improvement on what current models do, where an assumption about the cloud species is made before performing the retrieval (Venot et al., 2020); this assumption could bias the results.

4. We show that the three-parameter cloud parameterisation can also retrieve the general shape of the single-scattering albedo spectrum of the cloud. Despite the approach being agnostic to what sort of cloud is present, the retrieved single-scattering albedo can be compared to the single-scattering albedo of real species to infer the range of possible chemical composition and particle size distribution of the cloud.

In summary, this thesis has led to novel contributions to the field of exoplanet atmospheres. The contents of this thesis has currently led to 2 first author papers Taylor et al. (2020) and Taylor et al. (2021) with combined citations of 34[1]. Work from this thesis has resulted in 10 published co-author papers and 2 currently either in preparation or under review.

The 8 published co-author papers are:

1. Lee et al. (2019). Exoplanetary Monte Carlo radiative transfer with correlated-k - I. Benchmarking transit and emission observables. Monthly Notices of the Royal Astronomical Society 487, 2082–2096. doi:10.1093/mnras/stz1418
   Contributions: Ran all the NEMESIS models and performed the benchmark between NEMESIS and the framework presented in the paper.

2. Baudino et al. (2019). Towards the analysis of JWST exoplanet spectra: the effective temperature in the context of direct imaging. Monthly Notices of the

[1] As of July 12th 2021

Royal Astronomical Society 490, 2086–2090. doi:10.1093/mnras/stz2764
Contributions: Helped with writing the manuscript.

3. Irwin et al. (2020). 2.5D retrieval of atmospheric properties from exoplanet phase curves: application to WASP-43b observations. Monthly Notices of the Royal Astronomical Society 493, 106–125. doi:10.1093/mnras/staa238
Contributions: Ran models, provided models and helped with writing the manuscript.

4. Edwards et al. (2020a). ARES I: WASP-76 b, A Tale of Two HST Spectra. The Astronomical Journal 160. doi:10.3847/1538-3881/ab9225
Contributions: Helped with the implementation of H^- opacity into the TauREx framework.

5. Edwards et al. (2020b). Original Research By Young Twinkle Students (ORBYTS): Ephemeris Refinement of Transiting Exoplanets. Monthly Notices of the Royal Astronomical Society. doi:10.1093/mnras/staa1245
Contributions: Wrote the fitting algorithm used to fit the ephemerides.

6. Charnay et al. (2021). A survey of exoplanet phase curves with Ariel. Experimental Astronomy. doi:10.1007/s10686-021-09715-x
The contributions to this publication can be found in Appendix B.

7. May et al. (2021). Water Ice Cloud Variability and Multi-epoch Transmission Spectra of TRAPPIST-1e. The Astrophysical Journal 911.
The contributions to this publication can be found in Appendix C.

8. Tinetti et al. (2021). Ariel: Enabling planetary science across light-years. arXiv e-prints.
Contributions: Contributed to various Ariel projects since 2016.

9. Eisner et al. (2021). Planet Hunters TESS III: two transiting planets around the bright G dwarf HD 152843. Monthly Notices of the Royal Astronomical Society 505, 1827–1840.
Contributions: Computed all the atmospheric models and helped with writing the text.

10. Rathcke et al. (2021). HST PanCET Program: A Complete Near-UV to Infrared Transmission Spectrum for the Hot Jupiter WASP-79b. arXiv e-prints.

Contributions: The development of H^- opacity in NEMESIS from this thesis was used in this publication.

5.2 Future Directions

The future direction of retrieval analysis will focus on finding the balance between the complexity of the forward models used and the amount of information that can be extracted from the observations from telescopes such as JWST. There are two main areas that should be focused on when preparing for observations from future space missions: these are 1) developing and understanding multidimensional retrieval models to explore the spatial impacts of the objects and 2) improved cloud modelling in emission spectra, with a focus on how we can utilise the scattering properties of the clouds to learn about their composition and formation.

5.2.1 Multidimensional retrieval models

The multidimensional study in Chapter 3 builds a foundation for further exploration of the multidimensional effects that can impact our interpretation of exoplanet atmospheres. I plan to follow up this study by incorporating the horizontal variation of not only the temperature, but the chemical abundances and cloud coverage too. This is important to study as it has been found that correlations between chemical composition and thermal structure can lead to biased results for transmission spectra (e.g., Pluriel et al. (2020a)). I will take a simple to complex layering approach to understand how different assumptions affect the retrieved result and how to best counteract this in our models. To test the ability of the developed framework, I will use simulated observations based on the grid of non-grey General Circulation models, such as those published in Parmentier et al. (2016). By doing this, I will be able to determine the numerous pitfalls that 2D chemical and thermal structure can lead to and how the developed framework mitigates this. It is important to take a layered approach to the complexity, as this will ensure we understand the limits of the meaningful information we can obtain from JWST-quality data while developing the novel and robust modelling techniques for the community.

5.2.2 Cloud modelling in a retrieval framework

With JWST, we expect to observe clouds on the daysides of cooler (<1000K) exoplanets and nightsides of hot (>1200K) exoplanets (Beatty et al., 2019; Parmentier

et al., 2021). However, with the majority of current observations confined to the daysides of hotter exoplanets, predicted to be cloud-free (Parmentier et al., 2016), the inclusion of clouds in emission retrieval models has not generally been needed (Kreidberg et al., 2014; Line & Parmentier, 2016). Due to the lack of data of the dayside of cooler exoplanets, the exploration of how the clouds that form impact their emission spectrum have been limited. We need to explore these planet types in a theoretical framework to understand and develop models that will allow us to obtain the maximum amount of information possible from the data before becoming model-dependent. In Chapter 4, we explored the role that scattering clouds will play in extracting correct information from observations obtained with JWST and developed a new agnostic model which can retrieve the single-scattering albedo spectrum of the cloud. We find that our simple 3-parameter model cannot completely capture the complexities of the Ackerman & Marley model (Ackerman & Marley, 2001). This is likely due to our constant-with-altitude particle size and mixing. Future improvements on this work will include a hybrid approach between the "N-parameter" SSA retrieval and the vertical droplet parameterisation of the Ackerman & Marley model. The 3-parameter model is simplistic and only considered isotropic scattering. The impact of non-isotropic scattering needs to be explored in the retrieval framework, to understand how to best parameterise it and to assess its impact on future observations.

5.2.3 Optimal Estimation vs Nested Sampling?

It is now common practice to use a statistical technique such as MCMC or nested sampling to perform retrieval analysis of exoplanet atmospheres. However, we are moving into an era of higher signal-to-noise observations which require more free parameters to explore our problem. This poses the question: should we use an inverse technique such as optimal estimation in the future when high parameter spaces become unfeasible to compute with other techniques?

As explained in Chapter 2, the optimal estimation technique is widely used in the solar system community to retrieve atmospheric information from observations. The technique relies on the "initial guess" of the atmospheric state to be close to the "true" value, allowing for a rapid χ^2 fit to be performed in the local parameter space. The forward models used in solar system modelling can be more complex compared to those used to study exoplanets, such complexities are desirable for exoplanet studies. Therefore, we should learn from the solar system field how to interpret data using more complex models.

It has been shown by Line et al. (2013) that optimal estimation can perform just as well as techniques such as MCMC, the main disadvantage of the optimal estimation technique is that it requires prior information to be known about the exoplanet atmosphere, such as the abundances of molecules. This is information that we have for the solar system planets, but not for exoplanets. This does not necessarily need to be a disadvantage, it can be seen as an opportunity to think carefully about the prior information we use when studying the atmospheres of exoplanets. We can use our understanding of atmospheric physics to put a constraint on what the atmosphere *should* be like. This would result in thinking more about the problem and interpretation of the data. I see this as an advantage over the nested sampling or MCMC technique, as both these techniques can be used without thinking about the problem at hand, i.e., extremely wide priors can be put on each parameter, allowing the algorithm to find the best fitting result. However, as this thesis has shown, these techniques are prone to biases.

5.2.4 Recommendations for the Early Release Science and Guaranteed Time Observations data.

It is important to plan in advance on how to tackle the upcoming observations to ensure we are able to interpret the data correctly. As shown by Figure 3.2, emission spectra of hot planets observed at shorter wavelengths are more susceptible to multi-dimensional effects. Clouds will also have an impact and be a common opacity source in atmosphere of cool objects. These effects will impact an array of planned observations from the Early Release Science (ERS) program and the various Guaranteed Time Observations (GTO). The first three programs I describe I will be personally working on over the next couple of years.

1. GTO 1201 (PI David Lafrenière): This program will obtain eclipse measurements of HAT-P-1b, WASP-80b, WASP-107b, and GJ 3470b using NIRISS/SOSS. All of these measurements should have the scattering of clouds taken into consideration. This program will also obtain phase curve observations of WASP-121b and TOI-193b using NIRISS/SOSS. Scattering should be considered in these observations, especially given that clouds should form on the nightside of these objects. Multidimensional effects should only be considered for the phase curve observations in this program. The temperature of the planets in secondary eclipse are in a regime that has not been properly assessed for multidimensional effects, this should be investigated beforehand.

2. GO 2158 (PI Vivien Parmentier): This program will obtain the spectral phase curve of NGTS-10b using NIRSpec Prism. Results from this thesis show that multidimensional effects will need to be considered when performing spectral retrievals. The scattering properties of clouds need to be considered too, as we will observe the nightside of the planet where clouds should form.

3. ERS (PI Natalie Batalha): This program contains a full phase curve of WASP-43b using MIRI/LRS. This will result in 2 eclipse observations, one transit observation and then one complete observation of the full orbit. When analysing the extracted emission spectra of this target, we predict that multidimensional effects would not need to be considered due to the low signal-to-noise of the observation. However, when studying the spectral phase curve, multidimensional effects should be employed to fit the spectrum simultaneously at each phase angle, so that each phase angle observation is influencing the last. A technique that was employed in Irwin et al. (2020) should be applied to develop a structured map of the atmosphere. This observation will also let us study the nightside of the object. It has been shown by Venot et al. (2020) that the cloud features should be observable in the MIRI/LRS wavelength coverage. However, their lack of scattering made it difficult to extract the correct information from the data. Scattering due to the clouds needs to be considered for this object. This program will also obtain a secondary eclipse measurement of WASP-18b using NIRISS/SOSS. This target is an ultra-hot Jupiter and multidimensional effects should be considered. The effects of spatial information and different chemistry should be considered also, as the hot spot could potentially exhibit different chemical processes compared to the rest of the dayside atmosphere. It is unclear from current observations if scattering from clouds would need to be considered.

4. GTO 1177 (PI Thomas Green): This program contains eclipse observations of WASP-80b, WASP-69b, GJ 436b using MIRI/LRS and TRAPPIST-1b using MIRI/Imaging with the F1500W filter. All of these objects should have scattering considered apart from TRAPPIST-1b. The temperature of TRAPPIST-1b is around 400K, this temperature is too low to obtain discernible spectral features, hence the photometric route is being taken to make the first steps in *detecting* the thermal emission from the planet. Multidimensional effects should not be taken into account for eclipse measurements with MIRI/LRS as the signal-to-noise is expected to be low.

5. GTO 1185 (PI Thomas Green): This program is complementary to GTO 1177. It will observe the secondary eclipse of WASP-80b, WASP-69b, GJ 436b and HD 189733b using either NIRCam/F444W or NIRCam/F322W. Scattering should be considered in all analysis of these targets. By combining the observations with MIRI/LRS, multidimensional effects should be considered as the slope of the spectrum can be constrained better with a large wavelength coverage.

6. GTO 1224 (PI Stephan Birkmann): This program contains an eclipse measurement of WASP-52b using NIRSpec/PRISM and a phase curve measurement of WASP-43b using NIRSpec/G395H. Both should have scattering considered and both should consider multidimensional effects. WASP-52b is on the cooler side, but the large wavelength coverage of PRISM may result in the effects being detectable.

7. GTO 1279 (PI Pierre-Olivier Lagage): Similarly to GTO 1177, this program will obtain 5 secondary eclipse measurements of TRAPPIST-1b using MIRI/Imaging, but using the F1280W filter. The goal of the observations from GTO 1177 and GTO 1297 are the same and the observations should be combined to discover if thermal emission is detected in any of the spectral windows. Scattering does not need to be considered.

8. GTO 1312 (PI Nikole Lewis): This program contains the eclipse measurement of HAT-P-26b using NIRSpec/G395H and MIRI/LRS. The wide wavelength coverage will help to put the a constraint on the clouds and scattering will need to be considered. Multidimensional effects should be considered due to the large wavelength coverage.

9. GTO 1353 (PI Nikole Lewis): This program contains the eclipse measurement of WASP-17b using NIRISS/SOSS, NIRSpec/G395H and MIRI/LRS. Similar to GTO 1312, the wide wavelength coverage will help to put the a constraint on the clouds and scattering will need to be considered. Multidimensional effects should be considered due to the large wavelength coverage.

Appendix A

Benckmarking exercises

A.1 NEMESIS vs CHIMERA

The CHIMERA models used for this benchmark were generated by Dr Michael Line from Arizona State University.

CHIMERA (Line et al., 2013) is a radiative transfer and retrieval code, which was used in Chapter 4 to generate a physically driven cloud model that we used to investigate how well our single-scattering albedo parameterisation (from Chapter 2) performs. Before being able to correctly interpret the results, it is important that the codes are compared to each other in a simple way using the same setups. We do this so that we can verify that we get the same, or similar results. If this is the case, then we can rest assured that any differences that occur from comparing the cloud models are not due to the underlying setup of the codes, but due to the differences in the cloud modelling.

A.1.1 Forward Modelling

The first comparison is a simple forward modelling approach. We ask the question, if we use the same input values to our models, how similar will our outputs be?

For this comparison we assumed the physical planetary and stellar properties were of that of WASP-43b (Hellier et al., 2011), with planetary radius $R_p = 1.036 R_j$, planetary mass $M_p = 2.034\ M_j$, stellar radius $R_* = 0.667\ R_{sol}$ and separation D = 0.01526 au. For simplicity, the stellar model used for this test was a blackbody spectrum computed at 4500K.

For both models we assumed that the chemical volume mixing ratios were constant with altitude. These were $H_2O = 4\times10^{-4}$, $CO = 2\times10^{-4}$, $H_2 = 0.86$ and He=0.137.

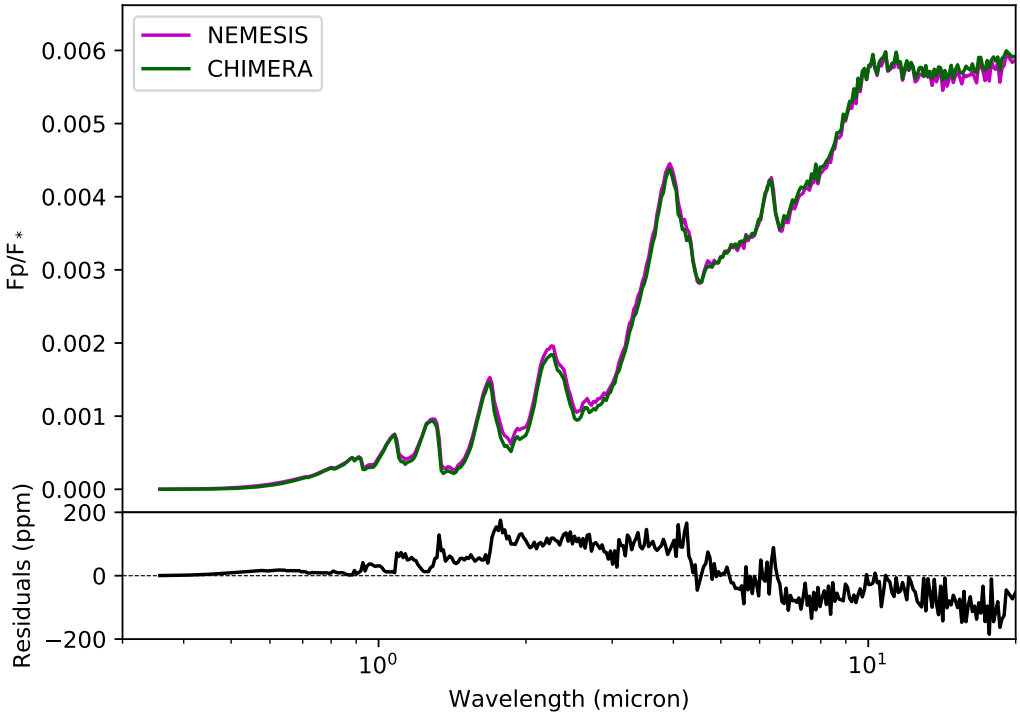


Figure A.1: Forward model comparisons between NEMESIS and CHIMERA. In purple we present the NEMESIS model and in green we present the CHIMERA model. The residuals are shown in the bottom panel.

The mean molecular weight of the atmosphere was assumed to be 2.31 grams. The temperature profile was generated using CHIMERA using the parameterisation described in Chapter 2, with $\log \kappa_{\rm IR}$ = -1.5, $\log \gamma_1 = \log \gamma_2$ = -1.0, α = 0.5 and $T_{\rm irr}$ = 1400K. This output was then used to generate the forward model in NEMESIS so that we were sure the temperature structure was the same in both models. The results of this forward modelling benchmark are shown in Figure A.1, where it can be seen that they agree at shorter wavelengths and begin to differ at longer wavelengths. Between 2 to 4 microns, NEMESIS exhibits higher flux and above these wavelengths exhibits lower flux than CHIMERA. Both models used the most up-to-date line-lists i.e., Polyansky et al. (2018) for H_2O and Li et al. (2015) for CO.

A.1.2 Retrieval Modelling

Given that the models slightly deviate in the forward modelling benchmark, we now ask the question: to what extent does this difference impact using NEMESIS to

retrieve on a model generated by CHIMERA? This is important to understand as multiple retrieval codes will be used to analyse the spectra obtained from JWST, so if there are differences in the models, we are able understand them and not attribute these biases to the data.

In this test the physical parameters of the star and the planet remain the same as the forward modelling test. The only difference between the forward modelling and retrieval modelling benchmark is the CHIMERA generated model has a slightly different temperature profile, with $\log \gamma_1 = \log \gamma_2 =$ -0.7. We perform a spectral retrieval on the CHIMERA model which has been given an error envelope of 60ppm. The best fitting model and temperature structure are presented in Figure A.2 and the corner plot is shown in Figure A.3. It can be seen from the residuals of the best fitting model that at all wavelengths the difference between the model and the data is within the 60ppm error bars. The retrieved parameters are in good agreement. At a first glance at Figure A.3 it would appear that NEMESIS did a bad job at retrieving the input parameters of CHIMERA. However, given that the error on each measurement is so precise the posterior distributions are very small. For example, the abundance of $\log(H_2O)$ is retrieved as -3.31 with an error of $\pm$0.05 dex, so despite the input value being -3.40 which is only 0.09 dex difference, the precise nature of the retrieved parameters exclude this value at the 1-σ level. Given that this precision would not be achieved with JWST, we can rest assured that the models are consistent.

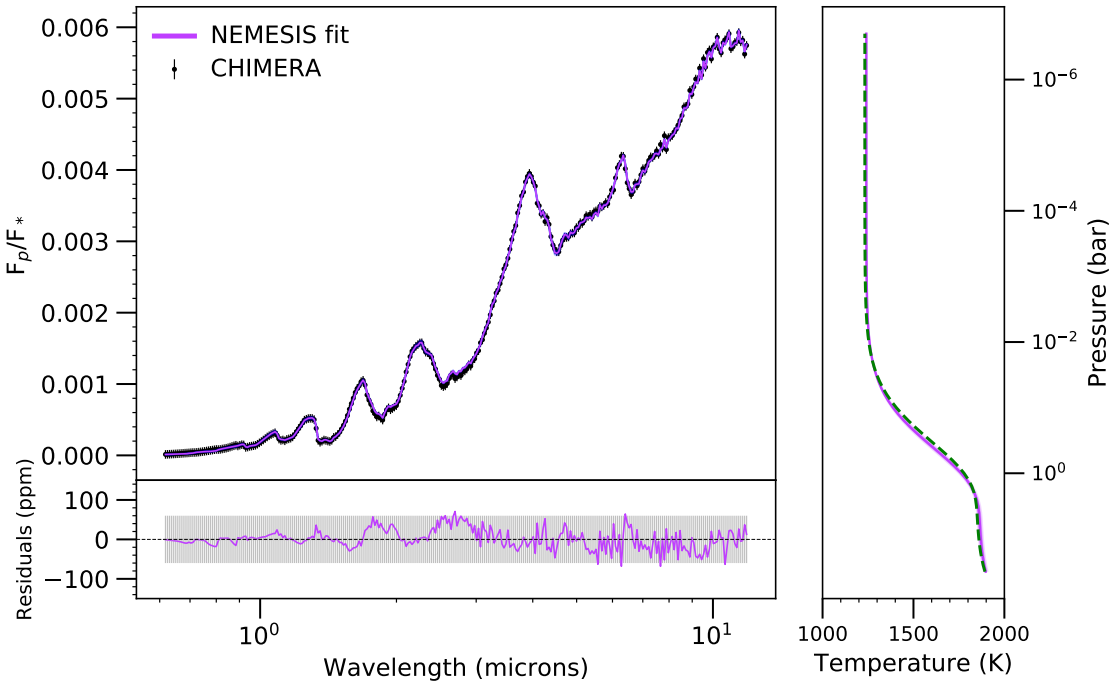


Figure A.2: The best fitting NEMESIS model to the data generated using CHIMERA. The bottom panel shows the residuals of the fit, with grey vertical lines showing the 60ppm error envelope. The right panel shows the retrieved thermal structure in purple and the input thermal structure using to generate the data in green.

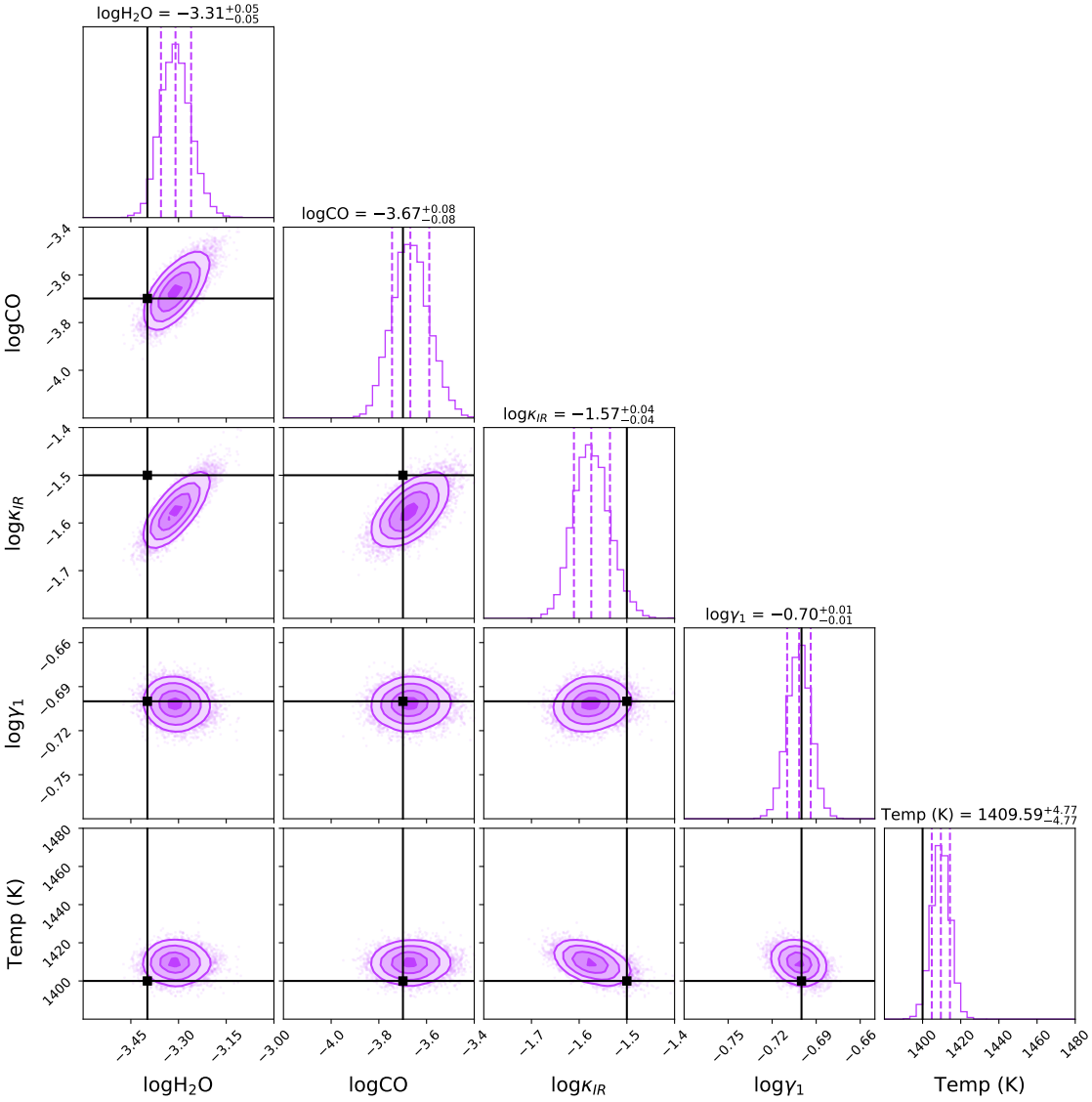


Figure A.3: The posterior distribution of the NEMESIS simulation that is shown in Figure A.2, the vertical black lines represent the true values that were used to generate the data.

Appendix B

Spectral Retrievals of hot Jupiter Phase Curves Observed with Ariel

The results presented here have been published in the journal Experimental Astronomy and can be found here Charnay et al. (2021). I detail here my contribution to this study. The simulated data that I retrieved on was generated by Dr João Mençonda. Dr Benjamin Charnay provided the error on the observations which were generated using Ariel-Rad.

To better understand the capability of Ariel[1] to reveal the global climate behaviour of planets, we performed 1D spectral retrievals on the disc average flux of WASP-43b produced by THOR (Mendonça et al., 2016). We chose to perform retrievals with a phase angle step of 60°. The error on the observations was estimated using Ariel-Rad for an integration time of 1 hour.

We used NEMESIS to perform the retrievals in this study, an outline of the code is presented in Chapter 2. The line lists used in the retrieval are the same as those used to calculate THOR's phase curves, apart from H_2O where NEMESIS uses a newer line-list (Polyansky et al., 2018). We model the atmosphere with a uniformly mixed vertical chemical structure and a temperature profile described in Chapter 2. Fig. B.1 shows the retrieved temperature profiles for the cloud-free WASP-43b simulation. The temperature retrieval shows that we can generally retrieve the gradient of the profile within 1-sigma and the vertical shape of the profile within 2-sigma, apart from at a phase angle of 300° which is slightly outside of 2-sigma at the lowest pressures.

Along with constraining the temperature structure, we wanted to explore if we can use the spectral phase curve to distinguish between atmospheres that are in equilibrium or disequilibrium. As seen in Fig. B.2, we find that our retrieved chemical

[1]The overview of this mission has been described in Chapter 1.

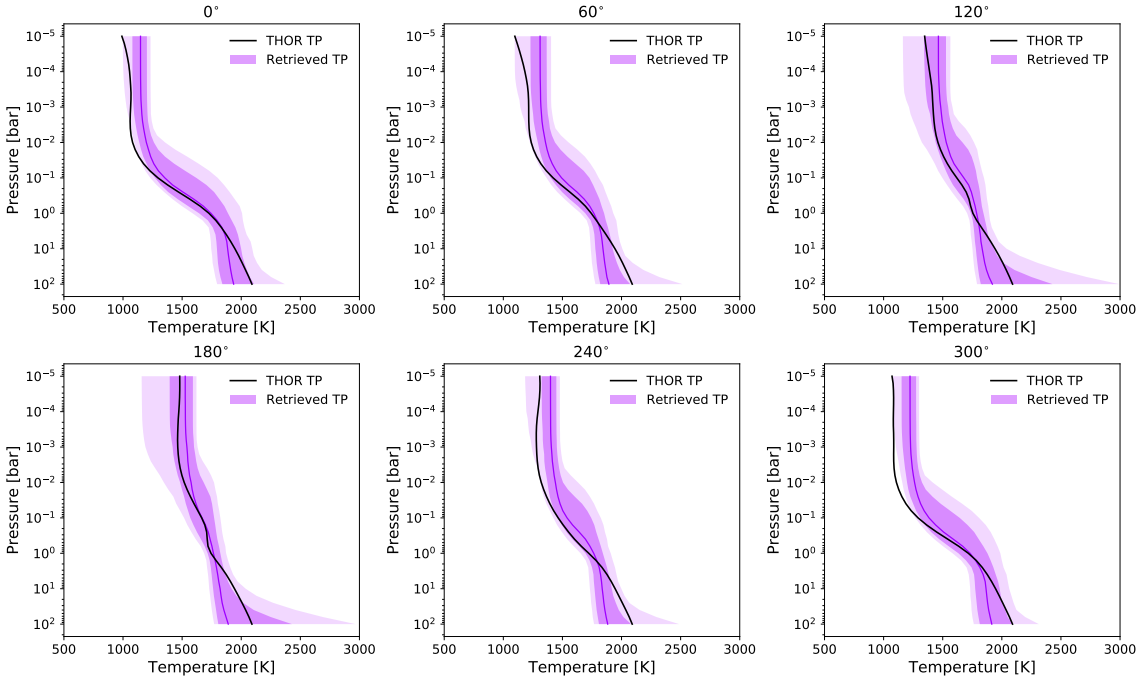


Figure B.1: Retrieved temperature structures for the cloud free WASP-43b numerical experiment. We present the median, 1-sigma and 2-sigma intervals in decreasing opacity of purple, and the temperature structure from THOR is presented in black.

abundances are within one sigma of the input value, with the tightest constraints being on the water abundance. We show that for H_2O and CO it is not possible to distinguish between the disequilibrium and equilibrium case, but it is possible for CO_2 and CH_4, with the greatest difference being for CH_4. It may however only be possible to put an upper limit on CH_4 and CO_2 due to their low abundance which results in less of an impact on the observed spectrum. We see from the chemistry retrieval that the error bars for CO are large for a phase angle of 180 degrees, this is due to the isothermal nature of the temperature-pressure profile in the region of the atmosphere to which we are sensitive to (i.e., around 0.1 bar), hence the features would appear muted and have a greater uncertainty.

We perform the same retrieval exercise for an atmosphere that is cloudy. To model the cloud in our retrieval framework we consider 3 extra parameters: the opacity of the cloud, the fractional scale height, and the cloud base pressure. We also assume that the cloud is non-scattering and grey in nature. We recognise that considering the scattering properties of the cloud could help to improve the retrieved atmospheric properties, this has been discussed in Chapter 4 of this thesis. We show the retrieved abundances in Fig. B.3 which demonstrates that we are able to detect

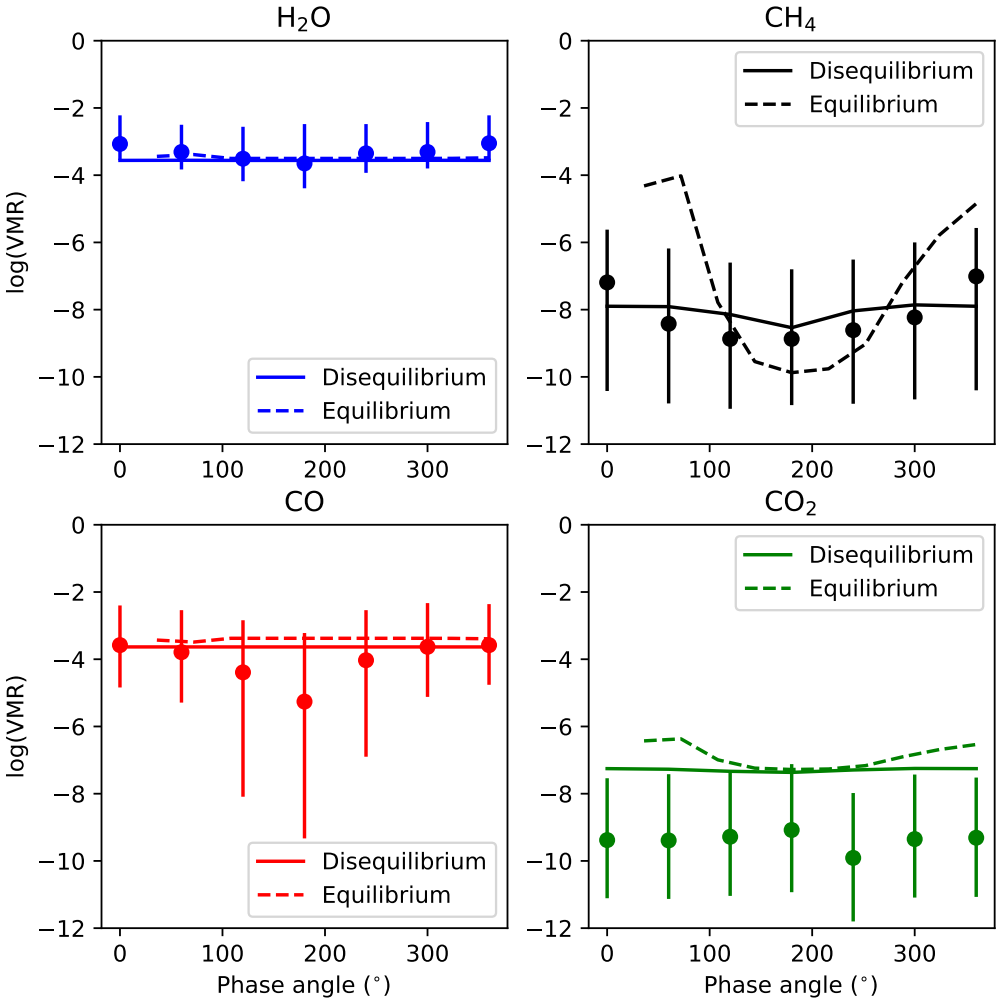


Figure B.2: Retrieved abundances (VMR) and associated uncertainty for the cloud-free WASP-43b simulations. They are shown by the vertical lines for each molecule. The horizontal solid and dashed lines are the disequilibrium and equilibrium abundances respectively, the values are taken to be around ∼0.1 to 0.01 bar, the region in which our simulations are sensitive to. Phase 0° and phase 180° correspond to the transit and the eclipse respectively. Synthetic observations use disequilibrium chemistry.

and constrain the abundance of H_2O with comparable precision to the cloud free scenario. We find that the other molecules are trickier to constrain due to the muted features introduced by the cloud. We present the retrieved thermal profiles in Fig. B.4 which demonstrates the inability to recover the shape of the thermal structure for

the cloudy atmosphere. The shape of the thermal structure calculated using THOR is not able to be captured by a Guillot-style parameterisation, given that this is one of the state-of-the-art thermal structure parameterisations used in exoplanet emission retrievals, we demonstrate that observations from future instruments will require a more complex temperature parameterisation for cloudy atmospheres.

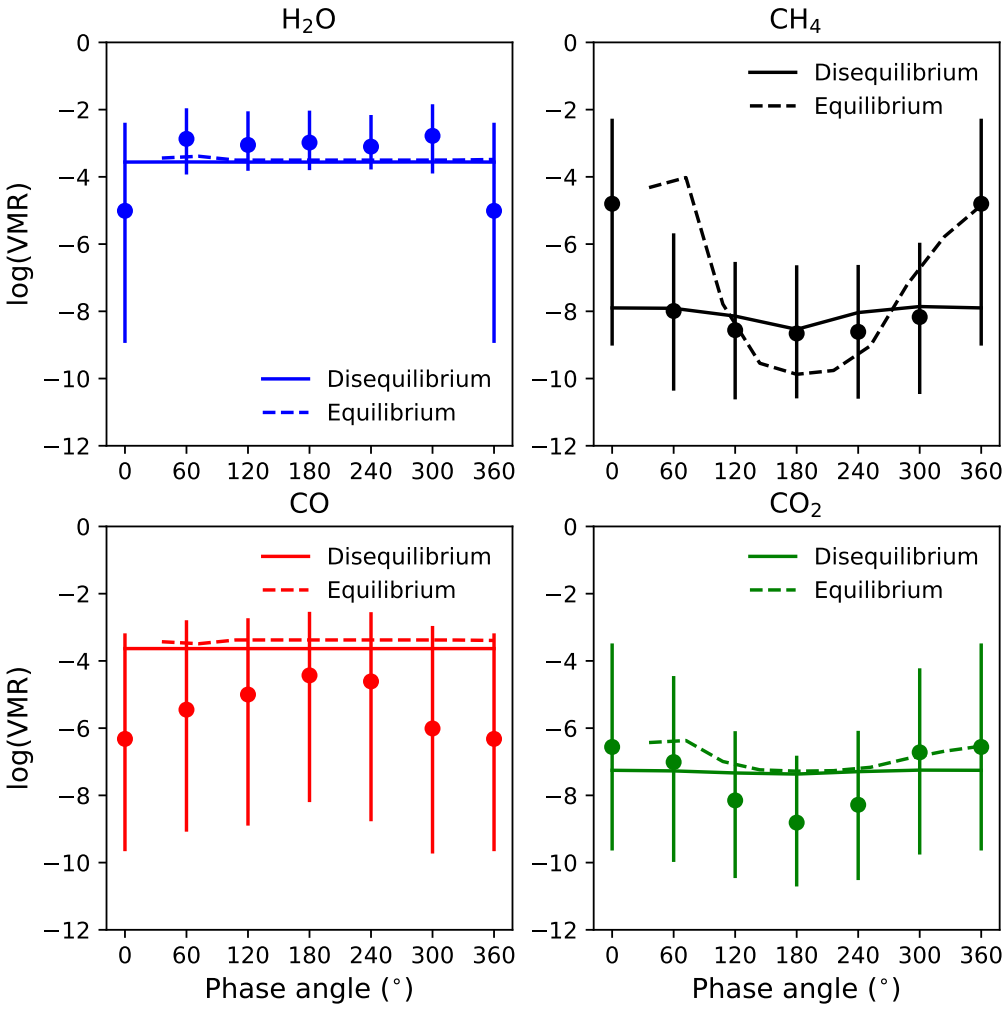


Figure B.3: Retrieved abundances (VMR) and associated uncertainty for the cloudy WASP-43b simulations. They are shown by the vertical lines for each molecule. The horizontal solid and dashed lines are the disequilibrium and equilibrium abundances respectively, the values are taken to be around ∼0.1 to 0.01 bar, the region in which our simulations are sensitive to. Phase 0° and phase 180° correspond to the transit and the eclipse respectively. Synthetic observations use disequilibrium chemistry.

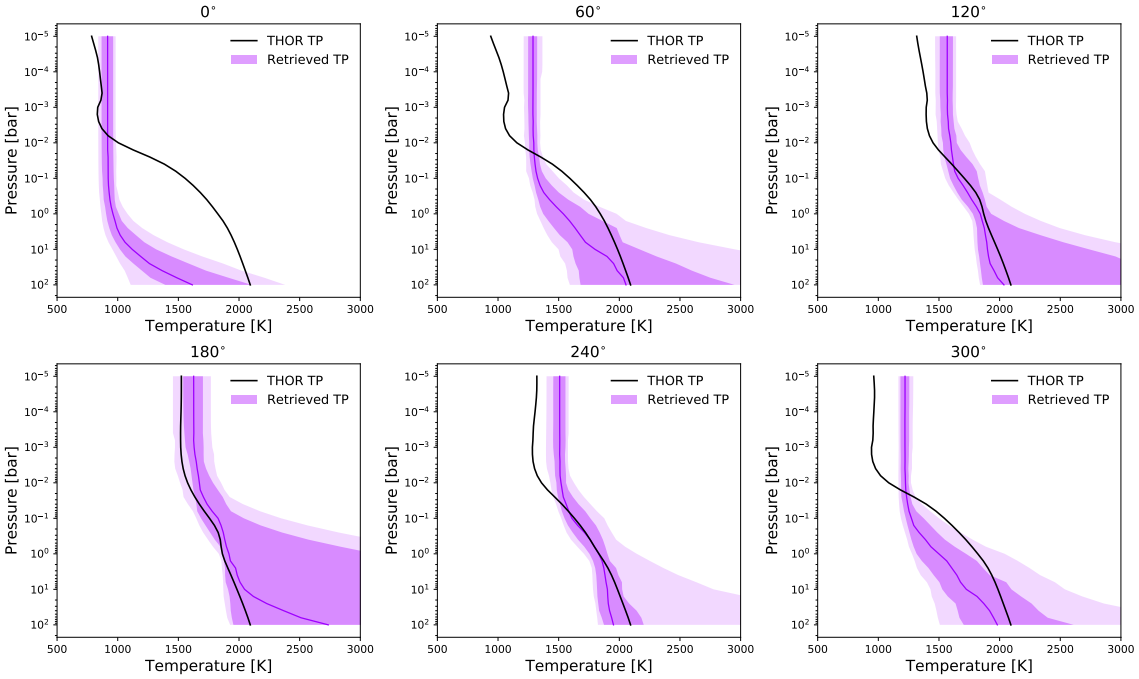


Figure B.4: Retrieved temperature structures for the cloudy WASP-43b numerical experiment. We present the median, 1-sigma and 2-sigma intervals in decreasing opacity of purple, and the temperature structure from THOR is presented in black.

Appendix C

Water Ice Cloud Variability & Multi-Epoch Transmission Spectra of TRAPPIST-1e

The results presented here have been accepted to the journal Astrophysical Journal Letters and can be found here May et al. (2021). I detail here my contribution to this study. The simulated data that I retrieved on was generated by Dr Erin May. Dr Thaddeus Komacek ran the GCM models which underline the atmosphere of the simulations.

C.1 Aims of the Study

In order to obtain the signal to noise needed to extract information from the atmosphere of terrestrial planets we need to perform multiple observations and then combine them together. This poses the question, if the cloud configuration is different in each observing instance, can we detect the difference in each model and does this affect the retrieved parameters of the planet.

C.2 Model Setup

Simulations were ran using a General Circulation Model for the exoplanet TRAPPIST-1e. It was ran for a year and at 10 random intervals in that year transmission spectra were generated of the current state of the atmosphere to ensure that the cloud configuration at each interval was varying as if the observations were happening at different times. These simulations were then converted into NIRSpec PRISM observations using PandExo and all 10 observations combined together. 10 observations were chosen

as this has been shown in previous studies to the amount of observations needed to achieved the signal-to-noise to obtained atmospheric information (Krissansen-Totton et al., 2018).

C.3 Atmospheric Retrievals

To perform our retrievals we use the open source radiative transfer and retrieval framework `CHIMERA` (Line et al., 2013). It previously has been used to study the atmosphere of TRAPPIST-1e to determine the resolution that a future instrument needs to have in order to detect and constrain the abundances of molecules in the atmospheres of temperate terrestrial planets to high precision (Tremblay et al., 2020). Our retrieval set up is similar to that presented in Tremblay et al. (2020). For each of the combined spectra we fit for 6 parameters: an isothermal temperature profile (T_{iso}), a radius scaling factor (xR_p), the cloud top pressure (log(CTP)), the mean molecular weight of the atmosphere and the volume mixing ratio of H_2O and CO_2. We use the mean molecular weight (MMW) as a proxy to effectively fill the rest of the atmosphere with N_2 as this molecule is inert.

C.4 Results

Each spectra that we retrieved on had a different underlying cloud configuration, hence we want to determine if these physical processes impact the retrieved CO_2 abundance. The histograms presented in Figure C.2 show that the retrieved abundances are consistent for each of the combined spectra, suggesting that the impact of cloud variability is not detectable with the resolution provided by JWST NIRSpec PRISM. This is further verified by the 3rd panel which shows consistent retrieved cloud top pressure for each spectra. It can be seen from Figure C.2 that for the CO_2 partial pressure greater than 10^{-1} bars the posterior tends towards the upper prior which is set by the physical limit of the volume mixing ratio, with the true value lying outside 1-σ. The lower partial pressures are not prior dominated and we are able to retrieve the correct volume mixing ratios within 1-σ. It can be seen that our 10 cases for each partial pressure are consistent, suggesting that the variable clouds are not affecting the retrieved values. Further, we are unable to constrain a water abundance due to its lack of strong spectral features in our models.

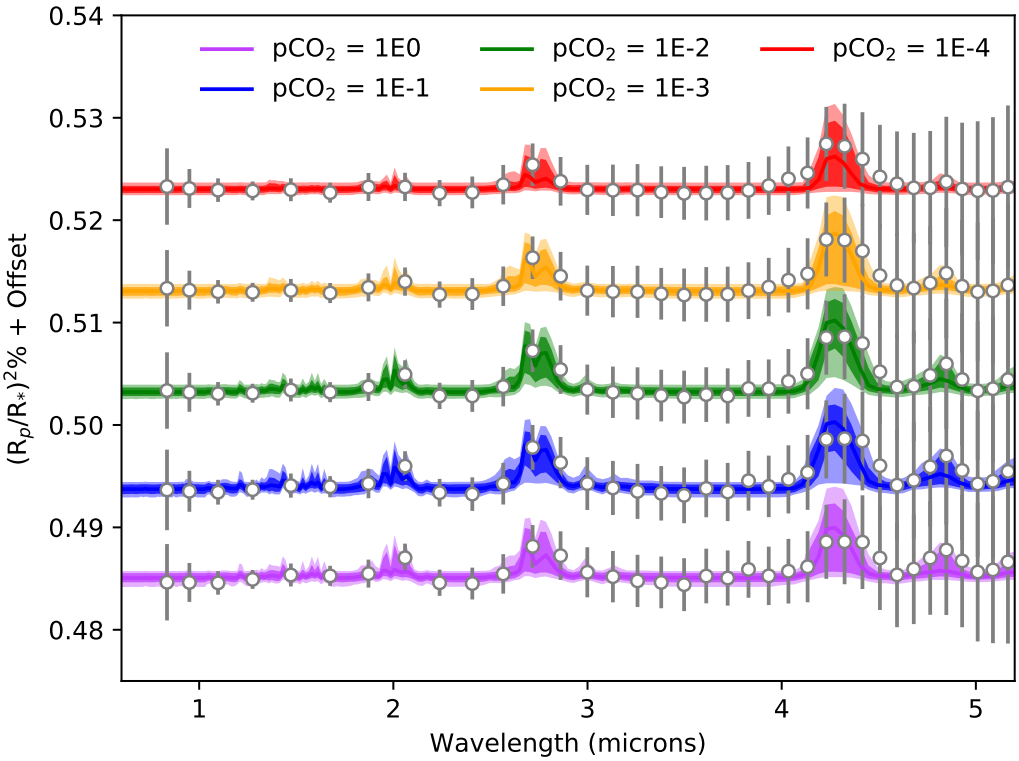


Figure C.1: Sample retrieved spectra. Each line represents a different pCO_2 case for a single multi-epoch case. 1- and 2- σ contours are included.

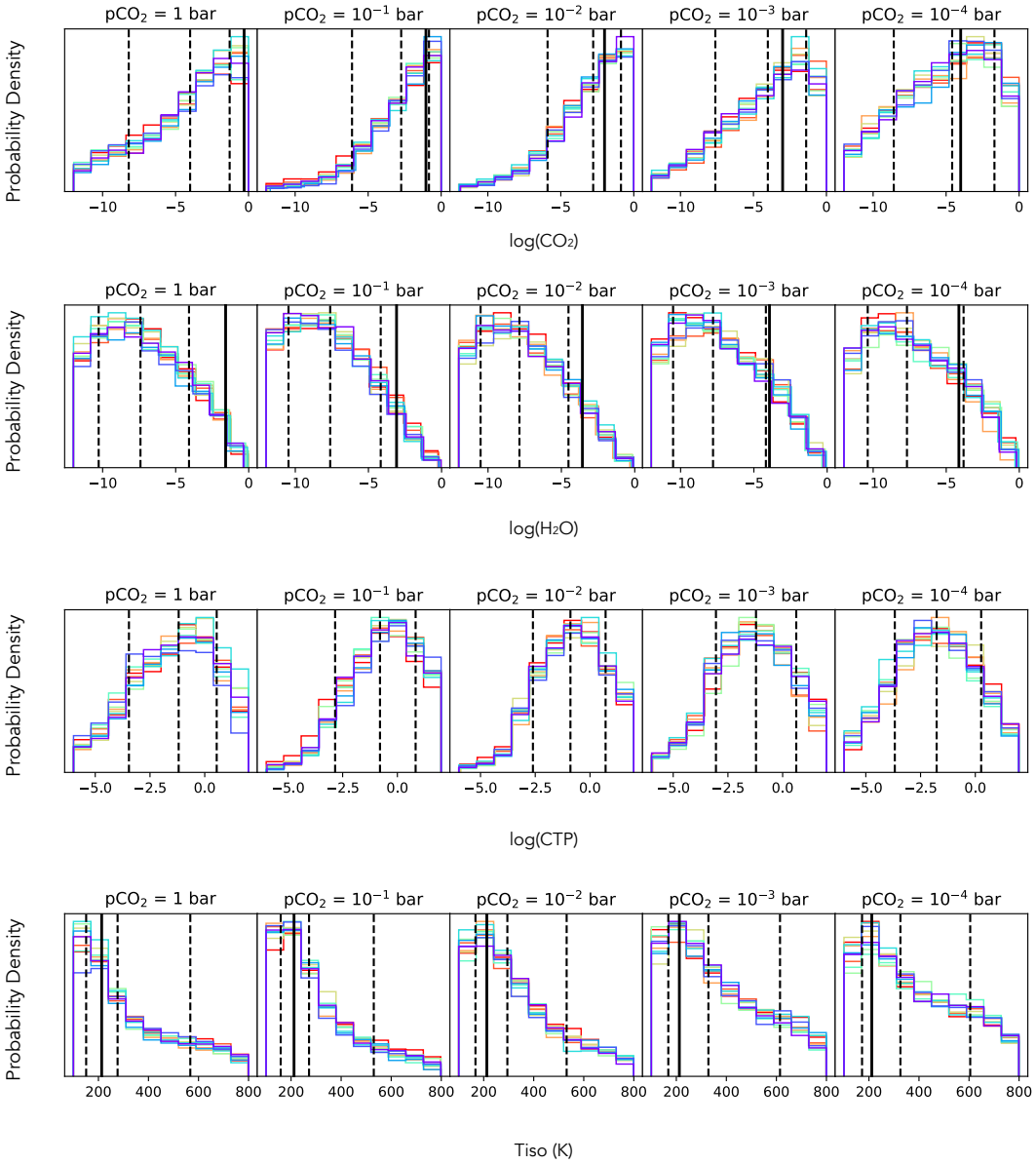


Figure C.2: The retrieved posterior distributions for 4 of the key parameters explored in this study. From top to bottom the 4 panels are: CO_2 abundance, H_2O abundance, cloud top pressure and temperature. Each coloured histogram represents the retrieved parameter for 1 of the combined spectra (representing 10 different "observed" epochs), for a total 10 different combined spectra, each with different underlying cloud assumption. The thick solid vertical lines show the terminator-average abundance of CO_2 and H_2O from the input models, while the dotted vertical lines represent the best fit value and the 1-σ constraints on it. With the exception of the 1 bar pCO_2 case, the true CO_2 value is within 1-σ of the retrieved values. We present the 0.1 bar temperature as a solid vertical line in the temperature histograms. It is not possible to present a "true" value for the cloud top pressure as this is different for each scenario. The consistency of the retrieved cloud top pressures demonstrates that the precision of the data is not high enough to detect this variability.

Appendix D

Derivation of the General Radiative Transfer Equation from Rutten (2003)

In this section we attempt to summarise the general case for the radiative transfer equation. For a more in depth look, we recommend the work in Rutten (2003), which greatly helped our understanding of how scattering affects the planetary flux.

D.1 General case

Let us first consider the radiative transfer equation (RTE) in plane-parallel geometry:

$$\mu \frac{dI_\lambda}{d\tau_\lambda} = I_\lambda - S_\lambda \tag{D.1}$$

here $d\tau_\lambda = -\kappa_\lambda \rho dr$, where κ_λ is the wavelength-dependent opacity (also known as the cross section per unit mass, with units $\mathrm{cm}^2\mathrm{g}^{-1}$) and ρ is the density in units $\mathrm{cm}^{-3}\mathrm{g}$. The intensity is I_λ and the source function is S_λ.

If we consider that the source function is isotropic and average over all angles we get:

$$\frac{1}{2}\int_{-1}^{+1} \mu \frac{dI_\lambda}{d\tau_\lambda} d\mu = \frac{1}{2}\int_{-1}^{+1} I_\lambda d\mu - \frac{1}{2}\int_{-1}^{+1} S_\lambda d\mu \tag{D.2}$$

By considering the different moments of intensity we respect to μ we can write this equation as:

$$\frac{dH_\lambda}{d\tau_\lambda} = J_\lambda - S_\lambda \tag{D.3}$$

Where H_λ is the second order moment, otherwise know as the Eddington flux; it can be related to the flux by $H_\lambda = \frac{F_\lambda}{4}$. J_λ is the first order moment, otherwise know as the mean intensity.

If we multiply Equation D.1 by μ and then average over all angles we instead get:

$$\frac{1}{2}\int_{-1}^{+1} \mu^2 \frac{dI_\lambda}{d\tau_\lambda} d\mu = \frac{1}{2}\int_{-1}^{+1} \mu I_\lambda d\mu - \frac{1}{2}\int_{-1}^{+1} \mu S_\lambda d\mu \tag{D.4}$$

which can be written in terms of the moments on intensity as:

$$\frac{dK_\lambda}{d\tau_\lambda} = H_\lambda \tag{D.5}$$

Here K_λ is the third-order moment of the intensity and is known as the K integral. We lose the source term as this goes to zero due to it being isotropic. We can then use Equation D.3 and Equation D.5 to get:

$$\frac{d^2K_\lambda}{d\tau_\lambda^2} = J_\lambda - S_\lambda \tag{D.6}$$

Hence, we now have a second order differential version of the radiative transfer equation.

We can now relate K_λ with J_λ by considering the following:

$$K_\lambda = \frac{1}{2}\int_{-1}^{+1} \mu^2 I_\lambda d\mu = \frac{1}{2} < I_\lambda > \int_{-1}^{+1} \mu^2 d\mu = \frac{1}{3} J_\lambda \tag{D.7}$$

This relation is known as the first order Eddington approximation, using this we can write Equation D.6 as:

$$\frac{1}{3}\frac{d^2J_\lambda}{d\tau_\lambda^2} = J_\lambda - S_\lambda. \tag{D.8}$$

If we consider that the scattering is elastic, the source function becomes

$$S_\lambda = (1-\epsilon_\lambda)J_\lambda - \epsilon_\lambda B_\lambda \tag{D.9}$$

and we can then write the radiative transfer equation as

$$\frac{1}{3}\frac{d^2J_\lambda}{d\tau_\lambda^2} = \epsilon_\lambda(J_\lambda - B_\lambda). \tag{D.10}$$

Let us now assume that the Planck function varies linearly with optical depth

$$B_\lambda(\tau_\lambda) = B_{\lambda,0} + b_\lambda \tau_\lambda \tag{D.11}$$

which results in the second order differential of the Planck function to be zero ($\frac{d^2 B_\lambda}{d\tau_\lambda^2} = 0$) and therefore we can rewrite Equation D.10 as

$$\frac{1}{3}\left(\frac{d^2 J_\lambda}{d\tau_\lambda^2} - \frac{d^2 B_\lambda}{d\tau_\lambda^2}\right) = \epsilon_\lambda (J_\lambda - B_\lambda). \tag{D.12}$$

as this does not change the result of Equation D.10. We can simplify this by writing it in the form

$$\frac{1}{3}\frac{d^2}{d\tau_\lambda^2}(J_\lambda - B_\lambda) = \epsilon_\lambda (J_\lambda - B_\lambda) \tag{D.13}$$

which can be integrated to find the difference between J_λ and B_λ

$$J_\lambda - B_\lambda = C_1 e^{-\sqrt{3\epsilon_\lambda}\tau_\lambda} + C_2 e^{\sqrt{3\epsilon_\lambda}\tau_\lambda} \tag{D.14}$$

where C_1 and C_2 are integration constants that can be found by applying a few boundary conditions. These boundary conditions are that $J_\lambda = B_\lambda$ for $\tau_\lambda \to \infty$ and no incident flux at $\tau_\lambda = 0$ hence in the Rosseland approximation. This results in $C_2 = 0$, to find C_1 we adopted the second Eddington approximation $J_\lambda(0) = a_\lambda H_\lambda(0)$, note that the second Eddington approximation is $J_\lambda(0) = 2H_\lambda(0)$ for an unrealistic Lambert radiator, we therefore use a_λ as a free parameter.

$$J_\lambda(0) = B_{\lambda,0} + C_1 \tag{D.15}$$

$$\begin{aligned} J_\lambda(0) = a_\lambda H_\lambda(0) = a_\lambda \Big[\frac{dK_\lambda}{d\tau_\lambda}\Big]_{\tau_\lambda=0} &= (a_\lambda/3)\Big[\frac{dJ_\lambda}{d\tau_\lambda}\Big]_{\tau_\lambda=0} \\ &= -(a_\lambda/3)\sqrt{3\epsilon_\lambda} C_1 + a_\lambda b_\lambda/3 \end{aligned} \tag{D.16}$$

By combining Equation D.15 and D.16 we find C_1 to be

$$C_1 = -\frac{B_{\lambda,0} - a_\lambda b_\lambda/3}{1 + (a_\lambda/3)\sqrt{3\epsilon_\lambda}} \tag{D.17}$$

and if we substitute Equation D.17 into D.14 we can find the general scattering solutions for $J_\lambda(\tau_\lambda)$, $S_\lambda(\tau_\lambda)$ and $H_\lambda(\tau_\lambda)$. Hence

$$J_\lambda(\tau_\lambda) = B_{\lambda,0} + b_\lambda \tau_\lambda - \frac{B_{\lambda,0} - a_\lambda b_\lambda/3}{1 + (a_\lambda/3)\sqrt{3\epsilon_\lambda}} e^{-\sqrt{3\epsilon_\lambda}\tau_\lambda} \tag{D.18}$$

$$S_\lambda(\tau_\lambda) = B_{\lambda,0} + b_\lambda \tau_\lambda - (1-\epsilon_\lambda)\frac{B_{\lambda,0} - a_\lambda b_\lambda/3}{1 + (a_\lambda/3)\sqrt{3\epsilon_\lambda}} e^{-\sqrt{3\epsilon_\lambda}\tau_\lambda} \tag{D.19}$$

$$H_\lambda(\tau_\lambda) = b_\lambda/3 + \sqrt{\epsilon_\lambda}\frac{B_{\lambda,0} - a_\lambda b_\lambda/3}{\sqrt{3} + a_\lambda\sqrt{\epsilon_\lambda}} e^{-\sqrt{3\epsilon_\lambda}\tau_\lambda} \tag{D.20}$$

As in Rutten (2003) we assume $a_\lambda = \sqrt{3}$ and assume that the planetary flux is given by $F_p = 4\pi H$, we can substitute in the value for $H_\lambda(\tau_\lambda)$ we just found to get

$$F_p = 4\pi \left(\frac{b_\lambda}{3} - \frac{\sqrt{\epsilon_\lambda}}{1+\sqrt{\epsilon_\lambda}} b_\lambda + \frac{\sqrt{\epsilon_\lambda}}{1+\sqrt{\epsilon_\lambda}} \frac{1}{\sqrt{3}} B_\lambda(0) \right) \tag{D.21}$$

which can be re-written as:

$$F_p = 4\pi \frac{2\sqrt{\epsilon_\lambda}}{1+\sqrt{\epsilon_\lambda}} \left(B_\lambda(0) + \frac{b_\lambda}{\sqrt{3\epsilon_\lambda}} \right) \tag{D.22}$$

Or also:

$$F_p = \frac{2\pi}{\sqrt{3}} \frac{2\sqrt{\epsilon_\lambda}}{1+\sqrt{\epsilon_\lambda}} B_\lambda(\tau_\lambda = 1/\sqrt{3\epsilon_\lambda}) \tag{D.23}$$

Bibliography

Ackerman, A. S. & Marley, M. S. 2001, ApJ, 556, 872

Amundsen, D. S., Tremblin, P., Manners, J., Baraffe, I., & Mayne, N. J. 2017, A&A, 598, A97

Arcangeli, J., Désert, J.-M., Line, M. R., Bean, J. L., Parmentier, V., Stevenson, K. B., Kreidberg, L., Fortney, J. J., Mansfield, M., & Showman, A. P. 2018, ApJ Lett., 855, L30

Arcangeli, J., Désert, J.-M., Parmentier, V., Stevenson, K. B., Bean, J. L., Line, M. R., Kreidberg, L., Fortney, J. J., & Showman, A. P. 2019, A&A, 625, A136

Barstow, J. K. 2020, MNRAS, 497, 4183

Barstow, J. K., Aigrain, S., Irwin, P. G. J., Hackler, T., Fletcher, L. N., Lee, J. M., & Gibson, N. P. 2014, ApJ, 786, 154

Barstow, J. K., Aigrain, S., Irwin, P. G. J., Kendrew, S., & Fletcher, L. N. 2015, MNRAS, 448, 2546

Barstow, J. K., Aigrain, S., Irwin, P. G. J., & Sing, D. K. 2017, ApJ, 834, 50

Batalha, N. E., Mandell, A., Pontoppidan, K., Stevenson, K. B., Lewis, N. K., Kalirai, J., Earl, N., Greene, T., Albert, L., & Nielsen, L. D. 2017, PASP, 129, 064501

Baudino, J.-L., Taylor, J., Irwin, P. G. J., & Garland, R. 2019, MNRAS, 490, 2086

Bauduin, S., Irwin, P. G. J., Lellouch, E., Cottini, V., Moreno, R., Nixon, C. A., Teanby, N. A., Ansty, T., & Flasar, F. M. 2018, Icar., 311, 288

Baxter, C., Désert, J.-M., Parmentier, V., Line, M., Fortney, J., Arcangeli, J., Bean, J. L., Todorov, K. O., & Mansfield, M. 2020, A&A, 639, A36

Bean, J. L., Stevenson, K. B., Batalha, N. M., Berta-Thompson, Z., Kreidberg, L., Crouzet, N., Benneke, B., Line, M. R., Sing, D. K., Wakeford, H. R., Knutson, H. A., Kempton, E. M. R., Désert, J.-M., Crossfield, I., Batalha, N. E., de Wit, J., Parmentier, V., Harrington, J., Moses, J. I., Lopez-Morales, M., Alam, M. K., Blecic, J., Bruno, G., Carter, A. L., Chapman, J. W., Decin, L., Dragomir, D., Evans, T. M., Fortney, J. J., Fraine, J. D., Gao, P., García Muñoz, A., Gibson, N. P., Goyal, J. M., Heng, K., Hu, R., Kendrew, S., Kilpatrick, B. M., Krick, J., Lagage, P.-O., Lendl, M., Louden, T., Madhusudhan, N., Mandell, A. M., Mansfield, M., May, E. M., Morello, G., Morley, C. V., Nikolov, N., Redfield, S., Roberts, J. E., Schlawin, E., Spake, J. J., Todorov, K. O., Tsiaras, A., Venot, O., Waalkes, W. C., Wheatley, P. J., Zellem, R. T., Angerhausen, D., Barrado, D., Carone, L., Casewell, S. L., Cubillos, P. E., Damiano, M., de Val-Borro, M., Drummond, B., Edwards, B., Endl, M., Espinoza, N., France, K., Gizis, J. E., Greene, T. P., Henning, T. K., Hong, Y., Ingalls, J. G., Iro, N., Irwin, P. G. J., Kataria, T., Lahuis, F., Leconte, J., Lillo-Box, J., Lines, S., Lothringer, J. D., Mancini, L., Marchis, F., Mayne, N., Palle, E., Rauscher, E., Roudier, G., Shkolnik, E. L., Southworth, J., Swain, M. R., Taylor, J., Teske, J., Tinetti, G., Tremblin, P., Tucker, G. S., van Boekel, R., Waldmann, I. P., Weaver, I. C., & Zingales, T. 2018, PASP, 130, 114402

Beatty, T. G., Madhusudhan, N., Tsiaras, A., Zhao, M., Gilliland, R. L., Knutson, H. A., Shporer, A., & Wright, J. T. 2017, AJ, 154, 158

Beatty, T. G., Marley, M. S., Gaudi, B. S., Colón, K. D., Fortney, J. J., & Showman, A. P. 2019, AJ, 158, 166

Bell, T. J. & Cowan, N. B. 2018, ApJ Lett., 857, L20

Bell, T. J., Dang, L., Cowan, N. B., Bean, J., Désert, J.-M., Fortney, J. J., Keating, D., Kempton, E., Kreidberg, L., Line, M. R., Mansfield, M., Parmentier, V., Stevenson, K. B., Swain, M., & Zellem, R. T. 2020, arXiv e-prints, arXiv:2010.00687

Benneke, B., Knutson, H. A., Lothringer, J., Crossfield, I. J. M., Moses, J. I., Morley, C., Kreidberg, L., Fulton, B. J., Dragomir, D., Howard, A. W., Wong, I., Désert, J.-M., McCullough, P. R., Kempton, E. M. R., Fortney, J., Gilliland , R., Deming, D., & Kammer, J. 2019, Nature Astronomy, 3, 813

Bourrier, V., Kitzmann, D., Kuntzer, T., Nascimbeni, V., Lendl, M., Lavie, B., Hoeijmakers, H. J., Pino, L., Ehrenreich, D., Heng, K., Allart, R., Cegla, H. M.,

Dumusque, X., Melo, C., Astudillo-Defru, N., Caldwell, D. A., Cretignier, M., Giles, H., Henze, C. E., Jenkins, J., Lovis, C., Murgas, F., Pepe, F., Ricker, G. R., Rose, M. E., Seager, S., Segransan, D., Suárez-Mascareño, A., Udry, S., Vanderspek, R., & Wyttenbach, A. 2020, A&A, 637, A36

Braude, A. S., Irwin, P. G. J., Orton, G. S., & Fletcher, L. N. 2020, Icar., 338, 113589

Buchner, J., Georgakakis, A., Nandra, K., Hsu, L., Rangel, C., Brightman, M., Merloni, A., Salvato, M., Donley, J., & Kocevski, D. 2014, A&A, 564, A125

Burningham, B., Marley, M. S., Line, M. R., Lupu, R., Visscher, C., Morley, C. V., Saumon, D., & Freedman, R. 2017, MNRAS, 470, 1177

Carter, A. L., Nikolov, N., Sing, D. K., Alam, M. K., Goyal, J. M., Mikal-Evans, T., Wakeford, H. R., Henry, G. W., Morrell, S., López-Morales, M., Smalley, B., Lavvas, P., Barstow, J. K., García Muñoz, A., Gibson, N. P., & Wilson, P. A. 2020, MNRAS, 494, 5449

Castelli, F. & Kurucz, R. L. 2003, in Modelling of Stellar Atmospheres, ed. N. Piskunov, W. W. Weiss, & D. F. Gray, Vol. 210, A20

Changeat, Q. & Edwards, B. 2021, ApJ Lett., 907, L22

Changeat, Q., Edwards, B., Waldmann, I. P., & Tinetti, G. 2019, ApJ, 886, 39

Charbonneau, D., Allen, L. E., Megeath, S. T., Torres, G., Alonso, R., Brown, T. M., Gilliland, R. L., Latham, D. W., Mandushev, G., O'Donovan, F. T., & Sozzetti, A. 2005, ApJ, 626, 523

Charnay, B., Mendonça, J. M., Kreidberg, L., Cowan, N. B., Taylor, J., Bell, T. J., Demangeon, O., Edwards, B., Haswell, C. A., Morello, G., Mugnai, L. V., Pascale, E., Tinetti, G., Tremblin, P., & Zellem, R. T. 2021, Experimental Astronomy

Chubb, K. L., Min, M., Kawashima, Y., Helling, C., & Waldmann, I. 2020a, A&A, 639, A3

Chubb, K. L., Rocchetto, M., Yurchenko, S. N., Min, M., Waldmann, I., Barstow, J. K., Mollière, P., Al-Refaie, A. F., Phillips, M. W., & Tennyson, J. 2020b, arXiv e-prints, arXiv:2009.00687

Cowan, N. B. & Agol, E. 2008, ApJ Lett., 678, L129

Cowan, N. B., Machalek, P., Croll, B., Shekhtman, L. M., Burrows, A., Deming, D., Greene, T., & Hora, J. L. 2012, ApJ, 747, 82

Crossfield, I. J. M., Knutson, H., Fortney, J., Showman, A. P., Cowan, N. B., & Deming, D. 2012, ApJ, 752, 81

Cubillos, P., Harrington, J., Madhusudhan, N., Stevenson, K. B., Hardy, R. A., Blecic, J., Anderson, D. R., Hardin, M., & Campo, C. J. 2013, ApJ, 768, 42

Cushing, M. C., Roellig, T. L., Marley, M. S., Saumon, D., Leggett, S. K., Kirkpatrick, J. D., Wilson, J. C., Sloan, G. C., Mainzer, A. K., Van Cleve, J. E., & Houck, J. R. 2006, ApJ, 648, 614

Dang, L., Cowan, N. B., Schwartz, J. C., Rauscher, E., Zhang, M., Knutson, H. A., Line, M., Dobbs-Dixon, I., Deming, D., Sundararajan, S., Fortney, J. J., & Zhao, M. 2018, Nature Astronomy, 2, 220

Daylan, T., Günther, M. N., Mikal-Evans, T., Sing, D. K., Wong, I., Shporer, A., Niraula, P., de Wit, J., Koll, D. D. B., Parmentier, V., Fetherolf, T., Kane, S. R., Ricker, G. R., Vanderspek, R., Seager, S., Winn, J. N., Jenkins, J. M., Caldwell, D. A., Charbonneau, D., Henze, C. E., Paegert, M., Rinehart, S., Rose, M., Sha, L., Quintana, E., & Villasenor, J. N. 2021, The Astronomical Journal, 161, 131

de Kok, R. J., Helling, C., Stam, D. M., Woitke, P., & Witte, S. 2011, A&A, 531, A67

Deming, D., Seager, S., Richardson, L. J., & Harrington, J. 2005, Natur., 434, 740

Deming, D., Wilkins, A., McCullough, P., Burrows, A., Fortney, J. J., Agol, E., Dobbs-Dixon, I., Madhusudhan, N., Crouzet, N., Desert, J.-M., Gilliland, R. L., Haynes, K., Knutson, H. A., Line, M., Magic, Z., Mand ell, A. M., Ranjan, S., Charbonneau, D., Clampin, M., Seager, S., & Showman, A. P. 2013, ApJ, 774, 95

Diamond-Lowe, H., Stevenson, K. B., Bean, J. L., Line, M. R., & Fortney, J. J. 2014, ApJ, 796, 66

Dransfield, G. & Triaud, A. H. M. J. 2020, MNRAS, 499, 505

Edwards, B., Changeat, Q., Baeyens, R., Tsiaras, A., Al-Refaie, A., Taylor, J., Yip, K. H., Bieger, M. F., Blain, D., Gressier, A., Guilluy, G., Jaziri, A. Y., Kiefer, F., Modirrousta-Galian, D., Morvan, M., Mugnai, L. V., Pluriel, W., Poveda, M., Skaf,

N., Whiteford, N., Wright, S., Zingales, T., Charnay, B., Drossart, P., Leconte, J., Venot, O., Waldmann, I., & Beaulieu, J.-P. 2020a, AJ, 160, 8

Edwards, B., Changeat, Q., Yip, K. H., Tsiaras, A., Taylor, J., Akhtar, B., AlDaghir, J., Bhattarai, P., Bhudia, T., Chapagai, A., Huang, M., Kabir, D., Khag, V., Khaliq, S., Khatri, K., Kneth, J., Kothari, M., Najmudin, I., Panchalingam, L., Patel, M., Premachandran, L., Qayyum, A., Rana, P., Shaikh, Z., Syed, S., Theti, H., Zaidani, M., Saraf, M., de Mijolla, D., Caines, H., Kokori, A., Rocchetto, M., Mallonn, M., Bachschmidt, M., Bosch, J. M., Bretton, M., Chatelain, P., Deldem, M., Di Sisto, R., Evans, P., Fernández-Lajús, E., Guerra, P., Horta, F. G., Kang, W., Kim, T., Leroy, A., Lomoz, F., de Haro, J. L., Hentunen, V.-P., Jongen, Y., Molina, D., Montaigut, R., Naves, R., Raetz, M., Sauer, T., Watkins, A., Wünsche, A., Zibar, M., Dunn, W., Tessenyi, M., Savini, G., Tinetti, G., & Tennyson, J. 2020b, MNRAS

Edwards, B., Mugnai, L., Tinetti, G., Pascale, E., & Sarkar, S. 2019, AJ, 157, 242

Ehrenreich, D., Lovis, C., Allart, R., Zapatero Osorio, M. R., Pepe, F., Cristiani, S., Rebolo, R., Santos, N. C., Borsa, F., Demangeon, O., Dumusque, X., González Hernández, J. I., Casasayas-Barris, N., Ségransan, D., Sousa, S., Abreu, M., Adibekyan, V., Affolter, M., Allende Prieto, C., Alibert, Y., Aliverti, M., Alves, D., Amate, M., Avila, G., Baldini, V., Bandy, T., Benz, W., Bianco, A., Bolmont, É., Bouchy, F., Bourrier, V., Broeg, C., Cabral, A., Calderone, G., Pallé, E., Cegla, H. M., Cirami, R., Coelho, J. M. P., Conconi, P., Coretti, I., Cumani, C., Cupani, G., Dekker, H., Delabre, B., Deiries, S., D'Odorico, V., Di Marcantonio, P., Figueira, P., Fragoso, A., Genolet, L., Genoni, M., Génova Santos, R., Hara, N., Hughes, I., Iwert, O., Kerber, F., Knudstrup, J., Landoni, M., Lavie, B., Lizon, J.-L., Lendl, M., Lo Curto, G., Maire, C., Manescau, A., Martins, C. J. A. P., Mégevand, D., Mehner, A., Micela, G., Modigliani, A., Molaro, P., Monteiro, M., Monteiro, M., Moschetti, M., Müller, E., Nunes, N., Oggioni, L., Oliveira, A., Pariani, G., Pasquini, L., Poretti, E., Rasilla, J., Redaelli, E., Riva, M., Santana Tschudi, S., Santin, P., Santos, P., Segovia Milla, A., Seidel, J. V., Sosnowska, D., Sozzetti, A., Spanò, P., Suárez Mascareño, A., Tabernero, H., Tenegi, F., Udry, S., Zanutta, A., & Zerbi, F. 2020, Nature, 580, 597

Eisner, N. L., Nicholson, B. A., Barragán, O., Aigrain, S., Lintott, C., Kaye, L., Klein, B., Miller, G., Taylor, J., Zicher, N., Buchhave, L. A., Caldwell, D. A., Horner, J., Llama, J., Mortier, A., Rajpaul, V. M., Stassun, K., Sporer, A., Tkachenko, A.,

Jenkins, J. M., Latham, D., Ricker, G., Seager, S., Winn, J., Alhassan, S., Baeten, E. M. L., Bean, S. J., Bundy, D. M., Efremov, V., Ferstenou, R., Goodwin, B. L., Hof, M., Hoffman, T., Hubert, A., Lau, L., Lee, S., Maetschke, D., Peltsch, K., Rubio-Alfaro, C., & Wilson, G. M. 2021, MNRAS, 505, 1827

Esteves, L. J., De Mooij, E. J. W., & Jayawardhana, R. 2015, ApJ, 804, 150

Evans, T. M., Sing, D. K., Goyal, J. M., Nikolov, N., Marley, M. S., Zahnle, K., Henry, G. W., Barstow, J. K., Alam, M. K., Sanz-Forcada, J., Kataria, T., Lewis, N. K., Lavvas, P., Ballester, G. E., Ben-Jaffel, L., Blumenthal, S. D., Bourrier, V., Drummond, B., García Muñoz, A., López-Morales, M., Tremblin, P., Ehrenreich, D., Wakeford, H. R., Buchhave, L. A., Lecavelier des Etangs, A., Hébrard, É., & Williamson, M. H. 2018, AJ, 156, 283

Evans, T. M., Sing, D. K., Kataria, T., Goyal, J., Nikolov, N., Wakeford, H. R., Deming, D., Marley, M. S., Amundsen, D. S., Ballester, G. E., Barstow, J. K., Ben-Jaffel, L., Bourrier, V., Buchhave, L. A., Cohen, O., Ehrenreich, D., García Muñoz, A., Henry, G. W., Knutson, H., Lavvas, P., Lecavelier Des Etangs, A., Lewis, N. K., López-Morales, M., Mandell, A. M., Sanz-Forcada, J., Tremblin, P., & Lupu, R. 2017, Natur., 548, 58

Feng, Y. K., Line, M. R., & Fortney, J. J. 2020, AJ, 160, 137

Feng, Y. K., Line, M. R., Fortney, J. J., Stevenson, K. B., Bean, J., Kreidberg, L., & Parmentier, V. 2016, ApJ, 829, 52

Feng, Y. K., Robinson, T. D., Fortney, J. J., Lupu, R. E., Marley, M. S., Lewis, N. K., Macintosh, B., & Line, M. R. 2018, AJ, 155, 200

Feroz, F. & Hobson, M. 2008, Monthly Notices of the Royal Astronomical Society, 384, 449

Feroz, F., Hobson, M., Cameron, E., & Pettitt, A. 2013, arXiv preprint arXiv:1306.2144

Fisher, C. & Heng, K. 2018, MNRAS, 481, 4698

Fletcher, L. N., Greathouse, T. K., Orton, G. S., Sinclair, J. A., Giles, R. S., Irwin, P. G. J., & Encrenaz, T. 2016, Icar., 278, 128

Ford, E. B. & Gregory, P. C. 2007, Statistical Challenges in Modern Astronomy IV ASP Conference Series, 371, 189

Ford, E. B., Rasio, F. A., & Yu, K. 2003, in Astronomical Society of the Pacific Conference Series, Vol. 294, Scientific Frontiers in Research on Extrasolar Planets, ed. D. Deming & S. Seager, 181–188

Fortney, J. J., Lodders, K., Marley, M. S., & Freedman, R. S. 2008, ApJ, 678, 1419

Fortney, J. J., Lupu, R. E., Morley, C. V., Freedman, R. S., & Hood, C. 2019, ApJ Lett., 880, L16

Galle, J. G. 1846, MNRAS, 7, 153

Gandhi, S. & Madhusudhan, N. 2018, MNRAS, 474, 271

Gao, P., Thorngren, D. P., Lee, G. K. H., Fortney, J. J., Morley, C. V., Wakeford, H. R., Powell, D. K., Stevenson, K. B., & Zhang, X. 2020, Nature Astronomy, 1

Garhart, E., Deming, D., Mandell, A., Knutson, H. A., Wallack, N., Burrows, A., Fortney, J. J., Hood, C., Seay, C., Sing, D. K., Benneke, B., Fraine, J. D., Kataria, T., Lewis, N., Madhusudhan, N., McCullough, P., Stevenson, K. B., & Wakeford, H. 2020, AJ, 159, 137

Garland, R. 2018, PhD thesis, University of Oxford

Garland, R. & Irwin, P. G. J. 2019, arXiv e-prints, arXiv:1903.03997

Giacobbe, P., Brogi, M., Gandhi, S., Cubillos, P. E., Bonomo, A. S., Sozzetti, A., Fossati, L., Guilluy, G., Carleo, I., Rainer, M., Harutyunyan, A., Borsa, F., Pino, L., Nascimbeni, V., Benatti, S., Biazzo, K., Bignamini, A., Chubb, K. L., Claudi, R., Cosentino, R., Covino, E., Damasso, M., Desidera, S., Fiorenzano, A. F. M., Ghedina, A., Lanza, A. F., Leto, G., Maggio, A., Malavolta, L., Maldonado, J., Micela, G., Molinari, E., Pagano, I., Pedani, M., Piotto, G., Poretti, E., Scandariato, G., Yurchenko, S. N., Fantinel, D., Galli, A., Lodi, M., Sanna, N., & Tozzi, A. 2021, Natur., 592, 205

Giles, R. S., Fletcher, L. N., & Irwin, P. G. J. 2015, Icar., 257, 457

Gillon, M., Triaud, A. H. M. J., Fortney, J. J., Demory, B. O., Jehin, E., Lendl, M., Magain, P., Kabath, P., Queloz, D., Alonso, R., Anderson, D. R., Collier Cameron, A., Fumel, A., Hebb, L., Hellier, C., Lanotte, A., Maxted, P. F. L., Mowlavi, N., & Smalley, B. 2012, A&A, 542, A4

Gordon, I. E., Rothman, L. S., Hill, C., Kochanov, R. V., Tan, Y., Bernath, P. F., Birk, M., Boudon, V., Campargue, A., Chance, K. V., Drouin, B. J., Flaud, J. M., Gamache, R. R., Hodges, J. T., Jacquemart, D., Perevalov, V. I., Perrin, A., Shine, K. P., Smith, M. A. H., Tennyson, J., Toon, G. C., Tran, H., Tyuterev, V. G., Barbe, A., Császár, A. G., Devi, V. M., Furtenbacher, T., Harrison, J. J., Hartmann, J. M., Jolly, A., Johnson, T. J., Karman, T., Kleiner, I., Kyuberis, A. A., Loos, J., Lyulin, O. M., Massie, S. T., Mikhailenko, S. N., Moazzen-Ahmadi, N., Müller, H. S. P., Naumenko, O. V., Nikitin, A. V., Polyansky, O. L., Rey, M., Rotger, M., Sharpe, S. W., Sung, K., Starikova, E., Tashkun, S. A., Auwera, J. V., Wagner, G., Wilzewski, J., Wcisło, P., Yu, S., & Zak, E. J. 2017, JQSRT, 203, 3

Greene, T. P., Line, M. R., Montero, C., Fortney, J. J., Lustig-Yaeger, J., & Luther, K. 2016, ApJ, 817, 17

Guillot, T. 2010, A&A, 520, A27

Guillot, T., Burrows, A., Hubbard, W. B., Lunine, J. I., & Saumon, D. 1996, ApJ Lett., 459, L35

Hansen, J. E. & Travis, L. D. 1974, Space science reviews, 16, 527

Hellier, C., Anderson, D. R., Collier Cameron, A., Gillon, M., Jehin, E., Lendl, M., Maxted, P. F. L., Pepe, F., Pollacco, D., Queloz, D., Ségransan, D., Smalley, B., Smith, A. M. S., Southworth, J., Triaud, A. H. M. J., Udry, S., & West, R. G. 2011, A&A, 535, L7

Helling, C., Gourbin, P., Woitke, P., & Parmentier, V. 2019, A&A, 626, A133

Helling, C., Woitke, P., & Thi, W. F. 2008, A&A, 485, 547

Herschel, W. & Watson, D. 1781, Philosophical Transactions of the Royal Society of London Series I, 71, 492

Hubeny, I., Burrows, A., & Sudarsky, D. 2003, ApJ, 594, 1011

Huffman, D. R. & Wild, R. L. 1967

Irwin, P. G. J., Parmentier, V., Taylor, J., Barstow, J., Aigrain, S., Lee, G. K. H., & Garland, R. 2020, MNRAS, 493, 106

Irwin, P. G. J., Teanby, N. A., de Kok, R., Fletcher, L. N., Howett, C. J. A., Tsang, C. C. C., Wilson, C. F., Calcutt, S. B., Nixon, C. A., & Parrish, P. D. 2008, JQSRT, 109, 1136

Irwin, P. G. J., Tice, D. S., Fletcher, L. N., Barstow, J. K., Teanby, N. A., Orton, G. S., & Davis, G. R. 2015, Icar., 250, 462

Irwin, P. G. J., Toledo, D., Garland, R., Teanby, N. A., Fletcher, L. N., Orton, G. A., & Bézard, B. 2018, Nature Astronomy, 2, 420

Iyer, A. R., Swain, M. R., Zellem, R. T., Line, M. R., Roudier, G., Rocha, G., & Livingston, J. H. 2016, ApJ, 823, 109

Jacob, W. S. 1855, MNRAS, 15, 228

John, T. L. 1988, A&A, 193, 189

Kass, R. E. & Raftery, A. E. 1995, Journal of the american statistical association, 90, 773

Kataria, T., Showman, A. P., Fortney, J. J., Stevenson, K. B., Line, M. R., Kreidberg, L., Bean, J. L., & Désert, J.-M. 2015, ApJ, 801, 86

Keating, D., Cowan, N. B., & Dang, L. 2019, Nature Astronomy, 3, 1092

Kitzmann, D. & Heng, K. 2018, MNRAS, 475, 94

Knutson, H. A., Charbonneau, D., Allen, L. E., Burrows, A., & Megeath, S. T. 2008, ApJ, 673, 526

Knutson, H. A., Charbonneau, D., Allen, L. E., Fortney, J. J., Agol, E., Cowan, N. B., Showman, A. P., Cooper, C. S., & Megeath, S. T. 2007, Natur., 447, 183

Knutson, H. A., Lewis, N., Fortney, J. J., Burrows, A., Showman, A. P., Cowan, N. B., Agol, E., Aigrain, S., Charbonneau, D., Deming, D., Désert, J.-M., Henry, G. W., Langton, J., & Laughlin, G. 2012, ApJ, 754, 22

Komacek, T. D. & Showman, A. P. 2016, ApJ, 821, 16

Komacek, T. D., Showman, A. P., & Tan, X. 2017, ApJ, 835, 198

Kreidberg, L., Bean, J. L., Désert, J.-M., Line, M. R., Fortney, J. J., Madhusudhan, N., Stevenson, K. B., Showman, A. P., Charbonneau, D., McCullough, P. R., Seager, S., Burrows, A., Henry, G. W., Williamson, M., Kataria, T., & Homeier, D. 2014, ApJ Lett., 793, L27

Kreidberg, L., Line, M. R., Parmentier, V., Stevenson, K. B., Louden, T., Bonnefoy, M., Faherty, J. K., Henry, G. W., Williamson, M. H., Stassun, K., Beatty, T. G., Bean, J. L., Fortney, J. J., Showman, A. P., Désert, J.-M., & Arcangeli, J. 2018, AJ, 156, 17

Krissansen-Totton, J., Garland, R., Irwin, P., & Catling, D. C. 2018, AJ, 156, 114

Lacis, A. A. & Oinas, V. 1991, JGR, 96, 9027

Lavie, B., Mendonça, J. M., Mordasini, C., Malik, M., Bonnefoy, M., Demory, B.-O., Oreshenko, M., Grimm, S. L., Ehrenreich, D., & Heng, K. 2017, AJ, 154, 91

Lee, G. K. H., Taylor, J., Grimm, S. L., Baudino, J.-L., Garland, R., Irwin, P. G. J., & Wood, K. 2019, MNRAS, 487, 2082

Lee, J. M., Fletcher, L. N., & Irwin, P. G. J. 2012, MNRAS, 420, 170

Lee, J.-M., Heng, K., & Irwin, P. G. J. 2013, ApJ, 778, 97

Lee, J.-M., Irwin, P. G. J., Fletcher, L. N., Heng, K., & Barstow, J. K. 2014, ApJ, 789, 14

Lenzuni, P., Chernoff, D. F., & Salpeter, E. E. 1991, ApJ Supp., 76, 759

Lewis, N. K., Wakeford, H. R., MacDonald, R. J., Goyal, J. M., Sing, D. K., Barstow, J., Powell, D., Kataria, T., Mishra, I., Marley, M. S., Batalha, N. E., Moses, J. I., Gao, P., Wilson, T. J., Chubb, K. L., Mikal-Evans, T., Nikolov, N., Pirzkal, N., Spake, J. J., Stevenson, K. B., Valenti, J., & Zhang, X. 2020, ApJ Lett., 902, L19

Li, G., Gordon, I. E., Rothman, L. S., Tan, Y., Hu, S.-M., Kassi, S., Campargue, A., & Medvedev, E. S. 2015, The Astrophysical Journal Supplement Series, 216, 15

Line, M. R., Knutson, H., Wolf, A. S., & Yung, Y. L. 2014, ApJ, 783, 70

Line, M. R. & Parmentier, V. 2016, ApJ, 820, 78

Line, M. R., Stevenson, K. B., Bean, J., Desert, J.-M., Fortney, J. J., Kreidberg, L., Madhusudhan, N., Showman, A. P., & Diamond-Lowe, H. 2016, AJ, 152, 203

Line, M. R., Wolf, A. S., Zhang, X., Knutson, H., Kammer, J. A., Ellison, E., Deroo, P., Crisp, D., & Yung, Y. L. 2013, ApJ, 775, 137

Line, M. R., Zhang, X., Vasisht, G., Natraj, V., Chen, P., & Yung, Y. L. 2012, ApJ, 749, 93

MacDonald, R. J. & Madhusudhan, N. 2017, MNRAS, 469, 1979

Mai, C. & Line, M. R. 2019, ApJ, 883, 144

Majeau, C., Agol, E., & Cowan, N. B. 2012, ApJ Lett., 747, L20

Mansfield, M., Schlawin, E., Lustig-Yaeger, J., Adams, A. D., Rauscher, E., Arcangeli, J., Feng, Y. K., Gupta, P., Keating, D., Stevenson, K. B., & Beatty, T. G. 2020, MNRAS, 499, 5151

Marley, M. S., Seager, S., Saumon, D., Lodders, K., Ackerman, A. S., Freedman, R. S., & Fan, X. 2002, ApJ, 568, 335

May, E. M. & Stevenson, K. B. 2020, AJ, 160, 140

May, E. M., Taylor, J., Komacek, T. D., Line, M. R., & Parmentier, V. 2021, arXiv e-prints, arXiv:2103.09313

Mayor, M. & Queloz, D. 1995, Natur., 378, 355

McCormac, J., Gillen, E., Jackman, J. A. G., Brown, D. J. A., Bayliss, D., Wheatley, P. J., Anderson, D. R., Armstrong, D. J., Bouchy, F., Briegal, J. T., Burleigh, M. R., Cabrera, J., Casewell, S. L., Chaushev, A., Chazelas, B., Chote, P., Cooke, B. F., Costes, J. C., Csizmadia, S., Eigmüller, P., Erikson, A., Foxell, E., Gänsicke, B. T., Goad, M. R., Günther, M. N., Hodgkin, S. T., Hooton, M. J., Jenkins, J. S., Lambert, G., Lendl, M., Longstaff, E., Louden, T., Moyano, M., Nielsen, L. D., Pollacco, D., Queloz, D., Rauer, H., Raynard, L., Smith, A. M. S., Smalley, B., Soto, M., Turner, O., Udry, S., Vines, J. I., Walker, S. R., Watson, C. A., & West, R. G. 2020, MNRAS, 493, 126

Mendonça, J. M., Grimm, S. L., Grosheintz, L., & Heng, K. 2016, ApJ, 829, 115

Mendonça, J. M., Tsai, S.-m., Malik, M., Grimm, S. L., & Heng, K. 2018, ApJ, 869, 107

Min, M. 2017, A&A, 607, A9

Mollière, P., Stolker, T., Lacour, S., Otten, G. P. P. L., Shangguan, J., Charnay, B., Molyarova, T., Nowak, M., Henning, T., Marleau, G. D., Semenov, D. A., van Dishoeck, E., Eisenhauer, F., Garcia, P., Garcia Lopez, R., Girard, J. H., Greenbaum, A. Z., Hinkley, S., Kervella, P., Kreidberg, L., Maire, A. L., Nasedkin, E., Pueyo, L., Snellen, I. A. G., Vigan, A., Wang, J., de Zeeuw, P. T., & Zurlo, A. 2020, arXiv e-prints, arXiv:2006.09394

Mollière, P., van Boekel, R., Dullemond, C., Henning, T., & Mordasini, C. 2015, ApJ, 813, 47

Morello, G., Danielski, C., Dickens, D., Tremblin, P., & Lagage, P. O. 2019, AJ, 157, 205

Morley, C. V., Fortney, J. J., Marley, M. S., Visscher, C., Saumon, D., & Leggett, S. K. 2012, ApJ, 756, 172

Moses, J. I., Visscher, C., Fortney, J. J., Showman, A. P., Lewis, N. K., Griffith, C. A., Klippenstein, S. J., Shabram, M., Friedson, A. J., Marley, M. S., & Freedman, R. S. 2011, ApJ, 737, 15

Moulton, F. R. 1899, AJ, 20, 33

Ohno, K. & Okuzumi, S. 2018, ApJ, 859, 34

Palik, E. D. 1998, Handbook of optical constants of solids [electronic resource], Ebook central (San Diego: Academic Press)

Parmentier, V., Fortney, J. J., Showman, A. P., Morley, C., & Marley, M. S. 2016, ApJ, 828, 22

Parmentier, V. & Guillot, T. 2014, A&A, 562, A133

Parmentier, V., Line, M. R., Bean, J. L., Mansfield, M., Kreidberg, L., Lupu, R., Visscher, C., Désert, J.-M., Fortney, J. J., Deleuil, M., Arcangeli, J., Showman, A. P., & Marley, M. S. 2018, A&A, 617, A110

Parmentier, V., Showman, A. P., & Fortney, J. J. 2021, MNRAS, 501, 78

Piette, A. A. A. & Madhusudhan, N. 2020, ApJ, 904, 154

Pinhas, A. & Madhusudhan, N. 2017, Monthly Notices of the Royal Astronomical Society, 471, 4355

Pinhas, A., Madhusudhan, N., Gandhi, S., & MacDonald, R. 2019, MNRAS, 482, 1485

Pluriel, W., Whiteford, N., Edwards, B., Changeat, Q., Yip, K. H., Baeyens, R., Al-Refaie, A., Fabienne Bieger, M., Blain, D., Gressier, A., Guilluy, G., Yassin Jaziri, A., Kiefer, F., Modirrousta-Galian, D., Morvan, M., Mugnai, L. V., Poveda, M., Skaf, N., Zingales, T., Wright, S., Charnay, B., Drossart, P., Leconte, J., Tsiaras, A., Venot, O., Waldmann, I., & Beaulieu, J.-P. 2020a, AJ, 160, 112

Pluriel, W., Zingales, T., Leconte, J., & Parmentier, V. 2020b, A&A, 636, A66

Polyansky, O. L., Kyuberis, A. A., Zobov, N. F., Tennyson, J., Yurchenko, S. N., & Lodi, L. 2018, Monthly Notices of the RAS, 480, 2597

Powell, D., Zhang, X., Gao, P., & Parmentier, V. 2018, ApJ, 860, 18

Rathcke, A. D., MacDonald, R. J., Barstow, J. K., Goyal, J. M., Lopez-Morales, M., Mendonça, J. M., Sanz-Forcada, J., Henry, G. W., Sing, D. K., Alam, M. K., Lewis, N. K., Chubb, K. L., Taylor, J., Nikolov, N., & Buchhave, L. A. 2021, arXiv e-prints, arXiv:2104.10688

Rauscher, E., Menou, K., Seager, S., Deming, D., Cho, J. Y. K., & Hansen, B. M. S. 2007, ApJ, 664, 1199

Rauscher, E., Suri, V., & Cowan, N. B. 2018, AJ, 156, 235

Rutten, R. J. 2003, Radiative Transfer in Stellar Atmospheres

Samra, D., Helling, C., & Min, M. 2020, A&A, 639, A107

Santerne, A., Malavolta, L., Kosiarek, M. R., Dai, F., Dressing, C. D., Dumusque, X., Hara, N. C., Lopez, T. A., Mortier, A., Vanderburg, A., Adibekyan, V., Armstrong, D. J., Barrado, D., Barros, S. C. C., Bayliss, D., Berardo, D., Boisse, I., Bonomo, A. S., Bouchy, F., Brown, D. J. A., Buchhave, L. A., Butler, R. P., Collier Cameron, A., Cosentino, R., Crane, J. D., Crossfield, I. J. M., Damasso, M., Deleuil, M. R., Delgado Mena, E., Demangeon, O., Díaz, R. F., Donati, J. F., Figueira, P., Fulton, B. J., Ghedina, A., Harutyunyan, A., Hébrard, G., Hirsch, L. A., Hojjatpanah, S., Howard, A. W., Isaacson, H., Latham, D. W., Lillo-Box, J., López-Morales, M., Lovis, C., Martinez Fiorenzano, A. F., Molinari, E., Mousis, O., Moutou, C., Nava, C., Nielsen, L. D., Osborn, H. P., Petigura, E. A., Phillips, D. F., Pollacco, D. L., Poretti, E., Rice, K., Santos, N. C., Ségransan, D., Shectman, S. A., Sinukoff,

E., Sousa, S. G., Sozzetti, A., Teske, J. K., Udry, S., Vigan, A., Wang, S. X., Watson, C. A., Weiss, L. M., Wheatley, P. J., & Winn, J. N. 2019, arXiv e-prints, arXiv:1911.07355

Schulze-Hartung, T., Launhardt, R., & Henning, T. 2012, Astronomy & Astrophysics, 545, A79

Schwartz, J. C. & Cowan, N. B. 2015, MNRAS, 449, 4192

Schwarz, H., Brogi, M., de Kok, R., Birkby, J., & Snellen, I. 2015, A&A, 576, A111

Sharp, C. M. & Burrows, A. 2007, ApJ Supp., 168, 140

Showman, A. P., Fortney, J. J., Lian, Y., Marley, M. S., Freedman, R. S., Knutson, H. A., & Charbonneau, D. 2009, ApJ, 699, 564

Showman, A. P. & Guillot, T. 2002, A&A, 385, 166

Sing, D. K., Fortney, J. J., Nikolov, N., Wakeford, H. R., Kataria, T., Evans, T. M., Aigrain, S., Ballester, G. E., Burrows, A. S., Deming, D., Désert, J.-M., Gibson, N. P., Henry, G. W., Huitson, C. M., Knutson, H. A., Lecavelier Des Etangs, A., Pont, F., Showman, A. P., Vidal-Madjar, A., Williamson, M. H., & Wilson, P. A. 2016, Natur., 529, 59

Stevenson, K. B., Désert, J.-M., Line, M. R., Bean, J. L., Fortney, J. J., Showman, A. P., Kataria, T., Kreidberg, L., McCullough, P. R., Henry, G. W., Charbonneau, D., Burrows, A., Seager, S., Madhusudhan, N., Williamson, M. H., & Homeier, D. 2014, Science, 346, 838

Stevenson, K. B., Lewis, N. K., Bean, J. L., Beichman, C., Fraine, J., Kilpatrick, B. M., Krick, J. E., Lothringer, J. D., Mandell, A. M., Valenti, J. A., Agol, E., Angerhausen, D., Barstow, J. K., Birkmann, S. M., Burrows, A., Charbonneau, D., Cowan, N. B., Crouzet, N., Cubillos, P. E., Curry, S. M., Dalba, P. A., de Wit, J., Deming, D., Désert, J.-M., Doyon, R., Dragomir, D., Ehrenreich, D., Fortney, J. J., García Muñoz, A., Gibson, N. P., Gizis, J. E., Greene, T. P., Harrington, J., Heng, K., Kataria, T., Kempton, E. M. R., Knutson, H., Kreidberg, L., Lafrenière, D., Lagage, P.-O., Line, M. R., Lopez-Morales, M., Madhusudhan, N., Morley, C. V., Rocchetto, M., Schlawin, E., Shkolnik, E. L., Shporer, A., Sing, D. K., Todorov, K. O., Tucker, G. S., & Wakeford, H. R. 2016, PASP, 128, 094401

Stevenson, K. B., Line, M. R., Bean, J. L., Désert, J.-M., Fortney, J. J., Showman, A. P., Kataria, T., Kreidberg, L., & Feng, Y. K. 2017, AJ, 153, 68

Struve, O. 1952, The Observatory, 72, 199

Taylor, J., Parmentier, V., Irwin, P. G. J., Aigrain, S., Lee, G. K. H., & Krissansen-Totton, J. 2020, MNRAS, 493, 4342

Taylor, J., Parmentier, V., Line, M. R., Lee, E. K. H., Irwin, P. G. J., & Aigrain, S. 2021, MNRAS

Teanby, N. A., Cordiner, M. A., Nixon, C. A., Irwin, P. G. J., Hörst, S. M., Sylvestre, M., Serigano, J., Thelen, A. E., Richards, A. M. S., & Charnley, S. B. 2018, AJ, 155, 251

Tennyson, J. & Yurchenko, S. N. 2017, International Journal of Quantum Chemistry, 117, 92

Thorngren, D., Gao, P., & Fortney, J. J. 2019, ApJ Lett., 884, L6

Tinetti, G., Drossart, P., Eccleston, P., Hartogh, P., Heske, A., Leconte, J., Micela, G., Ollivier, M., Pilbratt, G., Puig, L., Turrini, D., Vandenbussche, B., Wolkenberg, P., Beaulieu, J.-P., Buchave, L. A., Ferus, M., Griffin, M., Guedel, M., Justtanont, K., Lagage, P.-O., Machado, P., Malaguti, G., Min, M., Nørgaard-Nielsen, H. U., Rataj, M., Ray, T., Ribas, I., Swain, M., Szabo, R., Werner, S., Barstow, J., Burleigh, M., Cho, J., du Foresto, V. C., Coustenis, A., Decin, L., Encrenaz, T., Galand, M., Gillon, M., Helled, R., Morales, J. C., Muñoz, A. G., Moneti, A., Pagano, I., Pascale, E., Piccioni, G., Pinfield, D., Sarkar, S., Selsis, F., Tennyson, J., Triaud, A., Venot, O., Waldmann, I., Waltham, D., Wright, G., Amiaux, J., Auguères, J.-L., Berthé, M., Bezawada, N., Bishop, G., Bowles, N., Coffey, D., Colomé, J., Crook, M., Crouzet, P.-E., Da Peppo, V., Sanz, I. E., Focardi, M., Frericks, M., Hunt, T., Kohley, R., Middleton, K., Morgante, G., Ottensamer, R., Pace, E., Pearson, C., Stamper, R., Symonds, K., Rengel, M., Renotte, E., Ade, P., Affer, L., Alard, C., Allard, N., Altieri, F., André, Y., Arena, C., Argyriou, I., Aylward, A., Baccani, C., Bakos, G., Banaszkiewicz, M., Barlow, M., Batista, V., Bellucci, G., Benatti, S., Bernardi, P., Bézard, B., Blecka, M., Bolmont, E., Bonfond, B., Bonito, R., Bonomo, A. S., Brucato, J. R., Brun, A. S., Bryson, I., Bujwan, W., Casewell, S., Charnay, B., Pestellini, C. C., Chen, G., Ciaravella, A., Claudi, R., Clédassou, R., Damasso, M., Damiano, M., Danielski, C., Deroo, P.,

Di Giorgio, A. M., Dominik, C., Doublier, V., Doyle, S., Doyon, R., Drummond, B., Duong, B., Eales, S., Edwards, B., Farina, M., Flaccomio, E., Fletcher, L., Forget, F., Fossey, S., Fränz, M., Fujii, Y., García-Piquer, Á., Gear, W., Geoffray, H., Gérard, J. C., Gesa, L., Gomez, H., Graczyk, R., Griffith, C., Grodent, D., Guarcello, M. G., Gustin, J., Hamano, K., Hargrave, P., Hello, Y., Heng, K., Herrero, E., Hornstrup, A., Hubert, B., Ida, S., Ikoma, M., Iro, N., Irwin, P., Jarchow, C., Jaubert, J., Jones, H., Julien, Q., Kameda, S., Kerschbaum, F., Kervella, P., Koskinen, T., Krijger, M., Krupp, N., Lafarga, M., Landini, F., Lellouch, E., Leto, G., Luntzer, A., Rank-Lüftinger, T., Maggio, A., Maldonado, J., Maillard, J.-P., Mall, U., Marquette, J.-B., Mathis, S., Maxted, P., Matsuo, T., Medvedev, A., Miguel, Y., Minier, V., Morello, G., Mura, A., Narita, N., Nascimbeni, V., Nguyen Tong, N., Noce, V., Oliva, F., Palle, E., Palmer, P., Pancrazzi, M., Papageorgiou, A., Parmentier, V., Perger, M., Petralia, A., Pezzuto, S., Pierrehumbert, R., Pillitteri, I., Piotto, G., Pisano, G., Prisinzano, L., Radioti, A., Réess, J.-M., Rezac, L., Rocchetto, M., Rosich, A., Sanna, N., Santerne, A., Savini, G., Scandariato, G., Sicardy, B., Sierra, C., Sindoni, G., Skup, K., Snellen, I., Sobiecki, M., Soret, L., Sozzetti, A., Stiepen, A., Strugarek, A., Taylor, J., Taylor, W., Terenzi, L., Tessenyi, M., Tsiaras, A., Tucker, C., Valencia, D., Vasisht, G., Vazan, A., Vilardell, F., Vinatier, S., Viti, S., Waters, R., Wawer, P., Wawrzaszek, A., Whitworth, A., Yung, Y. L., Yurchenko, S. N., Osorio, M. R. Z., Zellem, R., Zingales, T., & Zwart, F. 2018, Experimental Astronomy, 46, 135

Tinetti, G., Eccleston, P., Haswell, C., Lagage, P.-O., Leconte, J., Lüftinger, T., Micela, G., Min, M., Pilbratt, G., Puig, L., Swain, M., Testi, L., Turrini, D., Vandenbussche, B., Rosa Zapatero Osorio, M., Aret, A., Beaulieu, J.-P., Buchhave, L., Ferus, M., Griffin, M., Guedel, M., Hartogh, P., Machado, P., Malaguti, G., Pallé, E., Rataj, M., Ray, T., Ribas, I., Szabó, R., Tan, J., Werner, S., Ratti, F., Scharmberg, C., Salvignol, J.-C., Boudin, N., Halain, J.-P., Haag, M., Crouzet, P.-E., Kohley, R., Symonds, K., Renk, F., Caldwell, A., Abreu, M., Alonso, G., Amiaux, J., Berthé, M., Bishop, G., Bowles, N., Carmona, M., Coffey, D., Colomé, J., Crook, M., Désjonqueres, L., Díaz, J. J., Drummond, R., Focardi, M., Gómez, J. M., Holmes, W., Krijger, M., Kovacs, Z., Hunt, T., Machado, R., Morgante, G., Ollivier, M., Ottensamer, R., Pace, E., Pagano, T., Pascale, E., Pearson, C., Møller Pedersen, S., Pniel, M., Roose, S., Savini, G., Stamper, R., Szirovicza, P., Szoke, J., Tosh, I., Vilardell, F., Barstow, J., Borsato, L., Casewell, S., Changeat, Q., Charnay, B., Civiš, S., Coudé du Foresto, V., Coustenis, A., Cowan, N., Danielski,

C., Demangeon, O., Drossart, P., Edwards, B. N., Gilli, G., Encrenaz, T., Kiss, C., Kokori, A., Ikoma, M., Morales, J. C., Mendonça, J., Moneti, A., Mugnai, L., García Muñoz, A., Helled, R., Kama, M., Miguel, Y., Nikolaou, N., Pagano, I., Panic, O., Rengel, M., Rickman, H., Rocchetto, M., Sarkar, S., Selsis, F., Tennyson, J., Tsiaras, A., Venot, O., Vida, K., Waldmann, I. P., Yurchenko, S., Szabó, G., Zellem, R., Al-Refaie, A., Perez Alvarez, J., Anisman, L., Arhancet, A., Ateca, J., Baeyens, R., Barnes, J. R., Bell, T., Benatti, S., Biazzo, K., Blkecka, M., Bonomo, A. S., Bosch, J., Bossini, D., Bourgalais, J., Brienza, D., Brucalassi, A., Bruno, G., Caines, H., Calcutt, S., Campante, T., Canestrari, R., Cann, N., Casali, G., Casas, A., Cassone, G., Cara, C., Carmona, M., Carone, L., Carrasco, N., Changeat, Q., Chioetto, P., Cortecchia, F., Czupalla, M., Chubb, K. L., Ciaravella, A., Claret, A., Claudi, R., Codella, C., Garcia Comas, M., Cracchiolo, G., Cubillos, P., Da Peppo, V., Decin, L., Dejabrun, C., Delgado-Mena, E., Di Giorgio, A., Diolaiti, E., Dorn, C., Doublier, V., Doumayrou, E., Dransfield, G., Dumaye, L., Dunford, E., Jimenez Escobar, A., Van Eylen, V., Farina, M., Fedele, D., Fernández, A., Fleury, B., Fonte, S., Fontignie, J., Fossati, L., Funke, B., Galy, C., Garai, Z., García, A., García-Rigo, A., Garufi, A., Germano Sacco, G., Giacobbe, P., Gómez, A., Gonzalez, A., Gonzalez-Galindo, F., Grassi, D., Griffith, C., Guarcello, M. G., Goujon, A., Gressier, A., Grzegorczyk, A., Guillot, T., Guilluy, G., Hargrave, P., Hellin, M.-L., Herrero, E., Hills, M., Horeau, B., Ito, Y., Jessen, N. C., Kabath, P., Kálmán, S., Kawashima, Y., Kimura, T., Knížek, A., Kreidberg, L., Kruid, R., Kruijssen, D. J. M., Kubelík, P., Lara, L., Lebonnois, S., Lee, D., Lefevre, M., Lichtenberg, T., Locci, D., Lombini, M., Sanchez Lopez, A., Lorenzani, A., MacDonald, R., Magrini, L., Maldonado, J., Marcq, E., Migliorini, A., Modirrousta-Galian, D., Molaverdikhani, K., Molinari, S., Mollière, P., Moreau, V., Morello, G., Morinaud, G., Morvan, M., Moses, J. I., Mouzali, S., Nakhjiri, N., Naponiello, L., Narita, N., Nascimbeni, V., Nikolaou, A., Noce, V., Oliva, F., Palladino, P., Papageorgiou, A., Parmentier, V., Peres, G., Pérez, J., Perez-Hoyos, S., Perger, M., Cecchi Pestellini, C., Petralia, A., Philippon, A., Piccialli, A., Pignatari, M., Piotto, G., Podio, L., Polenta, G., Preti, G., Pribulla, T., Lopez Puertas, M., Rainer, M., Reess, J.-M., Rimmer, P., Robert, S., Rosich, A., Rossi, L., Rust, D., Saleh, A., Sanna, N., Schisano, E., Schreiber, L., Schwartz, V., Scippa, A., Seli, B., Shibata, S., Simpson, C., Shorttle, O., Skaf, N., Skup, K., Sobiecki, M., Sousa, S., Sozzetti, A., Šponer, J., Steiger, L., Tanga, P., Tackley, P., Taylor, J., Tecza, M., Terenzi, L., Tremblin, P., Tozzi, A., Triaud, A., Trompet, L., Tsai, S.-M., Tsantaki, M., Valencia, D., Carine Vandaele, A., Van der Swaelmen, M., Vardan, A., Vasisht, G.,

Vazan, A., Del Vecchio, C., Waltham, D., Wawer, P., Widemann, T., Wolkenberg, P., Hou Yip, G., Yung, Y., Zilinskas, M., Zingales, T., & Zuppella, P. 2021, arXiv e-prints, arXiv:2104.04824

Toledo, D., Irwin, P. G. J., Rannou, P., Teanby, N. A., Simon, A. A., Wong, M. H., & Orton, G. S. 2019, Icar., 333, 1

Toon, O. B., McKay, C. P., Ackerman, T. P., & Santhanam, K. 1989, JGR, 94, 16287

Tremblay, L., Line, M. R., Stevenson, K., Kataria, T., Zellem, R. T., Fortney, J. J., & Morley, C. 2020, AJ, 159, 117

Trotta, R. 2008, Contemporary Physics, 49, 71

Tsiaras, A., Waldmann, I. P., Zingales, T., Rocchetto, M., Morello, G., Damiano, M., Karpouzas, K., Tinetti, G., McKemmish, L. K., Tennyson, J., & Yurchenko, S. N. 2018, AJ, 155, 156

Venot, O., Parmentier, V., Blecic, J., Cubillos, P. E., Waldmann, I. P., Changeat, Q., Moses, J. I., Tremblin, P., Crouzet, N., Gao, P., Powell, D., Lagage, P.-O., Dobbs-Dixon, I., Steinrueck, M. E., Kreidberg, L., Batalha, N., Bean, J. L., Stevenson, K. B., Casewell, S., & Carone, L. 2020, ApJ, 890, 176

von Essen, C., Mallonn, M., Borre, C. C., Antoci, V., Stassun, K. G., Khalafinejad, S., & Tautvaišienė, G. 2020, A&A, 639, A34

Wakeford, H. R. & Sing, D. K. 2015, A&A, 573, A122

Wakeford, H. R., Sing, D. K., Deming, D., Lewis, N. K., Goyal, J., Wilson, T. J., Barstow, J., Kataria, T., Drummond, B., Evans, T. M., Carter, A. L., Nikolov, N., Knutson, H. A., Ballester, G. E., & Mandell, A. M. 2018, AJ, 155, 29

Wakeford, H. R., Sing, D. K., Evans, T., Deming, D., & Mandell, A. 2016, ApJ, 819, 10

Wakeford, H. R., Sing, D. K., Stevenson, K. B., Lewis, N. K., Pirzkal, N., Wilson, T. J., Goyal, J., Kataria, T., Mikal-Evans, T., Nikolov, N., & Spake, J. 2020, AJ, 159, 204

Wakeford, H. R., Visscher, C., Lewis, N. K., Kataria, T., Marley, M. S., Fortney, J. J., & Mandell, A. M. 2017, MNRAS, 464, 4247

Wakeford, H. R., Wilson, T. J., Stevenson, K. B., & Lewis, N. K. 2019, Research Notes of the American Astronomical Society, 3, 7

Welbanks, L. & Madhusudhan, N. 2019, AJ, 157, 206

Wilkins, A. N., Delrez, L., Barker, A. J., Deming, D., Hamilton, D., Gillon, M., & Jehin, E. 2017, ApJ Lett., 836, L24

Wittenmyer, R. A., Endl, M., Cochran, W. D., Hatzes, A. P., Walker, G. A. H., Yang, S. L. S., & Paulson, D. B. 2006, AJ, 132, 177

Woitke, P. & Helling, C. 2003, A&A, 399, 297

Woitke, P., Helling, C., Hunter, G. H., Millard, J. D., Turner, G. E., Worters, M., Blecic, J., & Stock, J. W. 2018, A&A, 614, A1

Yurchenko, S. N., Al-Refaie, A. F., & Tennyson, J. 2018, A&A, 614, A131

Zellem, R. T., Lewis, N. K., Knutson, H. A., Griffith, C. A., Showman, A. P., Fortney, J. J., Cowan, N. B., Agol, E., Burrows, A., Charbonneau, D., Deming, D., Laughlin, G., & Langton, J. 2014, ApJ, 790, 53